Direct Numerical Calculation on the Collective Motion of Model Microswimmers

Norihiro Oyama

2017

Acknowledgements

I would like to show my greatest gratitude to my supervisor, Professor Dr. Ryoichi Yamamoto, for his coaching and various support throughout whole my days in this lab. And I thank Professor Dr. Minoru Miyahara and Professor Dr. Takaji Inamuro for their insightful review and comments on this dissertation. I acknowledge also Associate Professor Dr. Takashi Taniguchi for enlightening advice. I would like to thank Assistant Professor Dr. John Jairo Molina. I learned really a lot from him. Thank you also to Dr. Hideyuki Mizuno, Dr. Rei Tatsumi, Dr. Simon K. Schnyder, Dr. Gregory Lecrivain, Dr. Mitsusuke Tarama, Dr. Hiroaki Ito for their helpful discussions, guidance, suggestion and showing how exciting the academic life is. A very special thanks to all the members of the transport phenomena lab. for providing a wonderful and exciting environment.

Above all, I would like to thank particularly my family, Kazuo, Satsuki, Kiyohito and Levin, for their support, encouragement, love and unwavering belief in me. Without you, I would not be the person I am today. My special gratitude goes to Mr. Hiroto Yada and Mr. Suguru Aoki for encouragement, support and all precious time spent together.

List of Publications

Chapter 2

Norihiro Oyama, John Jairo Molina and Ryoichi Ymamoto,"Hydrodynamically assisted binary collisions of microswimmers", *to be submitted*

Chapter 3

Norihiro Oyama, John Jairo Molina and Ryoichi Ymamoto, "Purely hydrodynamic origin for swarming of swimming particles", *Phys. Rev. E*, **93**, 043114 (2016)

This chapter is reprinted from this paper with revisions and with the permission. All figures in this paper is reused in the dissertation with the permission. Copyright (2016) by the American Physical Society.

Chapter 4

Norihiro Oyama, John Jairo Molina and Ryoichi Ymamoto, "Hydrodynamic alignment of microswimmers in pipes", *Eur. Phys. J. E, submitted*

Contents

1 General Introduction

1.1 Introductory Remarks

Active matter systems are now attracting more and more interests of many researchers from the various area as representative systems of the out-of-equilibrium state[1–19]. The terminology “active matter” is a general name of the systems in which internal energy is converted into mechanical work. All the living creatures including human beings can be pronounced as examples of active matters[20–24] , and recently even nonliving examples have been being developed. As the examples for nonliving active systems, oil drops in water[25, 26], camphor rafts floating on water surface[27], active Janus particles on whose only “active” part of the surface chemical reactions take place[28–30] and the Belousov-Zhabotinsky reaction[31, 32] can be numerated. It is well-known that active matter systems can show nontrivial collective motion which cannot be predicted only by looking at the dynamics of single agent. Such collective motion can be observed over vast range of length scales. As a microscopic system, for example, the protein filaments can show collective alignment[33, 34] of their moving direction, and as a macroscopic system, fish or birds are known to swim in big schools or flocks[22, 23]. Among them, the author is interested in microswimmers, which propel themselves as the consequent of the interactions with the ambient fluid, such as microorganisms or Janus particles. Such systems are much simpler than macroscopic systems and can show nontrivial collective motions only due to physical contributions such as the hydrodynamic interactions and the finite volume effects, as presented in this dissertation. This is because in microswimmer dispersions the Reynolds number is very low and the viscous effect is dominant. At the same time, microswimmers are

expected to be applied to various engineering situations like the targeted drug delivery systems or a brand new material with tunable viscosity. In this dissertation, the author investigate the collective dynamics of the microswimmer dispersions in various circumstances such as in bulk or under confinement, by means of direct numerical simulation with full hydrodynamics.

1.2 Brief Review on the Field of Microswimmers

Before going into the specific topics about this dissertation, the scientific researches on dynamics of microswimmers so far are reviewed briefly in this section. The approaches of studies on microswimmers can be roughly divided into two tactics, namely, the single-body study and the many-body study. These difference in the tactics comes from the different focuses of the study. The single-body study focus on the detailed precise motion of a single swimmer itself. Experimentally, direct measurement of the flagellar motion of Chlamydomonas have been reported[35]. Numerically or theoretically, distinct specific models are composed one by one depending on details of the targeted systems. The elucidation of the swimming mechanism of a bacteria[36] or the optimazation problems for the sperm shape or the flagellum motion have been reported, for example[37]. Such study sometimes go into certain biological problems, for example why the current shape is selected in the course of the evolution. Because collective behaviors of many-body systems are the focus of this dissertation, only studies on many-body systems are introduced in detail in the following.

Regarding the many-body systems, it is known that the emergence of nontrivial collective behaviors can be expected as presented above, and such collective motions are usually main focus of the many-body studies. The discovery of a brand new collective motion, the quantitative evaluation or the specifying the onset of such collective motions are the major approaches. Experimentally, many works are on the dynamics

of microswimmers with certain objects or confinements[38–42]. For numerical or theoretical works, rough and simplified models are selected as the mathematical treatment for each single agent, or sometimes even the continuum description is employed.

First of all, the Vicsek model[43] can be announced as the simplest and very successful agent-based numerical model for the active systems. The model is a phenomenological one which is characterized by only two factors: the intensity of the alignment effects and the noise. Both these two effects are free from any physical origins and just introduced to mimic what we observe in the nature phenomenologically. In this model, the agents are modeled by the point particles which have only the information of the position and orientation. They move at the constant speed and change orientation as the consequent of the phenomenological interactions of the neighboring particles. A particle changes its direction so that the resultant value coincides the average of the directions of the neighbors. Such a scheme for directional change leads to the local alignment. The neighbors are defined with respect to the distance from the reference particle, and the directional change can also include noise term. Despite its simplicity, the Vicsek model is very powerful to reproduce many qualitatively different phenomena[44–46], including very long-ranged global ordering. Physicists and even biologists are now thinking that the model is so potent that we still can obtain more different motions only adding a little bit more components.

Several simplified agent-based models of rigid spheres are introduced, which can take into account the finite volume effects. Active Brownian particles (ABPs)[47–49] and Run-and-tumble Model (RTM)[50–53] are course grained models where the hydrodynamic interactions are not treated explicitly. In those models, particles have their own persistent moving directions, and change randomly depending on the model details: ABP change the direction according to the rotational diffusion, and RTM change the direction at a specific tumbling rate. The merit of these models are the simpleness such that the theoretical treatment is relatively easy.

As to examples of such theoretical treatments of microswimmer system, recently

many efforts have been dedicated to the trial to compose the united theory like thermodynamics for the passive, equilibrium systems [11, 12, 14–16, 19, 54–58]. Especially, recently the concept of the active pressure is introduced for the system of the ABPs. It is reported that the motility induced phase separation, which is typical collective behaviors of the active systems, can be quantitatively understandable in analogy of the liquid-gas phase separation in the passive equilibrium systems [12, 16, 19, 54, 57]. However, still such theoretical description is limited to the systems where the hydrodynamic interactions can be ignored. Recently it is proved that the active pressure cannot be the state variable generally, especially when the interactions have the orientation-dependency[12], and the field is now facing a very big challenge.

So far, in these theoretical works with "thermodynamic" approach, hydrodynamic interaction are ignored, though it is known to be important for the dynamics of microswimmer systems. Regarding the theoretical works with hydrodynamic interactions, several works on the dynamics of the many-body systems can be found. These are continuum model which gives the Smoluchowski-type time evolution of probability distribution function[59–61]. In these models, the active stress term is introduced as the dipole form. They succeeded in predicting the existence of density waves by conducting the linear stability analysis. However, these model description is composed under the far-field approximation, and the results are conflicting against those from squirmer dispersions, which are introduced in the following paragraph, even at the semi-dilute condition, as presented in the **Chapter 3**.

The squirmer model is a commonly used model whose motion is induced by the purely hydrodynamic interactions between the host fluid[62, 63]. In this model, the microswimmers are expressed as spherical rigid particles as presented later. The activeness is introduced by giving the prescribed flow field as the modified stick boundary condition on the surface. Squirmers propel themselves by utilizing the reaction of such an active flow field. Due to this model characteristics, studies using the squirmer model require the complicated numerical calculation of a particle-fluid multi-phase

flow. Although already many efforts are dedicated to the dynamics of squirmer dispersions [64–78], there are still many open questions. In this dissertation, the author tackle some of those questions.

1.3 Swimming types

Microswimmers can be divided roughly into three different types. It is known that the property of collective motion of microswimmers depends strongly on such swimming types. In this section, the distinguish between them is introduced.

The types can be divided, first, by the appendages utilized to generate propulsion. Some utilize cilia, tiny hair, and the others do flagella, relatively longer hair, to propel themselves. For the former type of swimmers, sometimes mentioned as *neutral swimmers*, in most cases, cilia are spreading throughout the whole surface of a swimmer body. They move cilia in a well-synchronized manner and push the surrounding fluid by propagation of metachronal wave of ciliary envelope. As the reaction to the ambient flow field, they propel themselves. The latter types of swimmers can be divided further by the position of flagella is attached. If they are in back, such a swimmer is called *pushers* and generate an extensile flow field around it with respect to the swimming direction. If flagella are in front, such a swimmer is called *pullers* and generate a contractile flow. In Fig. 1.1, the schematic pictures of three types of swimmers are shown. Such difference in the ambient flow field results in the big difference of collective motion. Quantitative differences in flow fields are discussed in the following section.

1.4 Theoretical Formulations

In this dissertation, all the works are performed by means of three dimensional direct numerical calculation with fully resolved hydrodynamics. In this chapter, the theoretical formulations utilized are presented. First of all, we need a numerical model for

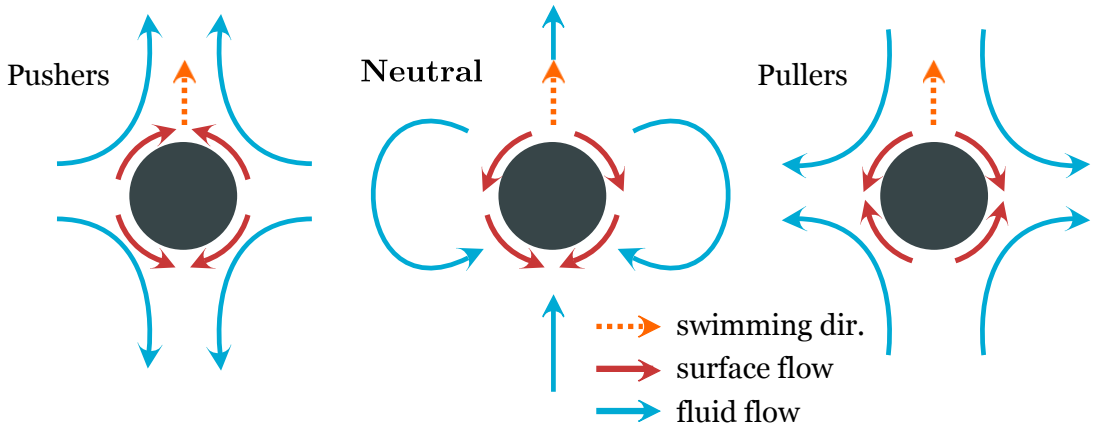

FIGURE 1.1: Schematic representation of pushers and pullers within the squirmer model. The swimming direction, and the fluid and surface flows generated by squirmers are shown.

microswimmers. For that, we employed the squirmer model. In the first subsection, this model will be introduced briefly. Because in this model, swimmers are regarded as rigid spherical objects and propel themselves as the consequence of interactions with the ambient fluid, we have to consider dynamics of solid-fluid multi-phase flow. The governing equations and the calculation scheme for the multi-phase flow are introduced in the following subsections.

1.4.1 The Squirmer Model

To perform calculation of dynamics in microswimmer dispersions, we have to model swimmers numerically. As such a numerical model, the Squirmer Model was employed in this work. This model was first introduced by Lighthill[62] and Blake[63]. This model was originally developed to describe the motion of neutral swimmers, or ciliary microorganisms, such as Volvox. Such ciliary microorganisms swim by pushing the surrounding fluid back by generating metachronal wave of synchronizingly moving cilia on thier surfaces. Lighthill and Blake model numerically this complicated motion replacing the ciliary envelope with a prescribed surface flow field $\boldsymbol{u}^s$ as

a form of a modified stick boundary on the particle surface:

$$\boldsymbol{u}^s\left(\hat{\boldsymbol{r}}\right) = \sum_{i=1}^{\infty} \frac{2}{n(n+1)} B_n P_n'(\cos\theta)\sin\theta\hat{\boldsymbol{\theta}}, \tag{1.1}$$

where $\hat{\boldsymbol{r}}$ is a unit vector directed from the center of a squirmer to a point on its surface, $\theta = \cos^{-1}\left(\hat{\boldsymbol{r}}\cdot\hat{\boldsymbol{e}}\right)$ the polar angle between $\hat{\boldsymbol{r}}$ and the swimming direction $\hat{\boldsymbol{e}}$, $\hat{\boldsymbol{\theta}}$ the unit polar angle vector at the point indicated by $\hat{\boldsymbol{r}}$. P_n' is the derivative of the Legendre polynomial of n-th order, and B_n is the magnitude of each mode. A detailed derivation of this model can be found in **Appendix A**.

Here, the activity of microswimmers is introduced in terms of the prescribed flow field. A microswimmer gives such a given flow field with respect to its own swimming direction and propels itself as the reaction of that. In this model, the assumptions are roughly only the following three: rigidity of squirmers, axisymmetry around the swimming axis and ignorance of the components in radial or azimuthal components of active flow field on the squirmer surfaces. Although the original derivation is done assuming a ciliary microorganism, because the assumptions are only general ones, this model can express far-field characteristics of the flow field around various types of swimmers well. This is also the case even for non-living swimmers like diffusiophoretic Janus particles.

In most numerical works, including the works in this dissertation, only the first two modes in Eq.(1.1) were retained, because it is enough to distinguish:

$$\boldsymbol{u}^s(\theta) = B_1\left(\sin\theta + \frac{\alpha}{2}\sin 2\theta\right)\hat{\boldsymbol{\theta}}. \tag{1.2}$$

The coefficient of the first mode, B_1, determines the swimming velocity of an isolated squirmer ($U_0 = 2/3B_1$). The coefficient of the second mode, B_2, determines the stress exerted by the particles on the fluid [79]. Using only the first two modes, the type of swimming can be modified by changing the sign of the $\alpha = B_2/B_1$ coefficient in Eq.(1.2). Negative values of α describe pushers, which generate an extensile flow

field in the propeling direction, and positive values describe pullers, which generate a contractile flow. The value of zero stands for the neutral swimmer, which swims with a potential flow field(Fig. 1.1). Because these swimming mechanisms result in distinct flow fields, different swimmers can exhibit vastly different collective motion, as we will show in this dissertation.

1.4.2 The Navier-Stokes Equations

As the governing equations for the flow field of the host fluid $\boldsymbol{u}_{\mathrm{f}}$, we employ the Navier-Stokes equation with a constant viscosity η under the incompressible condition:

$$\boldsymbol{\nabla} \cdot \boldsymbol{u}_{\mathrm{f}} = 0 \tag{1.3}$$

$$\rho_{\mathrm{f}} \left(\partial_t + \boldsymbol{u}_{\mathrm{f}} \cdot \boldsymbol{\nabla}\right) \boldsymbol{u}_{\mathrm{f}} = \boldsymbol{\nabla} \cdot \boldsymbol{\sigma}_{\mathrm{f}} \tag{1.4}$$

The stress tensor and the mass density of the host fluid are $\boldsymbol{\sigma}_{\mathrm{f}}$ and ρ_{f}. The stress tensor $\boldsymbol{\sigma}_{\mathrm{f}}$ is composed of two contributions, namely, the isotropic pressure term and the shear stress term due to the viscosity ($\boldsymbol{\sigma}'_{\mathrm{f}}$):

$$\boldsymbol{\sigma}_{\mathrm{f}} = -p\boldsymbol{I} + \boldsymbol{\sigma}'_{\mathrm{f}}, \tag{1.5}$$

$$\boldsymbol{\sigma}'_{\mathrm{f}} = \eta \left[\boldsymbol{\nabla}\boldsymbol{u}_{\mathrm{f}} + (\boldsymbol{\nabla}\boldsymbol{u}_{\mathrm{f}})^t\right], \tag{1.6}$$

where $\boldsymbol{I}$ is the unit tensor.

1.4.3 The Newton-Euler Equations

The position, velocity and angular velocity of particle i are expressed as $\boldsymbol{R}_i$, $\boldsymbol{V}_i$ and $\boldsymbol{\Omega}_i$. The time evolution of the particles follows from the Newton-Euler equations:

$$\begin{aligned} \dot{\boldsymbol{R}}_i &= \boldsymbol{V}_i, & \dot{\boldsymbol{Q}}_i &= \text{skew}(\boldsymbol{\Omega}_i) \cdot \boldsymbol{Q}_i, \\ M_\text{p} \dot{\boldsymbol{V}}_i &= \boldsymbol{F}_i^\text{H} + \boldsymbol{F}_i^\text{C}, & \boldsymbol{I}_\text{p} \cdot \dot{\boldsymbol{\Omega}}_i &= \boldsymbol{N}_i^\text{H}, \end{aligned} \tag{1.7}$$

where $\boldsymbol{Q}_i$ denotes the rotation matrix, M_p the mass, $\boldsymbol{I}_\text{p} = \frac{2}{5} M_\text{p} a^2 \boldsymbol{I}$ (with a the radius of particles) the moment of inertia and skew$(\boldsymbol{\Omega}_i)$ the skew symmetric matrix of $\boldsymbol{\Omega}_i$ defined as

$$\text{skew}\left(\boldsymbol{\Omega}\right) = \begin{pmatrix} 0 & -\Omega_3 & \Omega_2 \\ \Omega_3 & 0 & -\Omega_1 \\ -\Omega_2 & \Omega_1 & 0 \end{pmatrix}, \quad \boldsymbol{\Omega} = \begin{pmatrix} \Omega_1 \\ \Omega_2 \\ \Omega_3 \end{pmatrix}. \tag{1.8}$$

The hydrodynamic force and torque acting on particle i,$\boldsymbol{F}_i^\text{H}$ and $\boldsymbol{N}_i^\text{H}$, are calculated by the following equations:

$$\boldsymbol{F}_i^H = \int_{\boldsymbol{S}_i} \text{d}\boldsymbol{S}_i \cdot \boldsymbol{\sigma}_\text{f} \tag{1.9}$$

$$\boldsymbol{N}_i^H = \int_{\boldsymbol{S}_i} (\boldsymbol{r} - \boldsymbol{R}_i) \times (\text{d}\boldsymbol{S}_i \cdot \boldsymbol{\sigma}_\text{f}) \tag{1.10}$$

Finally, the force due to direct interactions between particles, $\boldsymbol{F}_i^\text{C}$, is taken to be a truncated Lennard-Jones type $2n - n$ potential $(n = 18)$, in order to ensure that the

excluded volume constraint is satisfied.

$$\boldsymbol{F}_i^{\mathrm{C}} = \sum_j \boldsymbol{F}_{ij}, \quad \boldsymbol{F}_{ij} = -\boldsymbol{\nabla}_i U\left(r_{ij}\right), \tag{1.11}$$

$$U\left(r_{ij}\right) = \begin{cases} 4\epsilon\left[\left(\dfrac{\sigma}{r_{ij}}\right)^{36} - \left(\dfrac{\sigma}{r_{ij}}\right)^{18}\right] + \epsilon & \left(r_{ij} \leq 2^{1/18}\sigma\right) \\ 0 & \left(r_{ij} \geq 2^{1/18}\sigma\right) \end{cases},$$

where, $\boldsymbol{F}_{ij}$ stands for the force exerted on particle i due to the pair potential between particles i and j, $\boldsymbol{\nabla}_i$ the spacial derivative with respect to the coordinate of particle i, $r_{ij} = |\boldsymbol{R}_j - \boldsymbol{R}_i|$ the distance between two particles, σ the diameter of particles and ϵ the energy unit in the system.

1.4.4 The Smoothed Profile Method

To solve the combined equations for both particles and the fluid efficiently, we utilize the Smoothed Profile Method (SPM) [80–82]. In this method, the sharp boundary between the particle and fluid domains which leads to very expensive calculation cost is not considered explicitly. Instead, a diffuse interface of finite width ξ is introduced, and the solid domain is represented via an order parameter ϕ_{p}, which takes a value of 1 in the solid domain, and 0 in the fluid domain.

$$\phi_{\mathrm{p}}\left(\boldsymbol{r}, t\right) = \sum_i \phi_{\mathrm{p}i}\left(\boldsymbol{r}, t\right), \tag{1.12}$$

as indicated by the subscript i, the order parameter field is described by the superposition of the order parameters for each particle. Using this continuous order parameter, the particle velocity can be expressed as a field variable on Cartesian grids:

$$\phi_{\mathrm{p}}\boldsymbol{u}_{\mathrm{p}}\left(\boldsymbol{r}, t\right) = \sum_i \phi_{\mathrm{p}i}\left(\boldsymbol{r}, t\right)\left[\boldsymbol{V}_i\left(t\right) + \boldsymbol{\Omega}_i\left(t\right) \times \boldsymbol{r}_i\left(t\right)\right], \tag{1.13}$$

where $\boldsymbol{r}_i = \boldsymbol{x} - \boldsymbol{R}_i$. This notation allows us to define the total velocity field which include both the fluid and the particle velocity field throughout the whole computational domain:

$$\boldsymbol{u}\left(\boldsymbol{r}, t\right) = (1 - \phi_{\mathrm{p}})\boldsymbol{u}_{\mathrm{f}} + \phi_{\mathrm{p}}\boldsymbol{u}_{\mathrm{p}}, \tag{1.14}$$

where $\boldsymbol{u}$ is the total velocity field, $(1 - \phi_{\mathrm{p}})\boldsymbol{u}_{\mathrm{f}}$ and $\phi_{\mathrm{p}}\boldsymbol{u}_{\mathrm{p}}$ the velocity field of fluid and particles, respectively. Consequently, we can build a momentum balance equation for a multi-phase system. The equation has the for of a modified incompressible Navier-Stokes equation:

$$\rho_{\mathrm{f}}\left(\partial_t + \boldsymbol{u} \cdot \nabla\right)\boldsymbol{u} = \nabla \cdot \boldsymbol{\sigma} + \rho_{\mathrm{f}}\left(\phi_{\mathrm{p}}\boldsymbol{f}_{\mathrm{p}} + \boldsymbol{f}_{\mathrm{sq}}\right), \tag{1.15}$$

$$\boldsymbol{\nabla} \cdot \boldsymbol{u} = 0, \tag{1.16}$$

The rigidity condition of particles is took into account via a body force $\phi_{\mathrm{p}}\boldsymbol{f}_{\mathrm{p}}$ and the force distribution due to the squirming motion $\boldsymbol{f}_{\mathrm{sq}}$. The brief summary of the implementation can be found in **Appendix C**.

1.5 Thesis Objectives

The collective properties of the squirmer dispersion is studied by means of the direct numerical simulation with fully resolved hydrodynamics. Although several preceding works disclosed many aspects of the problem, we still have many open questions. This dissertation is focused on two of those questions:

- the onset of the collective alignment seen in bulk
- how dynamics change under confinement

This dessertation is composed of five chapters. The first focus is discussed in **Chapter 2**, and the second focus is discussed in **Chapter 3** and **Chapter 4**.

In **Chapter 2**, the collective alignment in bulk systems are investigated. The degree of collective alignment can be measured quantitatively by the polar order parameter Q defined in Eq. (2.8). This parameter Q is known to be a function of the volume fraction of particles φ and the swimming parameter α in Eq. (1.1). The author first measured the value of Q for various sets of these two parameters thoroughly. The author confirmed that, for all the values of α, Q doesn't depend on φ so strongly at low volume fraction as reported only for the case with $\alpha = 1$ in ref.[83]. At very low volume fraction, many particle collisions are very unlikely to take place and can be ignored and particle-particle interactions can be assumed to be only binary ones. Therefore, we can expect that only binary collisions can lead to the bulk polar order. To verify this hypothesis, we composed a simplified binary collision model (BCM). The BCM can reproduce the bulk results successfully, while we see discrepancy at a specific range of α (we call this range intermediate pullers). Because at the range, strong clustering behavior is known to tale place in bulk, we consider this is an indirect evidence for the importance of many body interactions to form the polar order for the systems at the parameter range[75].

In **Chapter 3**, the collective motion of swimmers confined between flat parallel walls is presented. For a specific range of α, it is already known that we observe dynamic clustering of swimmer particles[75], though the authors did not try to quantify the dynamic property of the system. Therefore, first, we quantify such dynamic clustering behavior by measuring the dynamic structure factor. We clarified that the swimmer dispersions can show a pseudo-acoustic property, which cannot be expected for normal passive colloidal dispersions. And then, we studied the dynamics of swimmer dispersion between flat parallel walls. Under such confinements, the swimmer start to show a traveling wave-like collective motion, bouncing back and forth between the walls, only at a specific range of α. We measured the velocity of the traveling wave and compared with the sound velocity in bulk. They show a good agreement, which can be understood as an indirect evidence for that the traveling wave-like motion is

just the manifestation of the bulk pseudo-acoustic property. Interestingly, the range at which we observe the traveling wave-like motion is intermediate pullers.

In **Chapter 4**, the collective alignment of swimmers in pipes is investigated. We clarified that, in pipes, swimmers show almost the same degree of order as the values in bulk for most cases, though for several cases we see small qualitative differences. Measurement of structural information provided the onset of those differences. We also studied the dependency on the size and shape of pipes. Only a small range of pullers show an order/disorder phase transition when the size of pipe is squeezed. Interestingly, this range is again intermediate pullers. We don't see any qualitative change when we make the cross section of pipe square.

In **Chapter 5**, general conclusion is stated. The contents of this dissertation are summarized and the perspectives are presented.

2 Hydrodynamically assisted binary collisions of microswimmers

2.1 Introduction

"Active matter" encompasses a vast range of systems, from microorganisms at the microscopic scale, to humans and other mammals at the macroscopic scale[1, 2]. These active systems can show various nontrivial collective behaviors [24, 38, 60, 84–86]. Especially striking is the global ordering in the absence of any external field or leading agents[34, 83, 87–89]. In order to validate the various scenarios that have been proposed to explain such phenomena, it is important to develop model systems which can be well-controlled experimentally and efficiently simulated. For this purpose, microswimmers, such as microbes and self-propelled Janus particles, have been extensively used. It is well known that the hydrodynamic interactions play a very important role in determining the dynamics of dispersions of such microswimmers[90]. While the experimental realizations can be rather complicated, simple computational models exist which allow for direct numerical calculations, such that the full hydrodynamic effects can be accurately represented. Indeed, several simulation works on model microswimmer dispersions have recently been performed in order to study the role of hydrodynamics[66, 75, 76, 83, 84, 91]. Of particular interest for our current work is the study by Evans *et al.*[83], who investigated the conditions under which polar ordering appears. They found that the ordering does not depend strongly on the volume fraction of swimmers, but rather on the type and strength of the swimming. This result suggest that the mechanisms leading to the collective alignment do not depend on the

volume fraction, and could be explained by considering only binary collisions. Thus, in this work we investigate the onset of polar ordering by performing a detailed analysis of the collision data obtained from three dimensional (3D) simulations of swimmer suspensions with full hydrodynamics. First, we have extended the study of Evans' *et al.*, by performing direct numerical simulations (DNS) of bulk suspensions over a larger set of parameters. We have confirmed that the volume fraction dependence is weak if the volume fraction is small enough (if it is high, order/disorder phase transition takes place). Second, by simulating binary particle collision events with varying collision geometries, we have gathered comprehensive information on the changes in swimming direction that a particle feels when it undergoes a collision. If we look at changes in the relative angles of two particles after the collisions, the results show different tendencies depending on the sign of α. Pullers tend to exhibit disalignment when the incoming relative angle is small, while pushers exhibit disalignment at intermediate values. Furthermore, using this binary collision data, we have constructed a simple binary collision model (BCM) and used it to study the collective alignment of many particle systems as a function of swimming type. The BCM successfully reproduced the emergence of the polar order except for dispersions of intermediate pullers for which a strong clustering behavior is reported[75, 84].

2.2 Simulation Methods

2.2.1 The Squirmer Model

In this work, the squirmer model was used to describe the swimmers[62, 63]. Squirmers are particles with modified stick boundary conditions at their surface which are responsible for the self-propulsion. The general form is given as an infinite expansion of both radial and tangential velocity components, but for simplicity the radial terms are usually neglected and the infinite sum is truncated to second order[79]. For

spherical particles, the surface velocity is given by

$$\boldsymbol{u}^s(\theta) = B_1 \left(\sin\theta + \frac{\alpha}{2}\sin 2\theta\right)\hat{\boldsymbol{\theta}}, \tag{2.1}$$

where $\hat{\boldsymbol{\theta}}$ and $\hat{\boldsymbol{r}}$ (we use a caret to denote unit vectors) are the tangential and radial unit vectors for a given point at the surface of the particle and $\theta = \cos^{-1}(\hat{\boldsymbol{r}} \cdot \hat{\boldsymbol{e}})$ is the polar angle (since the system is axisymmetric around the swimming direction $\hat{\boldsymbol{e}}$, the azimuthal angle does not appear). The steady-state swimming velocity is determined only by the coefficient of the first mode B_1, and the ratio of the first two modes $\alpha = B_2/B_1$ determines the type and strength (stresslet) of the swimming. When α is negative, the squirmers are pushers, and generate extensile flow fields, and when it is positive, they are pullers and generate contractile flow fields. For the special case when $\alpha = 0$, we refer to the swimmers as a neutral swimmer which is accompanied by a potential flow. We call α the swimming parameter in the following.

2.2.2 Smoothed Profile Method

In order to solve for the dynamics of squirmers swimming in a viscous host fluid, the coupled equations of motion for the fluid and the solid particles needs to be considered. Particles follow the Newton-Euler equations of motion:

$$\begin{aligned} \dot{\boldsymbol{R}}_i &= \boldsymbol{V}_i & \dot{\boldsymbol{Q}}_i &= \mathrm{skew}(\boldsymbol{\Omega}_i)\cdot\boldsymbol{Q}_i \\ M_\mathrm{p}\dot{\boldsymbol{V}}_i &= \boldsymbol{F}_i^\mathrm{H} + \boldsymbol{F}_i^\mathrm{C} & \boldsymbol{I}_\mathrm{p}\cdot\dot{\boldsymbol{\Omega}}_i &= \boldsymbol{N}_i^\mathrm{H} \end{aligned} \tag{2.2}$$

where i is the particle index, $\boldsymbol{R}_i$ the position, $\boldsymbol{Q}_i$ the orientational matrix, and $\mathrm{skew}(\boldsymbol{\Omega}_i)$ the skew symmetric matrix of the angular velocity $\boldsymbol{\Omega}_i$. The hydrodynamic force $\boldsymbol{F}_i^\mathrm{H}$ and torque $\boldsymbol{N}_i^\mathrm{H}$ are computed assuming momentum conservation to guarantee proper coupling between the fluid and the particles. To satisfy the excluded volume effect, we

also introduced a repulsive interaction between particles, $\boldsymbol{F}_i^{\mathrm{C}}$, as a truncated Lennard-Jones potential with (36-18) powers. The time evolution of the fluid flow field is governed by the Navier-Stokes equation with the incompressible condition:

$$\boldsymbol{\nabla} \cdot \boldsymbol{u}_{\mathrm{f}} = 0 \tag{2.3}$$

$$\rho_{\mathrm{f}} \left(\partial_t + \boldsymbol{u}_{\mathrm{f}} \cdot \nabla\right) \boldsymbol{u}_{\mathrm{f}} = \nabla \cdot \boldsymbol{\sigma}_{\mathrm{f}} \tag{2.4}$$

$$\boldsymbol{\sigma}_{\mathrm{f}} = -p\boldsymbol{I} + \eta_{\mathrm{f}} \left\{\nabla \boldsymbol{u}_{\mathrm{f}} + \left(\nabla \boldsymbol{u}_{\mathrm{f}}\right)^t\right\} \tag{2.5}$$

where ρ_{f} is the fluid mass density, η_{f} the shear viscosity, and $\boldsymbol{\sigma}_{\mathrm{f}}$ is the Newtonian stress tensor. To couple these equations efficiently, we have used the Smoothed Profile Method (SPM), which enables us to calculate the solid/fluid two-phase dynamics on fixed grids with full hydrodynamic interactions[68, 80–82]. In the SPM, the sharp interface between the solid and fluid domains is replaced by a diffuse one with finite width ξ, and the solid phase is represented by a smooth and continuous profile function ϕ_{p}. This profile function takes a value of 1 in the solid domain, and 0 in the fluid domain. By introducing the smoothed profile function, we can define a total velocity field, $\boldsymbol{u}$, which includes both fluid and particle velocities, and is defined over the entire computational domain, as:

$$\begin{aligned} \boldsymbol{u} &= \left(1 - \phi\right) \boldsymbol{u}_{\mathrm{f}} + \phi \boldsymbol{u}_{\mathrm{p}}, \\ \phi \boldsymbol{u}_{\mathrm{p}} &= \sum_i \phi_i \left[\boldsymbol{V}_i + \boldsymbol{\Omega}_i \times \boldsymbol{R}_i\right], \end{aligned} \tag{2.6}$$

where, $\left(1 - \phi\right) \boldsymbol{u}_{\mathrm{f}}$ is the contribution from the fluid, $\phi \boldsymbol{u}_{\mathrm{p}}$ from the particle motion. The time evolution of the total flow field $\boldsymbol{u}$ obeys:

$$\begin{aligned} \boldsymbol{\nabla} \cdot \boldsymbol{u} &= 0, \\ \rho_{\mathrm{f}} \left(\partial_t + \boldsymbol{u} \cdot \nabla\right) \boldsymbol{u} &= \nabla \cdot \boldsymbol{\sigma}_{\mathrm{f}} + \rho_{\mathrm{f}} \left(\phi \boldsymbol{f}_{\mathrm{p}} + \boldsymbol{f}_{\mathrm{sq}}\right) \end{aligned} \tag{2.7}$$

where $\phi \boldsymbol{f}_{\mathrm{p}}$ is the body force necessary to maintain the rigidity of particles, and $\boldsymbol{f}_{\mathrm{sq}}$ is the force due to the active squirming motion. This method drastically reduces the computational cost.

2.3 Results

2.3.1 Bulk Polar Order

To start, we used the SPM to carry out DNS studies of bulk swimmer dispersion in 3D at varying volume fraction φ and swimming type α. We use a cubic system of linear dimension of 64Δ, with Δ the grid spacing. The viscosity and the mass density of the host fluid, μ, ρ_f are set to one, such that the unit of time is $t_0 = \rho_f \Delta^2/\mu$. The particle diameter σ and the interface thickness ξ are 4Δ and 2Δ respectively. We used a random initial configuration for the particle positions and orientations, and varied the number of particles N_{p} from 500 to 4000, which correspond to a range of volume fraction $0.06 \lesssim \varphi \lesssim 0.5$. To quantify the degree of collective alignment, we calculate the polar order parameter P[75, 83]

$$P = \left\langle \frac{1}{N_{\mathrm{p}}} \left| \sum_{i}^{N_{\mathrm{p}}} \hat{\boldsymbol{e}}_i \right| \right\rangle, \tag{2.8}$$

where $\hat{\boldsymbol{e}}_i$ is the swimming direction of particle i, N_{p} the number of particles and angular brackets denote an average over time (after steady state has been reached). Typical simulation snapshots for disordered ($P \simeq 0$) and ordered ($P \simeq 1$) systems are given in Fig. (2.1a). We note that even for a completely random distribution of orientations, the polar order defined by Eq. (2.8) will not be exactly 0, and will depend slightly on the number of particles, as $P_0 = 1/\sqrt{N_{\mathrm{p}}}$, where P_0 represents the polar order value at isotropic phase. This means that the base values for isotropic systems will differ depending on the precise value of N_{p} that is used; P_0 converges to zero only in the limit of $N_{\mathrm{p}} \to \infty$.

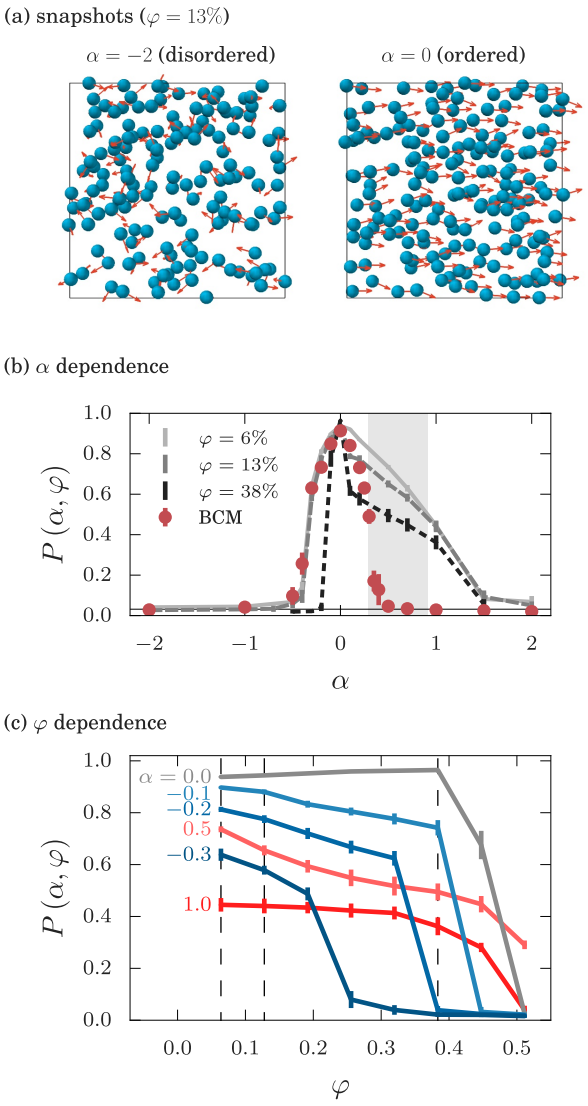

FIGURE 2.1: (a) Simulation snapshots for disordered ($\alpha = -2$) and ordered ($\alpha = 0$) states. The arrows give the direction of motion, and only a subset of the particles have been drawn. (b) The α dependency of the polar order $P(\alpha, \varphi)$ for $\varphi = 6\%$ (solid line), 13% (light dashed line) and 38% (dark dashed line). Results for the simplified binary collision model are given as circles. (c) The φ dependency of $P(\alpha, \varphi)$ for several values of α. Dashed vertical lines indicate the volume fractions of $6, 13$ and 38% used in (a) and (b).

The polar order parameter P is a function of only the volume fraction of particles φ and the swimming parameter α[83]. First, we investigated α dependency. The results are illustrated in Fig. (2.1b), for volume fractions $\varphi = 6\%$ ($N_{\mathrm{p}} = 500$),13% ($N_{\mathrm{p}} = 1000$) and 38% ($N_{\mathrm{p}} = 3000$). All the results show a similar tendency and are in agreement with preceding woks[75, 83]: P has a maximum at $\alpha = 0$, independent of φ, and decreases with increasing value of $|\alpha|$. In addition, the P for pushers decays faster than that of pullers as the magnitude of α is increased. For non-pusher $\alpha \geq 0$, the volume fraction dependence of P is not very large and at least the qualitative ordering tendency is the same; but for weak pushers (for example $\alpha \approx -0.3$), we observe a significant drop in the value of P, or an order/disorder phase transition when the volume fraction increases. The volume fraction dependence can be seen clearly in Fig. (2.1c), where we have plotted the values of P over the entire volume fraction range for six different swimmers ($\alpha = -0.3, -0.2, -0.1, 0, 0.5, 1$). Evans *et al.* have previously reported such a volume fraction dependence for $\alpha = 1$ [83]. To understand the dependence of P on the swimming type α, in particular the different behaviors seen for pushers and pullers, it is useful to compare them against the results obtained for neutral swimmers $\alpha = 0$, which show the highest degree of alignment. As seen in Figure2.1 (c), the order parameter for $\alpha = 0$ shows two distinct regimes: for $\varphi \lesssim 0.4$ there is little variation; for $\varphi \gtrsim 0.4$ there is a drastic drop in the order parameter to $P = 0$ (P_0). The same behavior is observed for pushers, although both of the degree of ordering and the critical volume fraction φ_c (where the order parameter falls to zero) are both reduced (higher $|\alpha|$ resulting in lower P and φ_c). In contrast, pullers show a gradual decrease only in the degree of order depending on $|\alpha|$. Interestingly, intermediate pullers ($\alpha = 0.5$) maintain a non-zero order parameter over the entire volume fraction range we have considered (all other systems giving $P \approx P_0$ at the highest φ). We believe this anomalous behavior for the intermediate pullers can be related to the strong clustering behavior that gives rise to density inhomogeneities[75, 84]. Note that because the number of particles are sufficiently large (even for the system with

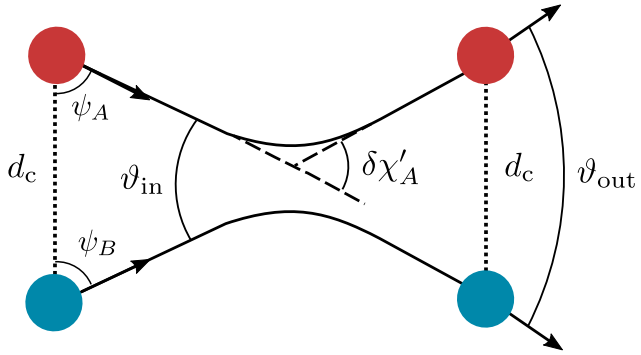

FIGURE 2.2: Schematic representation of the collision geometry.

the smallest volume fraction which corresponds to $N_p = 500$, the value of P_0 is less than 0.05), the decays in P are not related to the fact that we use different values of N_p.

2.3.2 Binary Collision Model

Taking into account the fact that at low volume fractions, two body interactions are dominant, we can expect that the observed polar order in bulk is due to binary collisions. To verify this, we first conducted an intensive analysis on the binary collision of squirmers with varying values of α. Then, we tried to construct a simplified binary collision model (BCM) using the data obtained by this analysis. We note that a similar binary collision analysis for pullers has been done by Ishikawa *et al.*[92]. We have extended their work to pushers and neutral swimmers and made direct comparison between the BCM and the bulk DNS results. For this, we have carried out 3D DNS for a pair of particles with various collision geometries and α values. Given the symmetry of the problem, the two particles will move in a 2D plane (defined by the two orientation vectors). We considered collisions of two particles labeled A and B. The precise parametrization we have used to describe the collision is given in Fig. 2.2, where three sets of angles have been defined, ψ_j, $\delta\chi_j$ ($j \in \{A, B\}$ is the particle label) and $\vartheta_{in/out}$. The initial configuration of the system is specified by ψ_j, the angles between the direction of motion and the center-to-center distance vector at the initial state. These

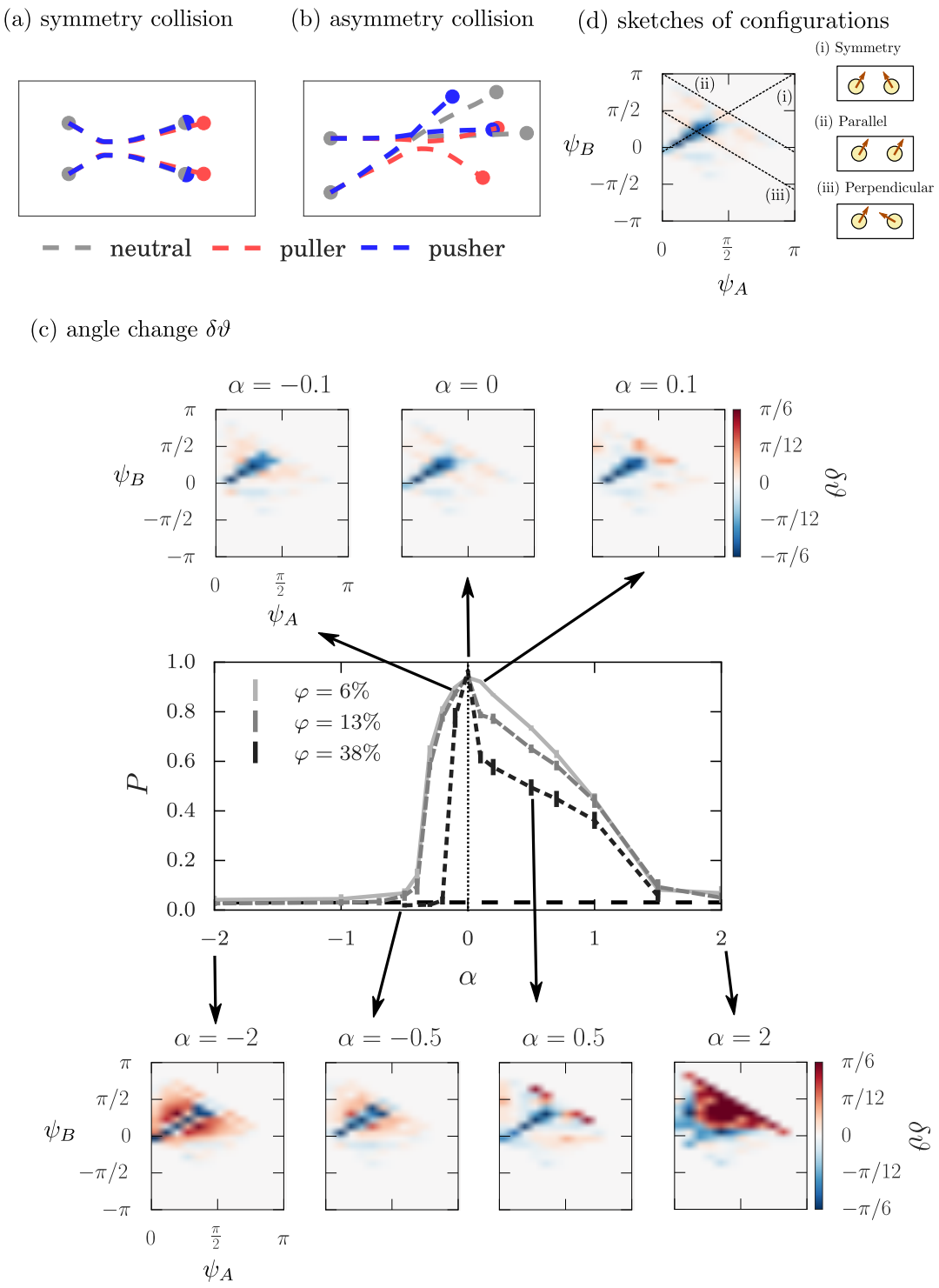

FIGURE 2.3: (a-b) Typical trajectories of collisions of neutral swimmer ($\alpha = 0$; colored as gray), pullers ($\alpha = 0.5$; red) and pushers ($\alpha = -0.5$; blue) for (a) a symmetric collision and (b) an asymmetric one. (c) Change in the relative angle between the particles during collisions, $\delta\vartheta = \vartheta_{\text{out}} - \vartheta_{\text{in}}$, as a function of the initial orientations, ψ_{A} and ψ_{B}. Results of bulk polar order measurement are also shown ($\varphi = 6, 13$ and 38%). In density maps, red colors mean positive values or the disalignment effect and blue colors negative or the aligning effect. (d) Sketches for the characteristic configurations in the density maps in (c).

angles determine whether particles start swimming towards or away from each other. The information for the change in the swimming direction of each particle is given by $\delta\chi_j$. Then, the relative orientation of particles when the collision event starts/ends is represented by $\vartheta_{\mathrm{in/out}}$. Due to the long-range nature of the hydrodynamic interactions, there is no unique way to define a "collision" between particles. Therefore, we define a characteristic distance d_c that is the threshold distance under which particles are considered to be colliding: a collision event has started when the distance between the two particles becomes less than d_c, and it lasts until the distance exceeds this value (see Figure 2.2). Thus, d_c should be large enough that hydrodynamic interactions can be neglected when the distance between the particles exceeds d_c.

The parameters for the binary collision is determined as follows. The initial particle distance was set to $d_0 = 16\Delta = 4\sigma$, and the collision threshold to $d_c = 15\Delta$. The value of d_c is determined to be big enough so that we can safely ignore the hydrodynamic interactions if the particle-particle distance is greater than d_c (above this value, particles hardly change their orientations). The value of d_0 is determined so that swimmers have obtained their steady state velocity when the inter-particle distance becomes d_c. The initial geometry was varied by changing ψ_j in intervals of $\pi/12$, for $0 \leq \psi_A \leq \pi$ and $-\pi \leq \psi_B \leq \pi$. To take into account the symmetry of the system, we label one of the particles (A) as a reference particle, and take $\psi_A \geq 0$, while ψ_B is defined as

$$\psi_B = \mathrm{sign}\left(\mathcal{P}_{AB} \cdot \hat{\boldsymbol{e}}_A\right) \mathrm{sign}\left(\mathcal{P}_{AB} \cdot \hat{\boldsymbol{e}}_B\right) \left|\arccos\left(\hat{\boldsymbol{r}}_{AB} \cdot \hat{\boldsymbol{e}}_B\right)\right| \tag{2.9}$$

where $\boldsymbol{r}_{AB} = \boldsymbol{r}_B - \boldsymbol{r}_A$, $\mathcal{P}_{AB}$ is the projection operator (with $\mathcal{I}$ the identity operator)

$$\mathcal{P}_{AB} = \mathcal{I} - \hat{\boldsymbol{r}}_{AB}\hat{\boldsymbol{r}}_{AB} \tag{2.10}$$

and $\mathrm{sign}(x) = 1$ for $x \geq 0$ and $\mathrm{sign}(x) = -1$ for $x < 0$. As mentioned above, we use a caret to denote unit vectors. Thus, ψ_B is defined as positive if both particles

are swimming towards the same side with respect to the center-to-center line between particles. We note that only combinations of ψ_i which meet $\hat{\boldsymbol{e}}_{AB} \cdot \hat{\boldsymbol{r}}_{AB} < 0$ can lead to "collisions", where $\boldsymbol{e}_{AB} = \hat{\boldsymbol{e}}_B - \hat{\boldsymbol{e}}_A$. Three-dimensional simulations for the binary collision were performed using the same system parameters as for the bulk simulations presented above.

The results of the binary collision analysis are summarized in Fig. 2.3. Fig. 2.3(a) and (b) show typical trajectories and Fig. 2.3(c) shows changes in the relative angle between the swimming direction of the two particles after the collisions, $\delta\vartheta = \vartheta_{\mathrm{out}} - \vartheta_{\mathrm{in}}$. In the following, we define a symmetric collision as a collision in which $\psi_A = \psi_B$ (Fig. 2.3(a)). Density maps show the values of $\delta\vartheta$ as a function of the initial angles, ψ_j. In Fig. 2.3(d), the schematic representations of three characteristic initial configurations are shown: (i)symmetric, (ii)parallel, (iii)perpendicular. Although the parallel configuration does not lead to a collision, it is useful to identify the corresponding region in the density plots shown in Fig. 2.3(c). The values of the polar order in bulk are again shown to make the connection between the bulk and binary collision dynamics clear. As shown in Fig. 2.3 (a) and (b), different values of α lead to different particle trajectories, resulting in different patterns for $\delta\vartheta$ (Fig. 2.3 (c)). Note that for symmetric collisions, the trajectories of neutral swimmers and pushers are quite close to each other (Fig. 2.3 (a)). The results of $\delta\vartheta$ in systems of pushers and pullers can be easily understood by considering their deviation from the results for neutral swimmers ($\alpha = 0$). The neutral swimmers show strong aligning behaviors only when the collision is symmetric, and just small absolute values of $\delta\vartheta$ otherwise. If we look at the results for pullers ($\alpha > 0$), we can perceive that, in the case of $\alpha = 0.1$, disalignment effects are detected at small relative incoming angles. Such disalignment effects becomes stronger with the increase in the absolute value of α, as shown in the subplots for $\alpha = 0.5, 2$. On the other hand, in the cases of pushers ($\alpha < 0$), disalignment effects are seen at relatively large incoming angles. For pushers, as well as for pullers, the increase in the absolute value of α leads to stronger disalignment effect. In this way,

measuring only $\delta\vartheta$, we can observe different tendencies between pushers and pullers. These tendencies seem to be a consequence of the complicated hydrodynamic interactions, and it is impossible to understand intuitively from the view point of the flow field which a single swimmer generates.

To implement a simple binary collision model using the collision data obtained from the DNS, it is necessary to measure the changes in the single particle orientations, $\delta\chi_j$. For this, from the comprehensive DNS data for binary collisions, we have determined $\delta\chi_j$ for all the collisions, as

$$\delta\chi_j = \arcsin\left(\hat{\boldsymbol{z}}_\chi \cdot \left(\hat{\boldsymbol{e}}_j^{\mathrm{in}} \times \hat{\boldsymbol{e}}_j^{\mathrm{out}}\right)\right), \tag{2.11}$$

where the superscript "in/out" refers to the value at the moment when a collision starts/ends, $\hat{\boldsymbol{z}}_\chi = \frac{\hat{\boldsymbol{e}}_j^{\mathrm{in}} \times \hat{\boldsymbol{e}}_{j'}^{\mathrm{in}}}{|\hat{\boldsymbol{e}}_j^{\mathrm{in}} \times \hat{\boldsymbol{e}}_{j'}^{\mathrm{in}}|}$ and j' refers to the particle which is colliding with particle j.

Finally, in order to investigate whether the polar order seen in bulk systems can be explained only by binary collisions, we constructed a binary collision model. Here, we have necessarily introduced two simplifications. First, we assume 2D systems. And second, we consider only binary collisions, and use the statistics of collision angles obtained from the present DNS. Because we are assuming very dilute system such that the information of the position doesn't matter anymore, the particles have only the information about the orientations. Under these simplifications, we calculated the polar order of the system of BCM using the following simple algorithm. At each step of the simulation, we randomly choose two particles (let's say particles i and i'). The selected particles will experience a "collision", which will change their orientations

according to the statistics obtained from the binary collision analysis:

$$\begin{aligned}\chi_i\left(s+1\right) &= \chi_i\left(s\right) + \delta\chi_i,\\ \chi_{i'}\left(s+1\right) &= \chi_{i'}\left(s\right) + \delta\chi_{i'},\\ \chi_k\left(s+1\right) &= \chi_k\left(s\right),\end{aligned} \tag{2.12}$$

where subscript k stands for the particles which are not selected to collide. Values of $\delta\chi_{i/i'}$ follow the conditional probability distribution of the pair of $\delta\chi_i$ and $\delta\chi_{i'}$ when the relative incoming angle ϑ_{in} is given: $P\left(\delta\chi_i, \delta\chi_{i'}|\vartheta_{\mathrm{in}}\left(i,i'\right)\right)$, where $\delta\vartheta\left(i,i'\right)$ means the relative incoming angle between particles i and i'. Because there is the information about only the orientation in the BCM, the orientation update algorithm is based only on the relative incoming angle $\bar{\vartheta}_{\mathrm{in}}$, and does not depend on the collision parameter (which cannot be defined in this model system) or other geometrical information. Such stochastic collisions will be repeated until the steady state is achieved. In this work, we used $N_{\mathrm{p}} = 1000$ for BCM. No noise term is included. After a sufficiently large number of collisions, the system reaches a steady state, with a constant polar order. We conducted calculations using this BCM for various values of α, while keeping the value of $N_{\mathrm{p}} = 1000$ the same. The results for these simulations are plotted in Fig. (2.1b) as red circles, lines representing the results from the bulk DNS with $\varphi = 6\%, 13\%$, and 38%. The results from the BCM and those from the bulk DNS under dilute condition ($\varphi = 6\%$) are in good agreement with each other for non-pullers ($\alpha \leq 0$). This indicates that the appearance of polar order can be understood just in terms of binary collision events for non-pullers. For pullers, we see a growing deviation: the larger α becomes, the larger the deviation becomes. For $\alpha \geq 0.4$, even qualitatively the results are different: in the BCM, the order is collapsed. The shaded gray region in the figure marks the parameter range in which we have observed strong clustering in bulk systems[84]; it is precisely in this regions where the results do not coincide with the BCM. This can be seen as indirect evidence for the importance of

multi-body interactions for the collective alignment of intermediate pullers. In pipes, we also observed similar indirect evidence for the importance of the many body interactions for the polar order formation in systems of intermediate pullers[93]. There, we reported that the polar order in the system of intermediate pullers is suppressed when the pipe size becomes small, while such a order/disorder transition cannot be observed for other types of swimmers. We consider such a phase transition indicates that intermediate pullers require clusters with a certain characteristic size to maintain the polar order. In small pipes, they are unable to form such clusters and seem to fail maintaining the order. Though several efforts have been dedicated to verify the importance of binary collisions to explain the polar order formation for various systems both experimentally and numerically [33, 94–96], the presented work is the first successful attempt to conduct such analysis considering full hydrodynamics.

2.4 Conclusion

Using DNS for squimer dispersions, we have investigated the emergence of polar ordering and its dependency on the particle volume fraction φ and swimming strength α. In agreement with a previous work[83], we see that the volume fraction dependence is rather weak, and the ordering depends mostly on α when φ is small enough. Still, we observed novel volume fraction dependencies for $|\alpha| < 1$. In particular, intermediate pullers show no decay of the polar order even at a very high volume fraction, at which all other swimmers show a decay. We believe this anomalous behavior at such a high volume fraction reflects the already-known strong clustering characteristics[75, 84]. On the other hand, weak pushers show a decay of the polar order even at small volume fractions.

We conducted a detailed analysis of the binary collision dynamics of two swimmers and looked at the changes in the relative orientation of two swimmers after the collisions. The results show different qualitative disaligning tendencies between

pusher and puller: pullers show disaligning effects at small relative incoming angles while pushers exhibit at relatively large angles. The absolute value of α changes only the magnitude of disalignment, and the tendency is determined by the sign. Such an analysis also enabled us to construct a simple binary collision model which is able to reproduce the polar ordering seen in the bulk DNS for pushers and neutral swimmers. Thus, it seems binary collisions are enough to explain the appearance of long range polar ordering for these types of swimmers. We note that intermediate pullers exhibit a clear discrepancy between the DNS results and the BCM; however, this occurs in the parameter range where strong clustering behavior is also observed. This can be seen as indirect evidence that in intermediate puller systems, clustering due to many body interactions plays an important role. In other words, the origin of the polar order formation can be different, depending on the specific type of swimming. In particular, the mechanism responsible for the clustering of intermediate pullers is still an open question.

3 Purely hydrodynamic origin for swarming of swimming particles

3.1 Introduction

Active matter systems such as groups of microorganisms, birds or fish often form swarms or flocks, and typically show complex collective behavior [97–99]. Of special interest for scientific study are active microscopic systems, e.g. microorganisms or Janus particles, because they are particularly well suited for experiments. Understanding the collective dynamic behavior of these systems can be useful for both science and industrial applications, for example, to explain the formation of biofilms [100] or to design targeted drug delivery systems [101]. Such systems typically exist under some type of confinement, which has been shown to exert a strong influence on the collective behavior [39–42, 102]. So far, most analysis of such systems have either neglected hydrodynamic interactions or only considered them in a far field approximation [40, 41, 59, 60], even though it is known that the hydrodynamic interactions can dramatically affect the physical properties of the systems [90]. Theoretically, it's impossible to take into account the full hydrodynamic interactions in many body systems, and numerically it's very computationally expensive. While several studies have succeeded in including hydrodynamic interactions [66, 75, 83], only few have focused on the collective dynamic behavior of 3D active systems under confinement.

We have conducted direct numerical calculations for 3D systems of spherical swimmers in a host viscous fluid with fully resolved hydrodynamics, and provide three novel findings. First, we elucidated that the swarming behavior (or dynamic transient

clustering behavior) in bulk puller dispersion, which Alarcon and Pagonabarraga reported [75], can be understood as a pseudo-sound mode, as evidenced by the dynamic structure factor. Second, under the confinement of two flat parallel walls, we find collective motion of swimmers with traveling wave characteristics, which propagates back and forth between the walls. Although similar traveling wave-like motion has already been observed in systems with explicit alignment interactions between the particles [85, 103], here we show that hydrodynamic interactions alone are enough to exhibit this behavior. Third, we show evidence that this traveling wave-like behavior can be regarded as a manifestation of the pseudo-sound mode of the system. Crucial to observe this wave-like behavior are the strength and type (pushers vs. pullers) of swimming, not the degree of global alignment.

3.2 Simulation Methods

3.2.1 The Squirmer Model

As the numerical model of microswimmers, the Squirmer Model was employed. In this model, a self-propelled particle is modeled as a spherical object with a modified stick boundary condition at its surface [62, 63]:

$$\boldsymbol{u}^s\left(\hat{\boldsymbol{r}}\right) = \sum_{i=1}^{\infty} \frac{2}{n(n+1)} B_n P_n'(\cos\theta) \sin\theta \hat{\boldsymbol{\theta}}, \tag{3.1}$$

where $\hat{\boldsymbol{r}}$ is a unit vector directed from the center of a squirmer to a point on its surface, $\theta = \cos^{-1}\left(\hat{\boldsymbol{r}} \cdot \hat{\boldsymbol{e}}\right)$ the polar angle between $\hat{\boldsymbol{r}}$ and the swimming direction $\hat{\boldsymbol{e}}$, $\hat{\boldsymbol{\theta}}$ the unit polar angle vector. P_n' is the derivative of the Legendre polynomial of n-th order, and B_n is the magnitude of each mode. Here, the radial deformation has been ignored, so this surface velocity has only the tangential component, and is responsible for the self-propulsion of the swimmers.

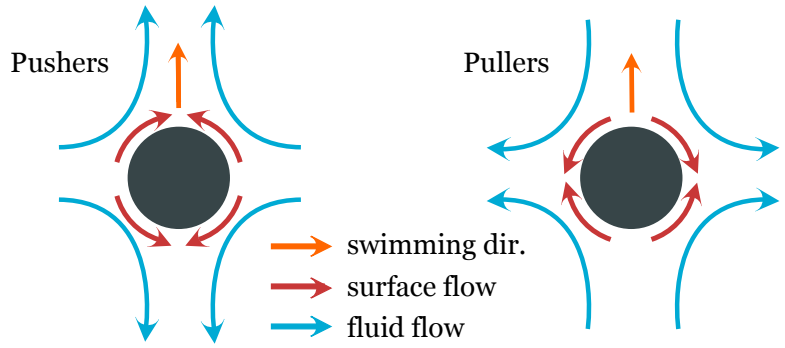

FIGURE 3.1: Schematic representation of pushers and pullers within the squirmer model. The swimming direction, and the fluid and surface flows generated by squirmers are shown.

In this work, only the first two modes in Eq.(3.1) were retained:

$$\boldsymbol{u}^s(\theta) = B_1 \left(\sin\theta + \frac{\alpha}{2} \sin 2\theta \right) \hat{\boldsymbol{\theta}}. \tag{3.2}$$

The coefficient of the first mode, B_1, determines the swimming velocity of an isolated squirmer ($U_0 = 2/3B_1$). The coefficient of the second mode, B_2, determines the stress exerted by the particles on the fluid [79]. Using only the first two modes, the type of swimming can be modified by changing the sign of the $\alpha = B_2/B_1$ coefficient in Eq.(3.2). Negative values of α describe pushers, which generate an extensile flow field in the propeling direction, and positive values describe pullers, which generate a contractile flow (Fig. 3.1). Because these two swimming mechanisms result in distinct flow fields, different swimmers can exhibit vastly different collective motion, as we will show in this paper.

3.2.2 Smoothed Profile Method (SPM)

In this study, the squirmer model is incorporated into the Smoothed Profile Method (SPM) [80–82], which is an efficient calculation scheme for solid/fluid two phase dynamics problems with full hydrodynamics. In this method, the sharp boundary between the solid and fluid domains is not considered explicitly. Instead, a diffuse interface of finite width ζ is introduced, and the solid domain is represented via an order

parameter ϕ_{p}, which takes a value of 1 in the solid domain, and 0 in the fluid domain. Using this continuous order parameter, all the physical quantities can be expressed as field variables on Cartesian grids, and the calculation cost can be reduced drastically. As the governing equations for the total fluid, we employ a modified incompressible Navier-Stokes equation:

$$\begin{aligned} \rho_{\mathrm{f}}\left(\partial_t + \boldsymbol{u}\cdot\nabla\right)\boldsymbol{u} &= \nabla\cdot\boldsymbol{\sigma} + \rho_{\mathrm{f}}\left(\phi_{\mathrm{p}}\boldsymbol{f}_{\mathrm{p}} + \boldsymbol{f}_{\mathrm{sq}}\right), \\ \boldsymbol{\nabla}\cdot\boldsymbol{u} &= 0, \\ \boldsymbol{u} &= (1-\phi_{\mathrm{p}})\boldsymbol{u}_{\mathrm{f}} + \phi_{\mathrm{p}}\boldsymbol{u}_{\mathrm{p}}, \\ \phi_{\mathrm{p}}\boldsymbol{u}_{\mathrm{p}} &= \sum_i \phi_{\mathrm{p}i}[\boldsymbol{V}_i + \boldsymbol{\Omega}_i\times\boldsymbol{R}_i], \end{aligned} \tag{3.3}$$

where $\boldsymbol{u}$ is the total velocity field, $(1-\phi_{\mathrm{p}})\boldsymbol{u}_{\mathrm{f}}$ and $\phi_{\mathrm{p}}\boldsymbol{u}_{\mathrm{p}}$ the velocity field of fluid and particles, respectively. The position, velocity and angular velocity of particle i are expressed as $\boldsymbol{R}_i$, $\boldsymbol{V}_i$ and $\boldsymbol{\Omega}_i$. The stress tensor and the mass density of the host fluid are $\boldsymbol{\sigma}$ and ρ_{f}. The body force generated from the rigidity condition of particles is expressed as $\phi_{\mathrm{p}}\boldsymbol{f}_{\mathrm{p}}$, and $\boldsymbol{f}_{\mathrm{sq}}$ stands for the force distribution resulting from the squirming motion (the effects due to the slip-velocity $\boldsymbol{u}^s$ are contained in $\boldsymbol{f}_{sq}$) [68]. The time evolution of the particles follows from the Newton-Euler equations:

$$\begin{aligned} \dot{\boldsymbol{R}}_i &= \boldsymbol{V}_i, & \dot{\boldsymbol{Q}}_i &= \mathrm{skew}(\boldsymbol{\Omega}_i)\cdot\boldsymbol{Q}_i, \\ M_{\mathrm{p}}\dot{\boldsymbol{V}}_i &= \boldsymbol{F}_i^{\mathrm{H}} + \boldsymbol{F}_i^{\mathrm{C}}, & \boldsymbol{I}_{\mathrm{p}}\cdot\dot{\boldsymbol{\Omega}}_i &= \boldsymbol{N}_i^{\mathrm{H}}, \end{aligned} \tag{3.4}$$

where $\boldsymbol{Q}_i$ denotes the rotation matrix, M_{p} the mass, $\mathrm{skew}(\boldsymbol{\Omega}_i)$ the skew symmetric matrix of $\boldsymbol{\Omega}_i$, and $\boldsymbol{F}_i^{\mathrm{H}}$ and $\boldsymbol{N}_i^{\mathrm{H}}$ are the hydrodynamic force and torque acting on particle i. The force due to direct interactions between particles, $\boldsymbol{F}_i^{\mathrm{C}}$, is taken to be a truncated Lennard-Jones potential, in order to ensure that the excluded volume constraint is satisfied. See refs [68, 80–82] for more detailed information of this method.

3.3 Results

3.3.1 Bulk Behaviors

We conducted simulations of swimmer dispersion systems in a three dimensional domain. Throughout this paper, the diameter σ and the boundary thickness ζ of the squirmers are 4Δ and 2Δ, respectively, where Δ is the grid spacing and the unit length. The B_1 parameter in Eq. (3.2) is set as 0.375. The shear viscosity η and the fluid mass density ρ_{f} are set to one, and the unit time is then expressed as $\rho\Delta^2/\mu$. The particle Reynolds number of an isolated squirmer $Re^0 = \rho_{\mathrm{f}} U_0 \sigma/\eta$ is set equal to one. The Reynolds number in the dispersion will be different from Re^0 due to a decrease in the propelling velocity with increasing volume fraction. We have ignored any effects due to thermal fluctuations. No external force is exerted, and the systems are buoyancy free.

We first calculated the dynamics of swimmers in bulk cubic systems. The linear dimension of the computational domain is $L = 64\Delta$ and the number of swimmers is 1043 (volume fraction of 13 %). Periodic boundary conditions are set in every direction. We conducted simulations for various α values in order to investigate the effect of α on the dynamics. Alarcon and Pagonabarraga have considered a similar setup and showed that puller suspensions with $\alpha = 0.5$ can exhibit swarming behavior [75] . The swarming is purely hydrodynamic in origin, as no direct aligning interactions are included. In [75], the swarming behavior was characterized in terms of the local structure (generalized radial distribution functions and the local density fluctuations), but no attempt was made to quantitatively analyze the collective dynamic behavior of the system. To accomplish this, we have calculate the dynamic structure factor $S(\boldsymbol{k}, \omega)$, which is just the Fourier transform of the density-density correlation function in both

space and time[104]:

$$\rho_{\boldsymbol{k}}(t) = \sum_{i=1}^{N} \exp\left[-i\boldsymbol{k}\cdot\boldsymbol{R}_i(t)\right] \tag{3.5}$$

$$S\left(\boldsymbol{k},\omega\right) = \frac{1}{2\pi}\int_{-\infty}^{\infty}\frac{1}{N}\langle\rho_{\boldsymbol{k}}\left(t\right)\rho_{-\boldsymbol{k}}\left(0\right)\rangle\exp\left(i\omega t\right)\mathrm{d}t \tag{3.6}$$

where $\boldsymbol{k}$ is the wave vector and ω the angular frequency.

The spherically averaged (over shells of wave vectors) structure factors of the systems for $\alpha = \pm 0.5$ are shown in Fig. 3.2. Shifted peaks were observed for both systems, pullers($\alpha = 0.5$) and pushers($\alpha = -0.5$). These peak positions ω_{shift} follow a Brillouin-like dispersion relation:

$$\omega_{\text{shift}} = c|\boldsymbol{k}| \tag{3.7}$$

where c is a coefficient which has the dimension of velocity (in the case of normal Brillouin peaks, c represents the sound velocity). We can therefore say that these systems possess pseudo-acoustic mode dynamics, or a sound-like propagation mode for the density. No Rayleigh-like peaks were observed for small wave vectors, probably because the Brillouin-like peaks are much stronger (for wave vectors of large magnitude, Rayleigh-like peaks are recovered). The sound velocity of this pseudo-acoustic mode can be calculated from the dispersion relation, shown at the bottom of Fig. 3.2 and Eq. (3.7) (note that the values in Fig. 3.2 (c) are all nondimensionalized). We don't see any difference between the sound velocities of pushers and pullers, although the peak intensities show very big differences.

3.3.2 In Confinement

As we show below, the pseudo-sound behavior presented above can have dramatic consequences for systems under confinement, which is relevant to most experimental realizations of active matter systems. We have calculated the dynamics of $N = 2607$

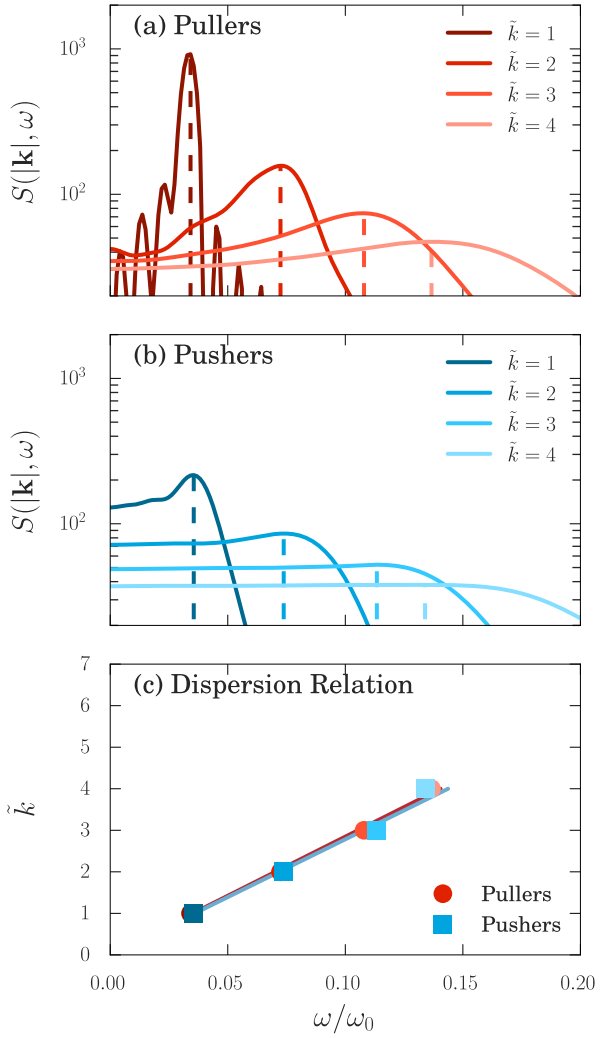

FIGURE 3.2: The calculation results for the spherically averaged Dynamic Structure Factor (DSF) $S(\boldsymbol{k},\omega)$, where $\boldsymbol{k} = \frac{2\pi}{L}\tilde{\boldsymbol{k}}$ is the wave vector, and ω the angular frequency (normalized by $\omega_0 = 2\pi/t_0$, where $t_0 = \sigma/U_0$). The top two figures show the simulation results for the DSF of (a) pullers at $\alpha = 0.5$, and (b) pushers at $\alpha = -0.5$. The bottom figure (c) shows the relation between wave vectors and the positions of the Brillouin peaks. Dashed lines in (a) and (b) show the positions of peaks.

swimmers in a $64\Delta \times 160\Delta \times 64\Delta$ rectangular system (volume fraction of 13%, the same value as the previous simulations in the bulk system). The computational domain is periodic in the x and z direction, but confined between two flat parallel walls along the y direction; at $y = 1\Delta$ and 159Δ. These walls are made of 2048 spherical particles which are pinned and unable to move or rotate from the initial positions and orientations. The wall particles are regularly spaced and are defined to have the same diameter as the squirmers. The initial configuration of swimmers was randomly determined with respect to both position and orientation. We again conducted simulations for various values of α. We have calculated the time evolution of the local density ρ, polar order $Q_{\rm l}$ and velocity $v_{\rm l}$, as a function of distance from the walls. Here, $Q_{\rm l} = \langle \hat{e}_y \rangle_{\rm plane}$ and $\bar{v}_{\rm l} = \langle V_y/U_0 \rangle_{\rm plane}$, where $\hat{e}_y$ and V_y are the components of $\hat{\boldsymbol{e}}$ and $\boldsymbol{V}$ perpendicular to the walls, and $\langle \cdot \rangle_{\rm plane}$ denotes an ensemble average over all particles in parallel slabs of width 2Δ. Fig. 3.3 shows the results of the systems with $\alpha = \pm 0.5$ (see movies S1 and S2 in Sec. 3.6.1). For pullers ($\alpha = 0.5$), the time evolution of the density, polar order and velocity are shown, while for pushers ($\alpha = -0.5$), only density is shown. Only the pullers show large density fluctuations; pushers show no such behavior. First, the pullers build up two distinct traveling waves which bounce back and forth between the walls. Gradually, as one wave begins to dominate, they merge into a single propagating wave. We also considered different wall separations, and found that such propagating wave-like motion can only be observed if the wall separation is larger than the characteristic size of this propagating flock. In our simulations, the threshold is $W/\sigma \simeq 40$, where W is the wall separation. In fig. 3.4, the traveling wave velocity is plotted for several different wall separations. They are quantitatively the same and there is no clear separation dependence (see Appendix for the wave velocity measurement scheme). The value of the sound velocity for the pullers calculated from the dispersion relation is also shown. This pseudo-sound velocity is quantitatively the same as the wave propagating velocity in confinement, though slightly higher. Thus, we believe that this traveling wave-like behavior under confinement is due mainly to

the intrinsic pseudo-acoustic properties of the swimmers. In this case, the role of the walls is to break the symmetry and provide a finite domain over which the density waves can develop.

We have performed simulations for volume fractions up to 30%, with smaller/larger wall surface areas, and different alpha values ($-5 \leq \alpha \leq 5$). The traveling wave-like motion is always observed for pullers in the range $0 < \alpha < 1$.

Although it is known that pullers can show swarming behavior in bulk [75], the traveling wave-like motion under confinement we present here was unexpected and surprising for the following two reasons. First, the walls can strongly affect the hydrodynamic interactions between particles [39–42, 102]. Actually, for small separations, we see suppression of this traveling-wave like motion, while, for sufficiently large separations, walls allow us to see constructive interference. Second, even if the swarming can be observed, it is possible that the particles will prefer to swim parallel to the walls. Indeed, this is exactly what happens for in the case of neutral swimmers ($\alpha = 0$) (S3 in Sec. 3.6.1).

3.4 Discussion

Now we would like to discuss the origin of the pseudo-acoustic mode. From Fig. 3.3, we can see that the particles show local polar order and move as a group collectively, even though individual particles seem to move independently from their neighbors. (for individual particles motion, see movie S4 in Sec. 3.6.1). In puller systems, this cooperative swimming as a group can be understood as the origin of the pseudo-acoustic mode, or density propagation. Now let us consider a simplified set-up in which swimmers are placed along a straight line with a non-regular distribution, and oriented parallel to this line, in such a way they will start swimming in the same direction (S5 and S6 in Sec. 3.6.1; simulations are conducted full-3D domain). In this situation, due to the contractile flow along the swimming direction, pullers attract each other

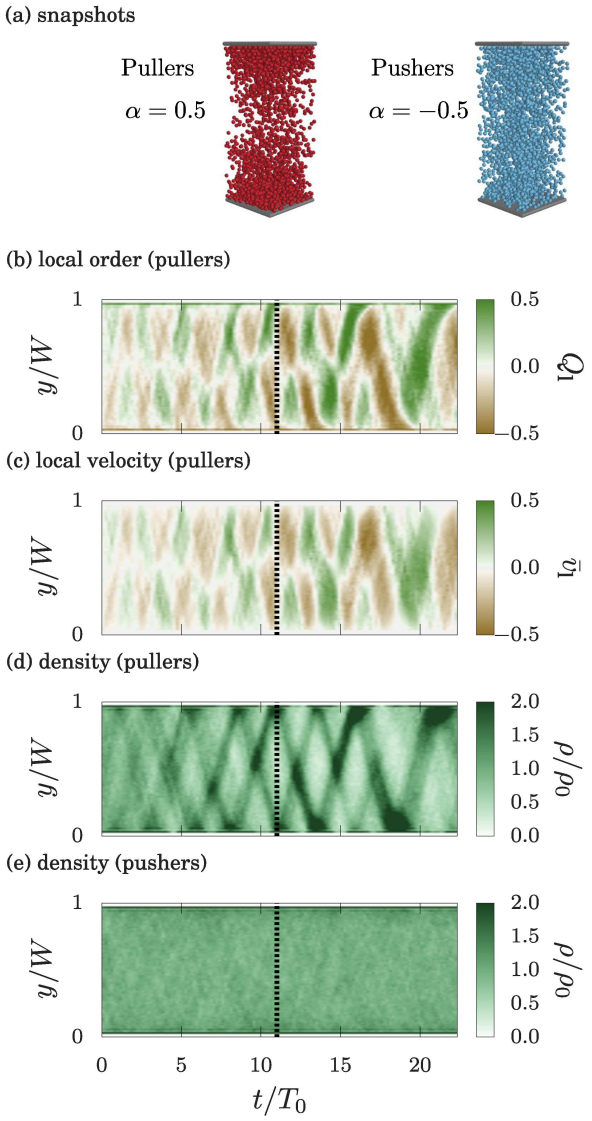

FIGURE 3.3: Simulation results for pullers and pushers ($\alpha = \pm 0.5$) at volume fraction of 13% and wall separation $W/\sigma = 40$. (a) Simulation snapshots, (b) local order of pullers defined as $Q_l = \langle \hat{e}_y \rangle_{\text{plane}}$, (c) local velocity of pullers in y direction (perpendicular to the walls) defined as $\bar{v}_l = \langle V_y/U_0 \rangle_{\text{plane}}$ (d,e) plane averaged density for pushers and pullers at each height y/W. The density is normalized by the global average value, ρ_0, and time and velocity are normalized by $T_0 = W/U_0$ and U_0, where W represents the separation of parallel flat walls. The snapshots are of around $t = 11T_0$, which is marked by dashed line.

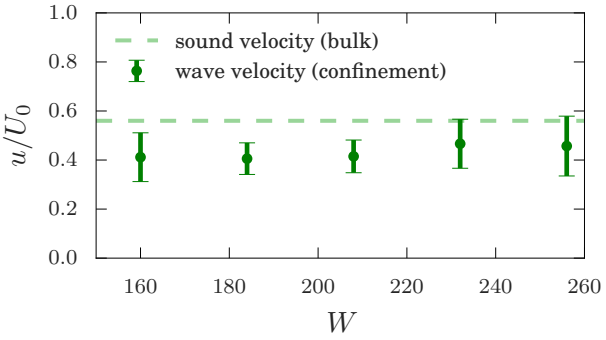

FIGURE 3.4: The traveling wave velocity of confined systems as a function of wall separation W. The sound velocity of the bulk system is also shown. Here, only puller results are shown, as pushers don't show wave-like behavior. All the values are normalized by U_0.

and tend to enhance the longitudinal mode of density fluctuations, resulting in the formation of flocks. On the other hand, pushers show the opposite tendency, which suppresses the longitudinal fluctuations. In the systems of interest in this paper, the situation is much more complicated. However, we can still say that the appearance of the large density fluctuations we present depends on the local interaction rather than on the global order. Actually, we never observed large fluctuations for pushers, even though the global polar order ($Q = \langle \frac{1}{N} | \sum_i \hat{\boldsymbol{e}}_i | \rangle$) [75, 83] could be similar to pullers with $\alpha = 0.5$. On the other hand, pullers with various values of α ($0.3 \leq \alpha \leq 0.9$) do show traveling-wave like motion in confinement.

Let us consider another simplified set-up, in which the swimmers are placed along a straight line with the same non-regular distribution, but oriented perpendicular to the line. (S7a and S8a in Sec. 3.6.1). In the case of pullers, the differences in the inter-particle separations, which can be regarded as transverse density fluctuations, are actually suppressed by the hydrodynamic interactions. We can understand this as follows: pullers aligned parallel to each other (side-by-side) tend to repel themselves due to the contractile flow field they generate. As for pushers, we observe a cyclic bouncing back motion between neighboring particles, in which the separation between the

two most distant particles is increased. Thus, for pushers, we observed a kind of transverse instability, although it is much weaker and more short-living compared to the longitudinal one seen for pullers. Both pushers and pullers show segregation of the particles into two distinct line clusters, one behind the other. We consider this is due to the small inter-particle separation. Actually, if we take as a starting configuration for a new simulation one of these line-clusters (from the steady state of the puller system), we don't see any such separation (see S7b and S8b in Sec. 3.6.1), but we still see a great difference in the density fluctuations between pullers/pushers.

In order to rule out the possibility that this traveling wave-like motion is due to inertial effects, we also conducted simulations with a smaller Reynolds number ($Re_0 = 0.1$). The system showed the same collective behavior. We can therefore conclude that this behavior is purely hydrodynamic in origin.

As mentioned above, the neutral system ($\alpha = 0$) shows a unique behavior due to absence of the second mode in the r.h.s. of Eq. 3.2. In bulk, a flocking state will soon develop, in which all particles swim in the same direction, with the same velocity. As there are only relatively small changes in their relative positions, the intermediate scattering function will exhibit a very long relaxation time. Therefore, it is practically impossible to calculate the corresponding dynamic structure factors, which are shown in Fig. 3.2 for pullers and pushers. Instead, we use the average swimmer velocity in the flocking state to define the characteristic velocity of the neutral swimmer dispersions. The average velocities in bulk (volume fraction of 13%) and confinement ($W = 160\Delta$, volume fraction of 13%) are $0.76U_0$ and $0.95U_0$ respectively; the velocity in confinement is considerably larger than that in bulk. Regarding the increased velocity for the neutral swimmers, as shown by Li *et. al.* [66], the swimming velocity can be both increased or decreased due to the presence of a wall (depending on Re and the swimming parameter α). In summary, the dynamics under confinement are qualitatively the same as those of bulk systems, even though the flocking velocity can differ.

We would like to mention previous works using theoretical continuum models which have shown similar results, although it is difficult to make a one-to-one comparison with our work. Simha and Ramaswamy predicted, using a continuum model, that active matter suspensions with polar order can show sound like propagation modes[59]. Ezhilan *et al.* studied a similar continuum model [60]. They reported that pushers show a stronger instability in their concentration field, contrary to our results that pullers have much higher Brillouin-like peaks and are more likely to show density fluctuations. However, these continuum models only include far field hydrodynamics, whereas we considered the full hydordynamic interactions and the finite size of the particles. As reported in preceding works, the near-field hydrodynamic interactions strongly affect the collective dynamics[76, 105]. In particular, most of the theoretical works assume an elongated shape for the particles, which leads to local alignment via steric interactions, while we consider spherical particles.

The recent work by Zöttl and Stark[91] is related to ours, but deals with quasi-2D systems under strong confinement (small separation of walls) and high volume fraction, which are quite different conditions from those of the present work. The values of the swimming strength, are also crucially different from ours, focusing mainly on strong pushers/pullers $|\alpha|> 1$ Although they have also considered neutral particles $\alpha = 0$, they have not considered any pusher/puller system with $|\alpha|< 1$, which is where we observe the traveling wave-like motion (as we have mentioned above, systems with $\alpha = 0$ behave in a completely different manner from systems with $\alpha \neq 0$). Not surprisingly, we are able to observe quite different dynamic behavior. The works by Lefauve and Saintillan [106] and Tsang and Kanso [107] also refer to traveling wave-like behavior in systems of microswimmers. They reported density shock waves at the front and back of the flocks, which we could not observe in our simulations. This is likely due to the addition of the background flow and strong Hele-Shaw type confinement used in these works. Actually, Desreumaux *et al.* reported that even passive colloids can show shock waves when they are driven by a

background flow [108].

3.5 Conclusion

In conclusion, we confirmed, using direct numerical simulations with full hydrodynamics, that swimmers can show pseudo-acoustic properties in bulk. Also, swimmer dispersions confined between flat parallel walls can exhibit a traveling wave-like motion, if the wall separation is big enough. Furthermore, the propagating velocity of this traveling wave does not depend on the separation, and this value is in quantitative agreement with the pseudo-sound velocity in bulk. Judging from these results, the presence of the walls does not strongly affect the dynamics. Rather, they just play a passive role, breaking the symmetry of the system and providing a finite domain over which the density wave can develop, thus allowing the pseudo-acoustic property to manifest itself.

This kind of phenomenon cannot be expected in conventional passive colloidal dispersions, since such density fluctuations would be suppressed due to viscous damping[109]. In future works, we will consider complex wall geometries, such as gear shaped objects [40, 41] and circular systems [102]. Based on our current results, we expect that spherically shaped particles, without any apparent alignment interaction, can generate non trivial collective motion due solely to hydrodynamic interactions.

3.6 Appendix

3.6.1 Simulation movies

See Supplemental Material at http://www-tph.cheme.kyoto-u.ac.jp/p/oyama/movies.html for the simulation movies, cited by "SM#" in the main text.

3.6.2 Wave velocity measurement

To calculate the wave velocity, we proceeded as follows. First, we divide the system into slabs of thickness $0.5a$ parallel to the walls and calculate the local order parameter, Q_l, and perpendicular velocity, $\bar{v}_l$, in each slab. In Fig. 3.3, we show Q_l, $\bar{v}_l$ and ρ as functions of height and time. We clearly see evidence of a propagating high density flock, which appears as a dark diagonal band in the density plot. We identify the moving flock by looking for regions with $Q_l > Q_t$ and $\bar{v}_l > v_t$, where Q_t and v_t are the threshold for each variable. The threshold for the local order parameter, Q_t, is set at 0.5 and we consider that the slab is occupied by the flock if Q_l is higher than this value. In addition, we use a threshold v_t for the velocity, in order to remove the data near the wall boundaries where the average local velocity should vanish. We set v_t at $0.04U_0$, which is less than 10% of the wave velocity (or the sound velocity).

4 Hydrodynamic alignment of microswimmers in pipes

4.1 Introduction

Self-propelled particles (SPPs) are attracting more and more interest as a representative example of out-of-equilibrium systems[1, 3, 11, 12, 14, 16, 55, 110]. Examples of SPPs range from the microscopic scale, with algae and bacteria, to the macroscopic scale, which includes all animals, and recently, even artificial SPPs have been constructed, such as active Janus particles[111, 112]. Among them, microswimmers are of particular interest, since they are suited to well-controlled lab experiments[38], and have many potential applications, for example, as targeted drug delivery systems. It is known that nontrivial motion, like the collective alignment of the swimming direction or the dynamic clustering can be observed, even for systems where particles interact with each other only through hydrodynamic interactions and excluded volume effects[75, 83, 84]. Such collective motion is mainly due to the complicated hydrodynamic interactions, and cannot be predicted only from knowledge of the single particle dynamics. That these hydrodynamic interactions are strongly affected by the presence of confining walls is well known. Experimentally, Das *et al.* reported that when a single Janus particle swims in the vicinity of a wall, it tends to swim along the wall[113]. Lushi *et al.* investigated the collective dynamics of a bacterial dispersion inside a circular confinement, and reported that the system spontaneously shows an anomalous double-vortex motion[38]. Regarding the numerical studies with full hydrodynamics, while most of them have focused on the dynamics in bulk, several

works have reported on the dynamics of microswimmers near walls or under confinement[38, 66, 67, 84, 91, 113]. The dynamics under confinement is usually studied using flat parallel walls or cylindrical pipes. We would like to note that works with nonspherical swimmers[114] or chemically actuated swimmers[115] with confinements have been reported. Though, in the presenting work, we focus on spherical swimmers which self-propel by utilizing only the hydrodynamic interactions between the ambient fluid, so-called "squirmers". In this description of microswimmers, different types of swimming mechanisms can be expressed only by changing one parameter, which we refer to as the swimming parameter. As examples of the work using the same swimmer description as ours, Li and Ardekani have investigated the static structure between flat parallel walls and shown evidence for the accumulation of particles near the wall[66]. Zöttl and Stark have studied a similar system[91], but under extreme confinement, and observed a dense-dilute phase separation, which is not seen in bulk. Our previous work[84] has focused on the dynamic properties of a microswimmer dispersion confined between flat parallel walls with relatively large separations (compared to the size of the particles). In ref. [84], we observed a traveling wave-like collective motion for a specific range of swimming parameters and densities. Though such a motion would seem to be a consequence of confinement, we clarified that it can be understood as the manifestation of the pseudo-acoustic properties of the system, which is already observed in bulk. As shown here, even for the same confinement geometry, the dynamic behavior can be considerably different depending on the strength of the confinement (i.e., the wall separation). Therefore, how the dynamics changes under confinement is a very difficult question to answer.

Although we can find several works on the collective dynamics in bulk or between flat parallel walls, the many particle dynamics of swimmers in pipes has not been extensively studied so far. This is the focus of the present work. Intuitively, we can expect that for big enough pipes, the dynamics will be the same as for bulk systems. Therefore, we focus on the dynamics in pipes with diameters comparable to that of the

particle, where we can expect nontrivial behaviors which are different from those in bulk. In fact, in the work by Zhu *et al.*, which deals with the single particle dynamics in a pipe with diameter three times the particle diameter, it is reported that different dynamical modes can be observed depending on the swimming type and strength[67]. Taking into account the possibility that the size and the shape of the pipe affect the dynamic properties, in this work, we investigated the collective alignment effects, known as the polar order formation, varying the four main parameters, namely, the pipe size, the pipe shape, the volume fraction and the type of the swimmers. Regarding the polar order formation in many particle systems, the behavior in pipes is mostly the same as in bulk, if the pipe size is large enough. However, for a specified region of the parameter space, we observed clear wall effects, which we investigated by measuring the structural information of the dispersion. In addition, we observed the pipe size dependent order/disorder phase transition only for the parameters at which clustering behaviors have been reported in bulk and between flat walls[75, 84]. In this work, we also measured the bulk structural information and obtained indirect evidences which states that the clustering is important for the collective alignment for a specific range of parameters.

4.2 Simulations

4.2.1 The Squirmer Model

As the numerical model for microswimmers, we employed the squirmer model[62, 63]. In this model, the microswimmers are expressed by rigid particles with a prescribed flow field on their surface. The general squirmer model is expressed in the form of an infinite expansion, with components along the tangential, radial, and azimuthal directions. However, utilizing only the first two modes of the tangential field, following Eq. (4.1), already enables us to model different types of swimmers, namely

pushers, pullers and the neutral swimmers.

$$\boldsymbol{u}^s(\theta) = B_1 \left(\sin\theta + \frac{\alpha}{2} \sin 2\theta \right) \hat{\boldsymbol{\theta}}, \tag{4.1}$$

where, $\boldsymbol{u}^s$ denotes the surface flow field, $\hat{\boldsymbol{r}}$ is a unit vector directed from the center of the particle to a point on its surface, $\theta = \cos^{-1}(\hat{\boldsymbol{r}} \cdot \hat{\boldsymbol{e}})$ the polar angle between $\hat{\boldsymbol{r}}$ and the swimming direction $\hat{\boldsymbol{e}}$, and $\hat{\boldsymbol{\theta}}$ is the tangential unit vector at $\hat{\boldsymbol{r}}$. This simplified squirmer model has been widely used and is known to lead to a wide variety of non-trivial phenomena[110]. The coefficient of the first mode, B_1, determines the swimming velocity of an isolated squirmer ($U_0 = 2/3B_1$), and that of the second mode, B_2, determines the stresslet[92]. The ratio between the coefficients of the two modes, $\alpha = B_2/B_1$ in Eq. (4.1), determines the swimming type and strength. In the following, we call α the swimming parameter. Negative values of α represents pusher-type swimmers, which swim with an extensile flow field in the swimming direction, and positive values describe puller-type swimmers, which swim with a contractile flow. A value of $\alpha = 0$ stands for a neutral swimmer, which generates a potential flow field. In this model, the prescribed flow field is assumed to be an axisymmetric pure tangential one and the particle is rigid and spherical. These are the only assumptions employed to derive the model. Therefore, it is thought that this model can capture even the features of the artificial microswimmers like Janus particles even though it was originally intended to describe ciliary propulsion of micro-organisms.

4.2.2 Smoothed Profile Method (SPM)

In this work, we investigate the dynamics of squirmer particles swimming in a viscous fluid. For this, we must solve the combined fluid-solid problem. The Newton-Euler

equations of motion govern the particle trajectories:

$$\dot{\boldsymbol{R}}_i = \boldsymbol{V}_i \qquad \dot{\boldsymbol{Q}}_i = \mathrm{skew}(\boldsymbol{\Omega}_i) \cdot \boldsymbol{Q}_i \tag{4.2}$$
$$M_\mathrm{p}\dot{\boldsymbol{V}}_i = \boldsymbol{F}_i^\mathrm{H} + \boldsymbol{F}_i^\mathrm{C} \qquad \boldsymbol{I}_\mathrm{p} \cdot \dot{\boldsymbol{\Omega}}_i = \boldsymbol{N}_i^\mathrm{H}$$

where the subscript i means the particle index, $\boldsymbol{R}$ the position vector, $\boldsymbol{Q}$ the orientation matrix, skew($\boldsymbol{\Omega}$) the skew symmetric matrix of the angular velocity $\boldsymbol{\Omega}$, and $\boldsymbol{F}^\mathrm{H}$ and $\boldsymbol{N}^\mathrm{H}$ the hydrodynamic force and torque though which the particle dynamics is coupled with the flow field. The interaction between particles, $\boldsymbol{F}^\mathrm{C}$, is also considered to prevent overlapping of the particles by employing a repulsive Lennard-Jones type potential, the Weeks-Chandler-Andersen potential. As the powers for the potential, we adopted 36-18. The time evolution of the fluid flow field is described by the Navier-Stokes equation with the incompressible condition:

$$\boldsymbol{\nabla} \cdot \boldsymbol{u}_\mathrm{f} = 0 \tag{4.3}$$

$$\rho_\mathrm{f} \left(\partial_t + \boldsymbol{u}_\mathrm{f} \cdot \nabla\right) \boldsymbol{u}_\mathrm{f} = \nabla \cdot \boldsymbol{\sigma}_\mathrm{f} \tag{4.4}$$

$$\boldsymbol{\sigma}_\mathrm{f} = -p\boldsymbol{I} + \eta \left\{\nabla \boldsymbol{u}_\mathrm{f} + (\nabla \boldsymbol{u}_\mathrm{f})^t\right\} \tag{4.5}$$

where $\boldsymbol{\sigma}_\mathrm{f}$ is the stress tensor, ρ_f the mass density of the host fluid and η the shear viscosity. In order to solve these simultaneous equations efficiently, we employed the Smoothed Profile Method (SPM). In the SPM, we don't treat the sharp boundary between the solid and fluid phases explicitly. Instead, a diffuse interface with thickness of ξ is introduced, and the phase boundaries are expressed by using a continuous order parameter ϕ, which takes the value of one in the solid domain, zero in the fluid domain, and intermediate values within the diffuse interface region. Employing this method, all the physical quantities can be expressed in terms of continuous fields defined over the whole computational domain. The total velocity field $\boldsymbol{u}$ which includes

both particle and fluid velocity information can be expressed like:

$$\begin{aligned} \boldsymbol{u} &= (1-\phi)\,\boldsymbol{u}_{\mathrm{f}} + \phi \boldsymbol{u}_{\mathrm{p}}, \\ \phi \boldsymbol{u}_{\mathrm{p}} &= \sum_i \phi_i \left[\boldsymbol{V}_i + \boldsymbol{\Omega}_i \times \boldsymbol{R}_i\right] \end{aligned} \tag{4.6}$$

where, $(1-\phi)\,\boldsymbol{u}_{\mathrm{f}}$ and $\phi \boldsymbol{u}_{\mathrm{p}}$ are the contribution of the fluid flow field and the particle motion to the total velocity field. And now, the time evolution of the total velocity field $\boldsymbol{u}$ is governed by a modified incompressible Navier-Stokes equation:

$$\rho_{\mathrm{f}} \left(\partial_t + \boldsymbol{u} \cdot \boldsymbol{\nabla}\right) \boldsymbol{u} = \boldsymbol{\nabla} \cdot \boldsymbol{\sigma}_{\mathrm{f}} + \rho_{\mathrm{f}} \left(\phi \boldsymbol{f}_{\mathrm{p}} + \boldsymbol{f}_{\mathrm{sq}}\right), \tag{4.7}$$

$$\boldsymbol{\nabla} \cdot \boldsymbol{u} = 0, \tag{4.8}$$

where $\phi \boldsymbol{f}_{\mathrm{p}}$ is the body force guaranteeing the rigidity condition of particles and $\boldsymbol{f}_{\mathrm{sq}}$ the force needed to maintain the squirming motion. By doing this, the calculation cost can be reduced by orders of magnitude. See refs.[68, 80–82] for more detailed information about this method.

In this work, the dynamics of swimmers in pipes are considered. For this, we have to model solid walls numerically. Within the SPM scheme, the walls can be expressed by assemblies of particles which are pinned and not allowed to translate or rotate. By this, the stick boundary at the wall surface is guaranteed. The wall particles are placed uniformly and have the same diameter as the swimmer particles. Because we consider various shapes and sizes of pipes, the number of particles composing the walls varies depending on the pipe. We note that the surface of the confinement has a non-zero roughness because the walls are represented by a collection of discrete particles.

4.2.3 System Parameters

Using the calculation method presented above, we conducted three dimensional direct numerical simulations (DNS) of microswimmer dispersions confined in pipes.

The diameter σ and interface thickness ξ of particles are set to be $\sigma = 6\Delta$ and $\xi = 2\Delta$ respectively, where Δ stands for the grid spacing. The excluded volume effect between particles (both wall-particle and particle-particle) is implemented by $\boldsymbol{F}^{\mathrm{C}}$ in Eq. (4.2). Regarding the parameters in Eq. (4.1), we set $B_1 = 0.25$ for all the calculations and varied α to study the α dependency of the dynamics. This value of B_1 gives a particle Reynolds number of one for an isolated swimmer (as presented above, only the value of B_1 determines the steady state velocity). The symmetry axis of the pipe is defined to be parallel to the y axis. In what follows, we refer to the confinement with a circular cross section as a pipe, and the one with a rectangular cross section as a duct. Regardless of the size or shape of confinement, the length of the pipe L is set to be $L = 128\Delta \approx 20\sigma$ and the periodic boundary condition is set in this direction (in other directions, the system is enclosed by the confinement, and the system size in those directions depends on the confinements). Unless stated otherwise, thermal fluctuations are ignored throughout this paper. We will consider the pipe with diameter $D = 8\sigma$ to be our reference confinement system, where D is defined as the diameter of the pipe containing the free space available to the particle. In this article, first we present the dynamics of this reference system, and then those obtained for different pipe sizes. For the definition of the particle volume fraction we used:

$$\varphi = \frac{N_{\mathrm{p}} V_{\mathrm{p}}}{V_{\mathrm{M}}}, \tag{4.9}$$

where $V_{\mathrm{p}} = \frac{1}{6}\pi\sigma^3$ is the volume of one particle and V_{M} the volume in which particle centers can move freely:

$$V_{\mathrm{M}} = \frac{\pi}{4} L D^2. \tag{4.10}$$

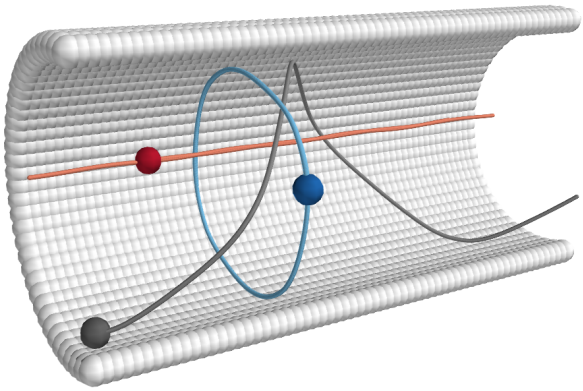

FIGURE 4.1: Typical trajectories of the three different dynamical modes. (a) Pusher's rotational orbit ($\alpha = -1$; represented by blue) (b) Neutral swimmer's spiral trajectory ($\alpha = 0$; represented by gray) (c) Puller's rectilinear path ($\alpha = 1$; represented by red). Note that these three trajectories are obtained using the same initial position and orientation. Only the trajectories in steady states are shown. White particles represent the particles composing the pipe. To facilitate the visualization, only half of the pipe-particles are drawn.

4.3 Results & Discussions

4.3.1 Single-particle Dynamics in a Pipe

The single-particle dynamics in a pipe has been studied by Zhu *et al.*, who reported that distinct dynamical modes are observed depending on the swimming parameter α[67]. In order to confirm the qualitative agreement within our calculation scheme, we performed calculations with one particle for various values of α. As mentioned above, in this section, we consider only a pipe with diameter $D = 8\sigma$, the reference system. After a sufficiently long time, all the cases achieve steady states. Typical trajectories of the steady states are shown in Fig. (4.1). Here, the result of the cases with $\alpha = 0, \pm 1$ are shown. The dynamical mode at the steady state depends only on the sign of α and is independent of the absolute value: a pusher gets trapped in an orbit and shows constant rotation at a fixed y position, while a puller shows rectilinear translation along the pipe axis at a constant distance from the wall. A neutral swimmer achieves the combined dynamics of the two modes: spiral motion along the pipe

axis (rotation + translation). These results are consistent with the results in ref.[67]; although the trajectories of the pushers are not analyzed in detail in this work.

As shown here, the single-particle dynamics are affected by the confinement. The intriguing thing is that the dynamical mode is determined only by the sign of α, independent of the absolute value. Regarding the bulk collective properties, it is known that such an absolute value dependence exists. For example, the polar order P (Eq. (4.11)), often used to measure the degree of collective alignment, strongly depends on the absolute value of α.

$$P = \left\langle \frac{1}{N_{\mathrm{p}}} \left| \sum_{i}^{N_{\mathrm{p}}} \hat{\boldsymbol{e}}_i \right| \right\rangle, \tag{4.11}$$

where, N_{p} stands for the number of particles in the system and $\hat{\boldsymbol{e}}_i$ the unit swimming direction vector of particle i. This quantitative measure of the degree of order, P, takes a value of one when the system is completely aligned, and $P \approx P_0 = 1/\sqrt{N_{\mathrm{p}}}$ when the system is completely isotropic. The value of P decreases as the absolute value of α increases[75, 83, 84].

4.3.2 Many Particle Dynamics in a Pipe

We next performed calculations for many particle systems in a pipe of diameter $D = 8\sigma$. The polar order P is a function of both the swimming parameter α, and the volume fraction of the particles φ. First of all, let us recapitulate the behaviors in bulk systems[116]. If we measure the polar order as a function of α at a certain value of the volume fraction, the value of P decreases with the increase in the absolute value of α, as stated above. This tendency is asymmetry with respect to positive and negative α values: with negative values (pushers), showing a faster decay. If we regard P as a function of φ for a certain value of α, the behavior is most easily understood in terms of the deviations from the volume fraction dependence for neutral swimmers.

This reference system ($\alpha = 0$) shows two regimes: for $\varphi \leq 0.4$, the values are constant; for $\varphi \geq 0.4$ there is an abrupt drop in the order parameter to $P \approx P_0$. A similar behavior is observed for pushers (negative values of α). At small volume fractions, they show only a weak decrease with increasing volume fraction, and then exhibit an abrupt drop at a critical volume fraction φ_c. Pushers show a decrease both in the degree of ordering and the value of φ_c. Pullers, on the other hand, show a decrease only in the degree of ordering, and systems intermediate pullers ($\alpha = 0.5$, for example) even maintain the order at very high volume fractions, where all other systems show $P \approx P_0$. Specifically, we stress that in bulk, the system with $\alpha = 1$ shows a nonzero value of P up to very high volume fractions.

We conducted simulations over a wide range of combinations of α and ϕ in the pipe. From the particle trajectories obtained from these simulations, we then calculated the polar order parameter along the y direction (the direction of the pipe elongation),

$$P_{\mathrm{y}} = \left\langle \frac{1}{N_{\mathrm{p}}} \left| \sum_{i}^{N_{\mathrm{p}}} e_i^{\mathrm{y}} \right| \right\rangle , \tag{4.12}$$

where e_i^{y} is the y-component of the swimming direction $\hat{\boldsymbol{e}}$ of particle i and the angular brackets denote a time average. In Fig. 4.2, the values of P_{y} are shown as a function of α. Here, the values of P in bulk are also shown using a dashed line. The volume fraction is $\varphi \approx 0.25$ for both cases ($N_{\mathrm{p}} = 500$ in the pipe, $N_{\mathrm{p}} = 550$ in bulk). In Fig. 4.2, we see a good match between results in bulk and those in pipe over a wide range of α. However, for $0.5 < \alpha \leq 1.5$, we see clear differences. In pipes, over this α range, the values of P are reduced compared to the bulk results, with the gap increasing with an increase in the absolute value of α. Finally, at $\alpha \simeq 0.9$, the dynamics show a qualitatively different behavior: in the pipe, $P_{\mathrm{y}} = P_0$ which means the order is completely lost.

In Fig. 4.3, detailed results representing the volume fraction dependency are shown

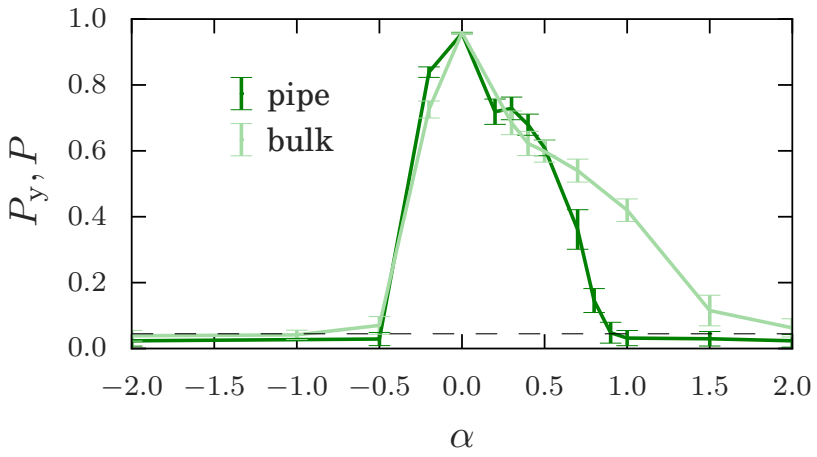

FIGURE 4.2: The polar order parameter P_y in a pipe with diameter 8σ as a function of the swimming parameter α. The polar order P in bulk systems is also shown as a light-colored line. The volume fraction is $\varphi \approx 0.25$ in both cases. The dashed line stands for the value of P_0.

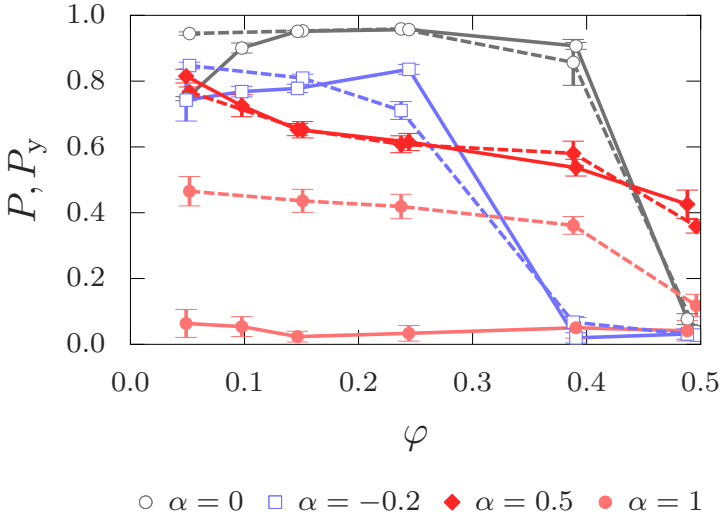

FIGURE 4.3: The polar order parameter P_y in a pipe with diameter 8σ as a function of volume fraction and swimming parameter. The polar order P in bulk systems is also shown using dashed lines.

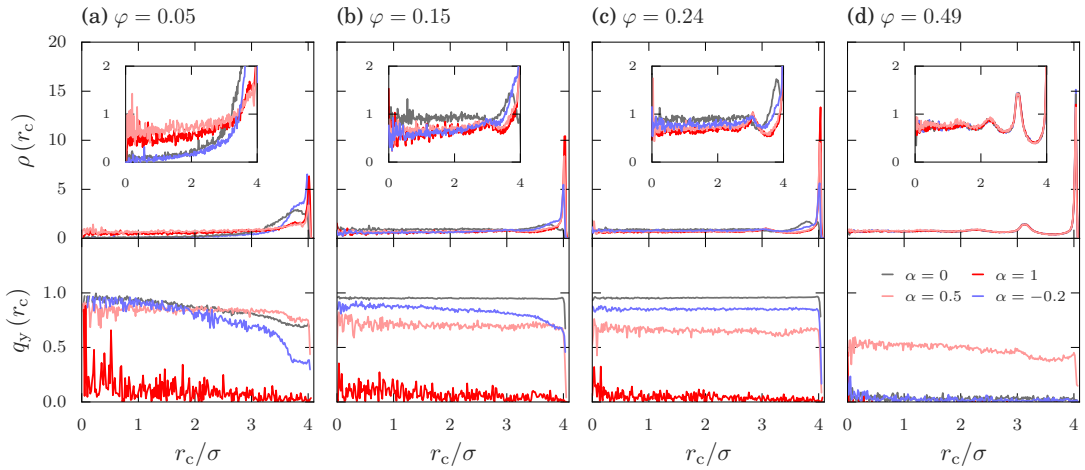

FIGURE 4.4: The single-body density distribution ρ and the local polar order p_y for various combinations of φ and α. Insets show the images magnified in the y direction. The horizontal axis represents the distance from the pipe axis normalized by the particle diameter.

for four different values of α, which exhibit qualitatively different behavior, $\alpha = -0.2, 0, 0.5, 1$. For the volume fraction, we consider six different values in the range of $0.05 \leq \varphi \leq 0.5$ (corresponding to $100 \leq N_\mathrm{p} \leq 1150$). As before, the bulk results are shown as dashed lines in Fig. 4.3. Although the results in the pipe are qualitatively the same as those in bulk for some of the cases, several differences can be perceived. In the case with $\alpha = 0$, the value of P at the smallest volume fraction, $\varphi \approx 0.05$ shows an obvious reduction in the pipe compared to the bulk. At other volume fractions, the values match reasonably well. In the case of $\alpha = -0.2$, we observe a similar reduction at the lowest volume fraction. In addition, in this case ($\alpha = -0.2$), we observe a rise in P_y at intermediate volume fraction ($\varphi \approx 0.25$). Finally, in the case with $\alpha = 1$, we see no polar order ($P_y \simeq 0$) at any of the volume fractions considered. Lastly, we note that in the case of $\alpha = 0.5$ we observed a very good agreement between the results in bulk and those in the pipe over the whole range of volume fractions.

In order to understand these differences from the view point of the structures inside the pipe, we measured the following two functions, the local density $\rho(r_c)$ and the local polar order along the y-axis $p_y(r_c)$. These are defined as a function of the

perpendicular distance r_{c} from the symmetry axis of the pipe:

$$\rho\left(r_{\mathrm{c}}\right)=\left\langle \frac{N_{\mathrm{c}}\left(r_{\mathrm{c}}\right)}{2\rho_0\pi r_{\mathrm{c}}L\Delta r_{\mathrm{c}}}\right\rangle, \tag{4.13}$$

$$p_{\mathrm{y}}\left(r_{\mathrm{c}}\right)=\left\langle \frac{1}{N_{\mathrm{c}}\left(r_{\mathrm{c}}\right)}\left|\sum_{i\in\mathrm{bin}} e_i^{\mathrm{y}}\right|\right\rangle, \tag{4.14}$$

where N_{c} is the number of particles at a distance r_c from the pipe axis, $\rho_0=\frac{N_{\mathrm{P}}}{V_{\mathrm{M}}}$ the average number density of the whole system, Δr_{c} the width of the cylindrical bins, and the summation in Eq. (4.14) is taken over all the particles in a given bin. The local density of the shell matches the overall average value when $\rho\left(r_{\mathrm{c}}\right)=1$. The results are shown in Fig. 4.4 for the same values of α shown in Fig. 4.3. From this figure, we can explain the differences seen in Fig. 4.3. In the case of $\alpha=-0.2$ and 0, when the volume fraction is small ($\varphi=0.05$, (a)), particles show a strong tendency to accumulate in the vicinity of the wall and almost no particles are observed within the central region ($r_c\simeq 0$). Such a wall accumulation effect has been reported for active systems in general[51, 117], and several works on squirmers have also shown this behavior[66, 84]. At the same time, we can see that the local polar order is reduced in the vicinity of the wall. In other words, the pipe can be divided into two distinct regions from the view point of p_{y}: an inner region where the local order has a value similar to that of the corresponding bulk dispersion, and an outer region (near to the walls) where the order is reduced. In the following, we specify the characteristic size of this outer region by l_{c}, the distance from the wall to the point where the inner region starts. Because, in these cases, most particles accumulate in this outer region, where the order is reduced, the overall polar order is smaller than that in bulk. Then, as φ is increased, the particles will become more uniformly distributed, and l_{c} is reduced. At the same time, due to the wall accumulation effect, the effective volume fraction in the inner region is smaller than the global volume fraction. Taking into account the fact that the polar order increases with decreasing volume fraction, this reduction in the volume fraction leads to a higher local polar order at the inner region, compared

to the bulk value at the same global volume fraction. As a result of these two effects, namely, the decrease in l_c and the increase of the local order due to the diluteness at the center, at $\varphi = 0.15$, the value of P_y recovers the bulk result. In the case of $\alpha = -0.2$, at $\varphi = 0.24$, the value of P_y is even larger than that in bulk. In the case of $\alpha = 0$, such an overshoot is not observed. This is because for $\alpha = 0$, the volume fraction dependency of the polar order is so small that the order is determined only by the value of l_c. For $\alpha = 1$, the value of l_c becomes very large and we don't see any ordering throughout the pipe, although the system with $\alpha = 1$ does show a nonzero value for polar order parameter P in bulk. In the limit when the diameter of the pipe goes to infinity, we expect the dynamics should converge to that observed in bulk. Therefore, we should see a qualitative transition at a critical diameter. This will be investigated in more detail in Sec. III. C.. We also note that the behavior of ρ for $\alpha = 1$ is very similar to that of $\alpha = 0.5$ at all volume fractions, although the order formation tendencies are completely different. At the highest volume fraction $\varphi = 0.49$, because of the screening of the hydrodynamic interactions, the excluded volume effects become dominant in determining the structure. Consequently, the structure is the same for all values of α. However, it is interesting to note that only in the case of $\alpha = 0.5$, do we observe a nonzero value of P_y.

We have clarified that in many particle systems, the wall effects can be characterized by the accumulation of particles over a distance of l_c close to the walls. These can lead to both enhancement and inhibition of the ordering, depending on the degree of accumulation and the size of l_c. While for some cases we do observe a rectification effect due to the existence of walls, the origin for such effects seems to have nothing to do with the causes responsible for the single particle trajectories presented above.

4.3.3 Pipe size dependency

Here, we show results for the pipe diameter dependence of the dynamics. First, we present the results for the single-particle systems in a pipe with a "small" diameter.

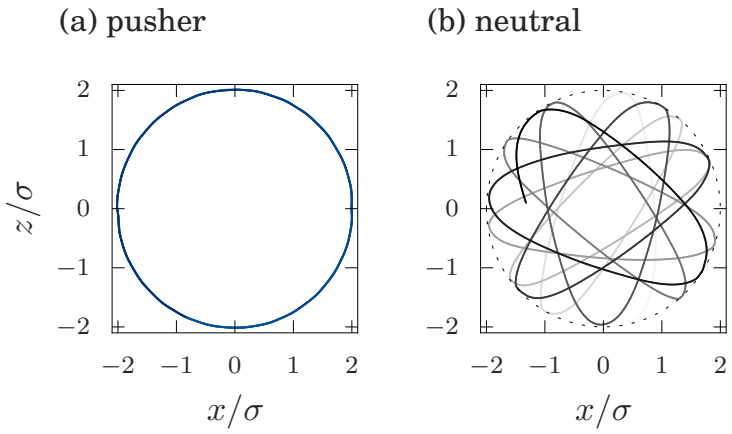

FIGURE 4.5: The projection of the trajectories in a small pipe onto the xz-plane. (a) Pusher with $\alpha = -1$. (b) Neutral swimmer. The lines represent the projections of the trajectories, with color intensity used to represent the time.

Here, we use $D = 2\sigma$, which corresponds to the system in ref.[67]. For these single-particle systems, we have observed the same qualitative results as those for $D = 8\sigma$ (which we refer to as the "big" pipe), except for pushers. First, let us recapitulate the single particle motion in the big pipe. In this case, the three different swimmers (puller, pusher and neutral swimmer) show qualitatively different trajectories. A puller swims parallel to the pipe axis, while a pusher is trapped in a closed orbit at a constant y-value. Finally, a neutral swimmer shows a behavior in between that of a pusher and a puller, namely a spiral motion. In the small pipe, only a pusher shows a different dynamical mode from that observed in the big pipe. In the small pipe, a pusher follows a spiral trajectory, just like a neutral swimmer. Nevertheless, we still see a distinct difference between a pusher and a neutral swimmer, if we look at the projection onto the xz-plane (see Fig. 4.5). The pusher's trajectory shows a perfect circular shape while the neutral swimmer shows a wave-like pattern. The trajectory we have obtained for the neutral swimmer is neither regularly patterned nor closed, unlike the results report in ref[67]. We believe this discrepancy is due to the roughness of the wall surface.

Next, we investigated the polar order of many particle systems in the small pipe. We present the results for a pipe with $D = 3\sigma$ as a reference system for the many

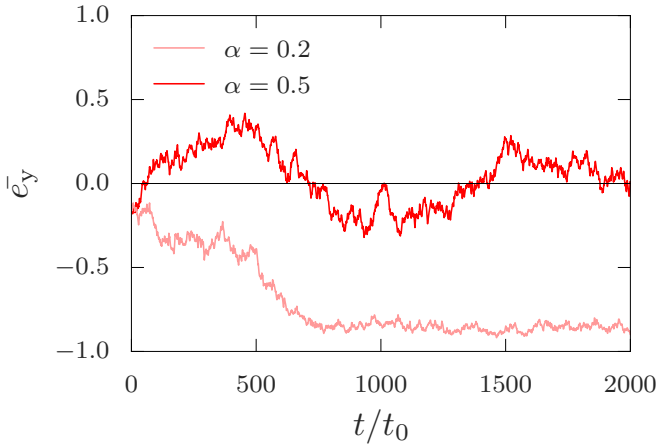

FIGURE 4.6: The time evolution of the temporal order $\bar{e^y}$ for systems with $\alpha = 0.2, 0.5$ in the small pipe with $D = 3\sigma$ at $\varphi = 0.28$. The horizontal axis gives the time normalized by $t_0 = \sigma/U_0$, where $U_0 = \frac{2}{3}B_1$ is the steady state velocity of an isolated swimmer. The vertical axis represents the value of temporal order.

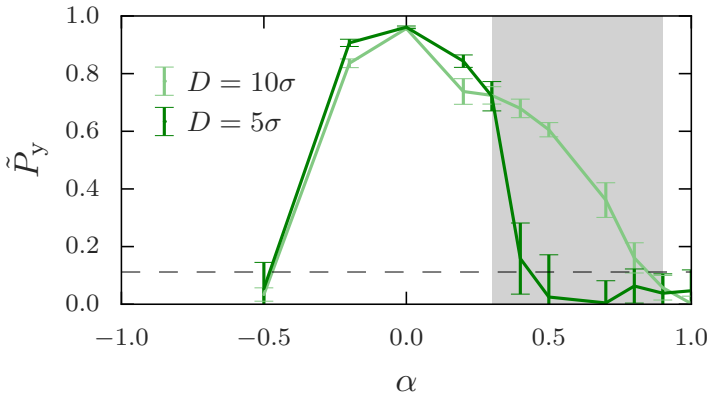

FIGURE 4.7: The dependency on α of the polar order $\tilde{P}_y$ in pipes. The dark lines are for the pipe with $D = 3\sigma$, while the light lines are for $D = 8\sigma$. The volume fraction is $\varphi \approx 0.25$ for both cases. The shaded region represents the region where the anomalous behavior was reported in ref.[84, 116].

particle dynamics, but we have confirmed that the same qualitative results are obtained for $D = 2\sigma$, for both the single- and many-particle dynamics. In the small pipe, over a specific range of parameters, the value of the polar order doesn't show a stable nonzero value. In Fig. 4.6, the time evolution of the temporal order $\bar{e}^{\mathrm{y}}$, defined in Eq. (4.15), is given for two cases to illustrate both the steady and unsteady behaviors.

$$\bar{e}^{\mathrm{y}} = \frac{1}{N_{\mathrm{p}}} \sum_{i}^{N_{\mathrm{p}}} e_i^{\mathrm{y}}. \tag{4.15}$$

Both results are for a system with $D = 3\sigma$ and $\varphi = 0.28$ ($N_{\mathrm{p}} = 80$). The steady results are for $\alpha = 0.2$, the unsteady one for $\alpha = 0.5$. As seen here, in the unsteady system, even the sign of $\bar{e}^{\mathrm{y}}$, which represents the direction of motion, changes in time; while in the systems with stable order, such change is never observed. This change of direction shows the absence of any long-time persistent order in the pipe. In order to evaluate such direction-flipping behavior, we define an alternative in-pipe polar order parameter that can also indicate the persistence of the motion:

$$\tilde{P}_{\mathrm{y}} = \left| \left\langle \frac{1}{N_{\mathrm{p}}} \sum_{i}^{N_{\mathrm{p}}} e_i^{\mathrm{y}} \right\rangle \right|. \tag{4.16}$$

Only the order of taking the average and the absolute value is changed with respect to the standard definition of the polar order P_{y}, Eq. (4.12). For the cases in which the direction doesn't change, the values P_{y} and $\tilde{P}_{\mathrm{y}}$ are essentially the same. We measured $\tilde{P}_{\mathrm{y}}$ in the small pipe for various values of α and compared the results with those obtained for the big pipe. The results are shown in Fig. 4.7 at a volume fraction of $\varphi \approx 0.25$. We observe a remarkable differences over the range $0.4 \leq \alpha \leq 0.7$. In the small pipe for this range of values of α, $\bar{e}^{\mathrm{y}}$ has no steady state value and changes directions, as described above. Actually, for such systems, the values of $\tilde{P}_{\mathrm{y}}$ are around P_0, which means that the system has no order. We consider this collapse of the order as an order/disorder phase transition. The gray-shaded region in Fig. 4.7 indicates the range

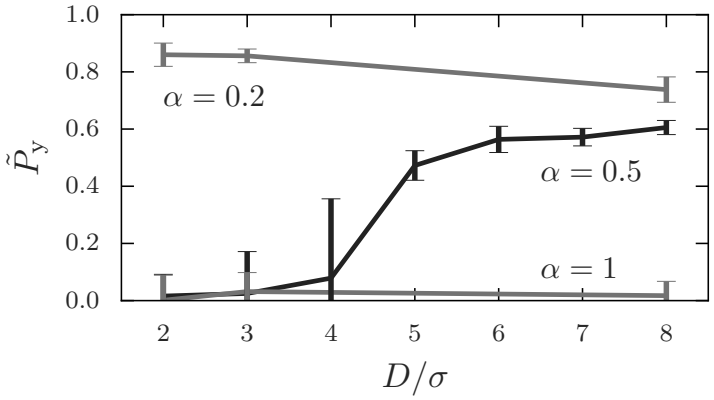

FIGURE 4.8: The pipe diameter dependency of the in-pipe polar order $\tilde{P}_y$. The horizontal axis represents the pipe diameter D normalized by the particle diameter. The volume fraction is $\varphi \approx 0.25$ for all cases.

of α at which anomalous behaviors were reported in preceding studies[84, 116]. In ref.[84], the dynamics of swimmer dispersions between flat parallel walls was studied. It was reported that, over this gray-shaded range of α, particles form big clusters, which exhibit a traveling wave-like motion, bouncing back and forth between walls. Interestingly, the shaded area corresponds very well to the region over which we observe the pipe-size dependent order/disorder transition in the present work. We refer to pullers in these regions as "intermediate" pullers. For α values other than those of intermediate pullers, the results are roughly the same between $D = 8\sigma$ and $D = 3\sigma$. We note that we have confirmed that the same qualitative results are obtained for different values of φ, at least over the range we have considered ($0.05 \leq \varphi \leq 0.25$). We would also like to stress that in bulk, we have observed a similar order/disorder phase transition when we change the volume fraction[83, 116]: when the volume fraction becomes very high, none of the swimmers except intermediate pullers are able to maintain the polar order. In contrast, in pipes, only intermediate pullers lose their polar order when the size of the pipe becomes small.

We have also investigated the detailed size dependency of the polar order for intermediate pullers. In Fig. 4.8, the values of the polar order $\tilde{P}_y$ are shown as a function

of the pipe diameter. Here, the results are shown not only for intermediate pullers $\alpha = 0.5$, but also for weak and strong pullers $\alpha = 0.2, 1$, which don't show the phase transition. The volume fraction is $\varphi \approx 0.25$ for all cases ($40 \leq \varphi \leq 500$, depending on the size of the pipe). We see an abrupt drop of $\tilde{P}_{\mathrm{y}}$ at the critical diameter $D_{\mathrm{c}} = 4\sigma$, though at higher D, the values are constant. In systems with $D \leq 4\sigma$, the value of $\tilde{P}_{\mathrm{y}}$ does not achieve the steady state, similar to the situations seen in Fig. 4.7. In other words, in such small pipes, intermediate pullers cannot maintain the polar order anymore, though temporally they can exhibit order. We believe this sensitivity to the pipe size suggests that intermediate pullers need clusters bigger than a characteristic size D_{c} to stabilize the polar order.

In order to specify the size of the cluster in bulk, we performed bulk simulations and measured the generalized radial distribution functions $g_n\,(r)$[75],

$$g_n\,(r) = \left\langle \frac{1}{4\pi r^2 \Delta r} \frac{1}{\rho_0\,(N_p - 1)} \sum_{i=1}^{N_p} \sum_{j \in \mathrm{bin}} P_n\,(\cos\theta_{ij}) \right\rangle, \tag{4.17}$$

where r represents the distance from a reference particle i to a second particle j, $\theta_{ij} = \cos^{-1}\,(\hat{\boldsymbol{e}}_i \cdot \hat{\boldsymbol{e}}_j)$ the relative angle between the swimming directions of both particles, and P_n is the n-th degree Legendre polynomial. The zeroth-order function $g_0\,(r)$ is the standard radial distribution function, and the first-order function $g_1\,(r)$ represents the local degree of orientational order. In the limit when $r \to \infty$, we expect $g_0\,(r \to \infty) \sim 1$ and $g_1\,(r \to \infty) \sim P^2$. Therefore, we can define the excess local order $\delta P\,(r) = \sqrt{g_1} - P$, in such a way that it will converge to zero in the limit of $r \to \infty$. The bulk system considered here has a cubic domain with a linear dimension of $128\Delta \approx 20\sigma$. Periodic boundary conditions are used in all directions, and the particles have the same diameter and interface thickness as in the simulations discussed above. The volume fraction is tuned by changing the number of particles, $1000 \leq N_{\mathrm{p}} \leq 9000$. The calculated results for $g_0\,(r)$, $g_1\,(r)$ and $\delta P\,(r)$ are shown in

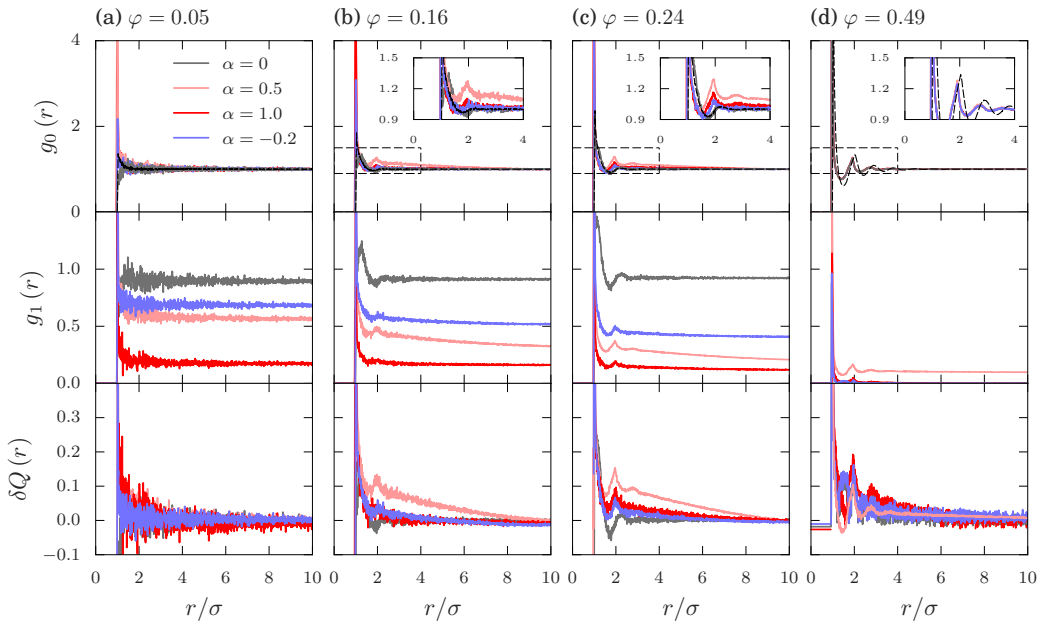

FIGURE 4.9: The generalized radial distribution functions g_0, g_1 and the local deviation of the order δP with respect to bulk values for various combinations of φ and α. Insets show the images magnified in both x and y directions. The horizontal axis represents the distance from the reference particle normalized by the particle diameter.

Fig. 4.9, for $\varphi = 0.05, 0.16, 0.24, 0.49$ and $\alpha = -0.2, 0, 0.5, 1$, corresponding to the confined systems in Fig. 4.4. In addition, results for $g_0(r)$ for passive colloidal systems are shown to aid in comparison. For these passive systems, the temperature is set so that $k_\mathrm{B}T = \epsilon$, where $\epsilon = \frac{\Delta\eta^2}{\rho_\mathrm{f}}$ is the energy unit in our system. The exact value of the temperature does not affect the radial distribution function, provided that it is small enough.

To begin the analysis of the structure, we discuss the behavior of $g_0(r)$ for the reference system of passive colloids. At the smallest volume fraction ($\varphi = 0.05$), it shows only a small first peak around $r = \sigma$, and quickly decays, converging to one around $r = 1.5\sigma$. The intensity of this first peak becomes larger as the volume fraction increases. At a volume fraction of $\varphi = 0.16$, we observe a shallow undershoot after the first peak. The correlation length becomes longer and the value converges to one at around $r = 2\sigma$. At $\varphi = 0.24$, it starts to show a second peak at a position $r \gtrsim 2\sigma$,

though the intensity is very small. Finally, at $\varphi = 0.49$, the system is in a mixed state of ordered and disordered phases[118], and shows four clearly distinguishable peaks (see inset magnified figures in Fig. 4.9(d)).

Now, we would like to present the results for the active systems. In the case of $\alpha = 0$, for all the volume fractions but the highest one, the first peak is smaller or shifted to larger distances compared to the passive system. In addition, the first peak doesn't even appear at the lowest volume fraction, $\varphi = 0.05$. These behaviors may indicates that there is an effective repulsive interaction between particles caused by the flow field. Due to this repelling flow field, neutral swimmers tend to get distributed uniformly. Similar effects can be seen in the pipe, as shown in Fig. 4.4 where neutrals swimmers show a much more uniform distribution compared to the pushers. The correlations beyond the first peak follow closely those of the passive system, while other swimmers show longer ranged correlations. This tendency may reflect the fact that the flow field around a neutral swimmer (decaying as r^{-3}) is more localized, because of the lack of the force dipole term (decaying as r^{-2}; the second term in Eq. 4.1). Regarding $g_1(r)$, the qualitative behavior follows that of $g_0(r)$. We note that the neutral swimmers exhibit a unique behavior around $r = 2\sigma$, where $\delta P(r)$ shows negative values for intermediate values of $\varphi = 0.16, 0.24$.

In the case of $\alpha = -0.2$ and 1, the results are quite similar for all the volume fractions, although the peak heights show slight differences. In these cases, the particles seem to show effective attraction due to the flow field, resulting in higher peaks for $g_0(r)$. As before, $g_1(r)$ follows the qualitative behavior seen in $g_0(r)$. Besides the higher peaks, the correlation length is longer than that seen for neutral swimmers. However, the bulk values are reached by $r \approx 6\sigma$ in all cases.

In the case with $\alpha = 0.5$, or intermediate pullers, many unique behaviors can be observed. First of all, $g_0(r)$ shows much more outstanding peaks than in any of the other cases. At $\varphi = 0.16$, only intermediate pullers show a definite second peak, and at $\varphi = 0.24$, the second peak is much higher than in the other systems, and a third

peak even appears. A similar peak behavior can be observed also in the plot of $\delta P\,(r)$. In addition, we see a very long tail, which is not seen in the other cases. All these unique behaviors for intermediate pullers can be understood as indirect evidence for their already known dynamic clustering tendency[75, 84]. The high peaks reflect the clustering behavior, and the long tail in $g_1\,(r)$ shows the highly localized ordering. The nonzero order at high volume fractions helps explain how intermediate pullers can swim collectively, even under such extreme conditions. We note that the critical diameter of the pipe D_{c} is bigger than any of the peaks detected here.

At the highest volume fraction, $\varphi = 0.49$, the shapes of $g_0\,(r)$ are the same for all α, while only the passive system shows a different shape. Regarding the neutral swimmer systems, $\alpha = 0$, this is notable because this system shows quite similar shapes at all the other volume fractions. The shape difference of $g_0\,(r)$ between the passive and active systems at $\varphi = 0.49$ may be due to the phase transition of the passive system. For passive hard-spheres, the volume fraction in the range $0.5 < \varphi < 0.55$ is known as the transient state of the ordered state and the disordered state[118]. In the passive system at $\varphi = 0.49$, shown in Fig. 4.9, such an ordered state seems to appear, while the active systems are still completely in the fluid phase. At this volume fraction, because the excluded volume effect is the dominant factor to determine the structure, rather than the flow field, all the active systems show the same shape for g_0. In summary, although we could not obtain a direct connection between the bulk structural information and the in-pipe order/disorder phase transition, we believe our results for the structure present indirect evidence for the importance of the dynamic clustering on the stabilization of the polar order for intermediate pullers systems. In order to verify the exact connection between these two quantities, we have to conduct a more detailed analysis on the dynamic clustering in bulk. Our previous results [116] support this view on the importance of dynamic clustering. In ref.[116], we investigated whether or not the polar order seen in bulk can be explained only by the repetition of binary collisions. We found that this is the case, except for systems of intermediate

pullers, which means that many particle interactions might be important in systems of intermediate pullers.

Finally, we have also considered pipes with diameters larger than 8σ. As the pipe size increases, we can expect that the dynamics approaches that seen in bulk systems. Indeed, for systems with $\alpha \neq 1$, we see in Fig. 4.3 that the order parameters in confinement agree very well with the bulk values. Thus, for these values of α, $D = 8\sigma$ seem to be big enough. Therefore, we have only considered larger diameters for $\alpha = 1$, to investigate whether a nonzero value of P is recovered for a large enough pipe diameter. We considered diameters up to $D = 18\sigma$ but were not able to recover the bulk values in this case. Thus, the hypothesis stated in section III. B. is still not solved within the range of parameters considered in the present study. Although it is possible that the dynamics can change for even larger diameters, we will not discuss this problem any more, as it lies outside the scope of the present work.

4.3.4 Confinement shape dependency

The dynamics of fluids in pipes is known to depend on the shape of the cross section. Therefore, we have also investigated the effect of the shape dependency on the dynamics of the swimmers. So far, we have only considered dynamics in cylindrical pipes, with circular cross sections. Here, we consider pipes with a rectangular cross section. We refer to such confinement geometries as "ducts". We considered two sizes of ducts, specified by a lateral size of 3σ and 8σ, respectively. Regarding the single-particle dynamics, the trajectories are qualitatively different from those in pipes for the case of pushers and neutral swimmers. Pullers will swim parallel to the duct axis, as they do in pipes. In ducts, regardless of the size, the trajectories of the pushers are spiral. Of course, reflecting the duct shape, the projections onto the xz-plane are no longer circular (Fig. 4.10). The neutral swimmer shows a similar spiral trajectory, but it has a strong dependency on the initial state and sometimes the trajectories can become more complicated (Fig. 4.10). Considering all the results for the single-particle

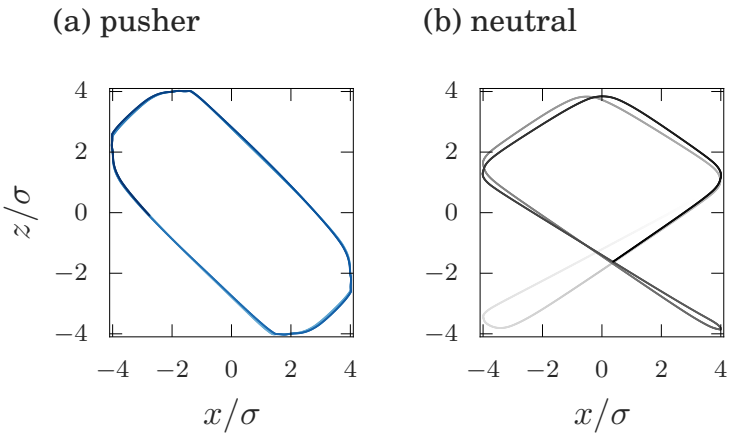

FIGURE 4.10: The projection of the trajectories of a swimmer in duct onto the xz-plane. (a) Pusher with $\alpha = 1$. (b) Neutral swimmer. The lines represent the projections of the trajectories, with color intensity used to represent the time.

system of pushers, we can conclude that the emergence of the circular closed orbits depends strongly on the curvature of the confining walls. Therefore, if we increase the diameter of the pipe continuously from 8σ, at some point we will find a critical value for pushers to lose their orbit-type characteristics. Such a detailed study is beyond our scope.

With regards to the many particle dynamics, we don't see any big differences from those in pipes. Namely, the results are almost the same as those in bulk when the duct size is big enough, and the ordering seen for intermediate pullers collapses when the size is decreased. As a result, intriguingly, from the view point of the polar order of the many particle dispersion, the results are qualitatively the same between pipes and ducts. However, it is possible that we can observe unique dynamics in a skewed confinement.

4.4 Conclusion

We investigated the polar order formation in pipes, conducting three-dimensional direct numerical simulation with fully resolved hydrodynamics. As a result of the investigation over a broad range of parameters, we confirmed that in most cases the

dynamics of many particle systems in pipes match very well those in bulk. We have only observed considerable differences over a small range of parameters. We have presented an explanation for the emergence of wall effects by measuring the structural information. They are mostly due to the wall accumulating effects and the reduction in the degree of order in the vicinity of the walls. Also, we have studied the effects of the change in pipe size. We have clarified that for a specific range of the swimming parameter, the system undergoes an order/disorder phase transition when the size of the pipe shrinks. Considering the results of the structural analysis in bulk, we believe that this is due to the intrinsic clustering tendency of the swimmers. There seems to exist a minimum cluster size which is necessary to maintain the polar order of intermediate pullers. If we change the shape of the confinement, we found no qualitative differences, from the view point of the polar order. These results can be utilized to address the transport problem of microswimmers, however, further studies, like in winding pipes or in pipes with abrupt expansion/contraction are desired for realistic applications.

5 General Conclusion

This dissertation is devoted to the study on collective motion of model microswimmers by means of three dimensional direct numerical simulation with fully resolved hydrodynamics. This dissertation has two main focuses: the collective motion in bulk and how dynamics change under confinement. The first aspect is investigated in **Chapter 2**. In this chapter, first, we measured the degree of order comprehensively as a function of both the swimming parameter and the volume fraction of particles. And then, by composing a simplified binary collision model, it is demonstrated that the collective alignment seen in bulk can be explained only by binary collisions in most cases. The second aspect, the collective motions under confinement, is investigated in **Chapter 3** and **Chapter 4**. Flat parallel walls are considered in**Chapter 3** and cylindrical confinements in **Chapter 4**. In both of these chapters, the behaviors under confinement are compared with those in bulk to understand the difference.

In **Chapter 2**, first, the value of the polar order parameter Q, defined by Eq. (2.8) is measured for various combinations of the swimming parameter α and the volume fraction of particles φ. We found that different values of α lead to different volume fraction dependency, though in the preceding work by Evans *et al.*, such volume fraction dependency was studied only for the system with $\alpha = 1$. We qualitatively reproduced the results of this preceding work for the same system: the values of Q are constant at $\varphi < 0.4$ and then the value drops abruptly to Q_0, which means the system has no order. For most cases, we observed the same tendency. We describe the tendency for each cases as the deviation from the neutral cases, which we would like to treat as the reference system. However, pushers show decrease both in the degree of the order and the value of the critical volume fraction. pullers show decrease only in

the degree of the order

At volume fractions lower than semi-dilute regime (where we don't see any phase transition), we can still say the volume fraction is not a crucial factor for the polar order, in agreement with the previous work. Because we can assume all the particle-particle interactions are binary ones at very low volume fraction regime, we can expect that only binary collisions lead to the bulk polar order at such low volume fractions. Thus, in order to confirm this deduction, we compose a simplified binary collision model (BCM). Firs, we conducted simulations for the system of only two particles with various combinations of incoming angles, and measured the outgoing angles. In the BCM, agents are just point particles which have only the information of the angle. At each step, two particles are chosen randomly. They "collide" and change directions according to the statistics of the binary collision DNS results. After sufficiently large number of steps, all the system achieve the steady state. Doing this BCM analysis for various values of α. The results of BCM match those from bulk DNS semi-quantitatively over vast range of α. However, for a specific range of pullers, the bulk polar order cannot be achieved by the BCM. This range of pullers are known to show dynamic clustering behavior in bulk. Therefore, we consider our results are indirect evidences for the importance of multi-particle interactions for the polar order formation in the systems of those pullers. In the rest of the dissertation, also this range of pullers show anomalous behaviors. So, we named this range intermediate pullers.

In **Chapter 3**, the dynamics between flat parallel walls are investigated. It is already known that microswimmer dispersions can show various nontrivial collective motions even in bulk. The representative example is the polar order formation, which is investigated in **Chapter 2**, and for a specific range of the swimming parameter α, formation of dynamic clusters is also reported. In order to understand such dynamic cluster formation quantitatively, we calculated, for the bulk trajectory data obtained from DNS, the dynamic structure factor, which is the Fourier transformation of density correlation function with respect both to time and space. As a result, we confirmed

that the squirmer dispersions can show pseudo-acoustic property depending on the value of α. Although not all the values of α lead to the pseudo-acoustic property, it is interesting that we observed such a property even for the parameters at which we don't observe dynamic clusters. We cannot expect the similar pseudo-acoustic property for passive colloidal dispersions, because such systems are completely over-dumped. This pseudo-acoustic property can be announced as the anomalous one of active systems.

In this chapter, we also investigated the dynamics of microswimmer dispersions between flat parallel walls. In this system, the control parameters are only three, the swimming parameter, the volume fraction of particles and the separation of the walls. In this work, we fixed the volume fraction at around 13% mainly. As a result, we clarified that three different dynamical modes can be observed depending on the value of the swimming parameter and the separation of the walls: polar order formation in the direction parallel to the walls, random no-order motion and traveling wave-like motion bouncing back and forth between the walls. The third mode is observed at the parameters at which we observe dynamic clusters in bulk. Even taking into account the bulk clustering behavior, such a traveling wave-like motion is an anomalous behavior which cannot be expected intuitively. In this work, we aim at the quantitative understanding of this phenomenon. We suspected that this phenomenon is sharing the same origin with the bulk dynamic clustering, and to compare the two phenomena, we measured the characteristic velocity of the collective behaviors. Such a velocity can be defined easily between the walls because the direction of the collective motion is obvious. In bulk, already we obtained the pseudo-sound velocity by the dynamic structure factor measurement. These values match well quantitatively. We consider that this result imply the traveling wave-like motion seen between walls is the manifestation of the pseudo-sound property. Also, interestingly, the range of α at which we observe the traveling wave-like motion match very well intermediate pullers for which BCM couldn't reproduce the bulk DNS results.

In **Chapter 4**, the dynamics in pipes is investigated. As to the single-particle dynamics, it is already reported that different dynamical modes can be observed depending on the swimming parameter α. In this work, we first performed calculation for single body systems and confirmed the agreement within our calculation methods. Next, the collective dynamics of many body system, pipe size dependency of the dynamics and the confinement shape dependency are studied. We performed simulations of the many body system, fixing the pipe diameter and changing the values of the volume fraction of particles and the swimming parameter. Though obtained values of the polar order parameter match well those in bulk for many cases, we observed several differences. By structural analysis in the pipe, it is elucidated that the cause of these differences can be explained mainly by the wall accumulation.

By studying pipe size dependency of the polar order, we found that pullers with α at a specific range cannot maintain the polar order in pipes smaller than a critical size. This can be understood as an order/disorder phase transition. Again only intermediate pullers show this anomalous phase transition. We consider that this sensitive size dependency implies the importance of the clustering behavior on the polar ordering in the systems of intermediate pullers. Regarding the shape dependency, we don't see any qualitative change with respect to the collective alignment.

Results from the **Chapter 3** and **Chapter 4** suggest that understanding the dynamic clustering in bulk can also help understanding the unique behaviors of intermediate pullers seen under confinements. As the perspectives for the future work, this should be pronounced. At least two approaches can be thought for study on the dynamic cluster. One is to measure the geometrical information of the dynamic clusters, and the other is to investigate the onset of the cluster. Regarding the former one, the failure of the generalized radial distribution function, or the complete information about the static property, to detect the typical size of dynamic cluster indicates that such a detection require a clearer definition for the dynamic cluster which enables us to measure clusters directly. In other words, the methods valid for the static passive system seem

not to be proper way. Regarding the latter part, the author believe that the measurement for the effective interactions between particles can beat a path.

Usually, as the examples of industrial applications of microswimmers, prevention of biofilm formation or the targeted drug delivery systems are mentioned. However, the author expects that the results in this dissertation are rather relevant to the development of brand new materials: liquids with a tunable viscosity. Rafai *et al.* reported that the effective viscosity of microswimmer (chlamydomonas) suspension can be different depending on the activity of the swimmers[90]. By using microswimmers whose activity is externally controllable, we can expect to develop liquid materials with a tunable viscosity. The works in this dissertation can provide an insight into the design of such microswimmers depending on purposes.

A The derivation of the Squirmer Model

In this appendix, we review the derivation of the squirmer model. Though Pak and Lauga discussed in detail already in ref.[119], they omitted the derivation of the Lamb's general solution, or the general solution of the Stokes equation. Here we show the full derivation of the squirmer model from the normal Navier-Stokes equation with constant viscosity and density, though the most important parts follow ref.[119].
The Navier-Stokes equation for incompressible fluids can be simplified as:

$$\begin{cases} \dfrac{\mathrm{D}\boldsymbol{u}}{\mathrm{D}t} = \dfrac{\partial \boldsymbol{u}}{\partial t} + (\boldsymbol{u}\cdot\nabla)\,\boldsymbol{u} = \dfrac{\mu}{\rho}\nabla^2\boldsymbol{u} - \dfrac{1}{\rho}\nabla p, \\ \nabla\cdot\boldsymbol{u} = 0. \end{cases} \tag{A.1}$$

When the Reynolds number, Re, is sufficiently small, the nonlinear inertial term can be ignored. Note that there are at least two ways of nondimesioalizing the pressure term in the Navier-Stokes equation. In order to obtain the following notation, we have to use $p^* = \frac{\mu U}{L}$, where U and L are the specific velocity and length in the system, while nondimensionalizing with $p^{*\prime} = \rho U^2$ is also popular. Then, above equations can be further simplified and we get a linear time-independent equation which is called the Stokes equation:

$$\mu\nabla^2\boldsymbol{u} = \nabla p, \quad \nabla\cdot\boldsymbol{u} = 0. \tag{A.2}$$

A.1 Lamb's general solution

In this section, the general solution for the Stokes equation, which was derived by Lamb[120], will be introduced. Because the Stokes equation is an inhomogeneous linear partial differential equation, Lamb exploited the mathematical theorem that the general solution of an inhomogeneous differential equation is expressed as a linear combination of the general solution of the equivalent homogeneous equation and a particular solution of the inhomogeneous one in hand. Therefore the derivation is performed in two steps.

A.1.1 The solution of the preliminary homogeneous equation

In order to solve Eq. (A.2) analytically, the following preliminary homogeneous equation should be considered first,

$$\begin{cases} \nabla^2 u' = 0, \quad \nabla^2 v' = 0, \quad \nabla^2 w' = 0, & \text{(A.3a)} \\ \nabla \cdot \boldsymbol{u} = \dfrac{\partial u'}{\partial x} + \dfrac{\partial v'}{\partial y} + \dfrac{\partial w'}{\partial z} = 0. & \text{(A.3b)} \end{cases}$$

Expanding u', v', w' in the series of solid harmonics (see Appendix B.2), the terms of nth-order, u'_n, v'_n, w'_n are a solution set of Eq. (A.3b) independently from terms of other orders. Therefore, Eq. (A.3a) can be rewritten:

$$\begin{cases} \dfrac{\partial}{\partial y}\left(\dfrac{\partial v'_n}{\partial x} - \dfrac{\partial u'_n}{\partial y}\right) = \dfrac{\partial}{\partial z}\left(\dfrac{\partial u'_n}{\partial z} - \dfrac{\partial w'_n}{\partial x}\right), & \text{(A.4a)} \\ \dfrac{\partial}{\partial z}\left(\dfrac{\partial w'_n}{\partial y} - \dfrac{\partial v'_n}{\partial z}\right) = \dfrac{\partial}{\partial x}\left(\dfrac{\partial v'_n}{\partial x} - \dfrac{\partial u'_n}{\partial y}\right), & \text{(A.4b)} \\ \dfrac{\partial}{\partial x}\left(\dfrac{\partial u'_n}{\partial z} - \dfrac{\partial w'_n}{\partial x}\right) = \dfrac{\partial}{\partial y}\left(\dfrac{\partial w'_n}{\partial y} - \dfrac{\partial v'_n}{\partial z}\right). & \text{(A.4c)} \end{cases}$$

$$\left(\begin{array}{ll} & \frac{\partial}{\partial x}u'_n + \frac{\partial}{\partial y}v'_n + \frac{\partial}{\partial z}w'_n = 0 \\ & \Rightarrow \frac{\partial^2 u'_n}{\partial x^2} = -\frac{\partial^2 v'_n}{\partial x \partial y} - \frac{\partial^2 w'_n}{\partial x \partial z} \\ \because & \nabla^2 u'_n = \frac{\partial^2}{\partial x^2}u'_n + \frac{\partial^2}{\partial y^2}v'_n + \frac{\partial^2}{\partial z^2}w'_n \\ & = -\frac{\partial^2 v'_n}{\partial x \partial y} - \frac{\partial^2 w'_n}{\partial x \partial z} + \frac{\partial^2}{\partial y^2}u'_n + \frac{\partial^2}{\partial z^2}u'_n \end{array}\right)$$

Introducing function χ_n, the following equations can be lead:

$$\frac{\partial w'_n}{\partial y} - \frac{\partial v'_n}{\partial z} = \frac{\partial \chi_n}{\partial x}, \quad \frac{\partial u'_n}{\partial z} - \frac{\partial w'_n}{\partial x} = \frac{\partial \chi_n}{\partial y}, \quad \frac{\partial v'_n}{\partial x} - \frac{\partial u'_n}{\partial y} = \frac{\partial \chi_n}{\partial z}, \tag{A.5}$$

$$\left(\begin{array}{ll} & \frac{\partial}{\partial y}A = \frac{\partial}{\partial z}B, \quad \frac{\partial}{\partial z}C = \frac{\partial}{\partial x}A, \quad \frac{\partial}{\partial x}B = \frac{\partial}{\partial y}C \\ \because & \Rightarrow A = \frac{\partial}{\partial z}\chi_n, \quad B = \frac{\partial}{\partial x}\chi_n, \quad C = \frac{\partial}{\partial y}\chi_n \end{array}\right)$$

where, due to the linearity of the Laplace equation, harmonic functions are also linear, so χ_n is also a nth-order solid harmonic. Besides, from Eq. (A.5),

$$z\frac{\partial \chi_n}{\partial y} - y\frac{\partial \chi_n}{\partial z} = x\frac{\partial u'_n}{\partial x} + y\frac{\partial u'_n}{\partial y} + z\frac{\partial u'_n}{\partial z} + u'_n - \frac{\partial}{\partial x}\left(xu'_n + yv'_n + zw'_n\right) \tag{A.6}$$

Considering Eqs. (A.3), the inside of the parenthesis in the last term in Eq. (A.6) should obey:

$$\begin{aligned} \nabla^2\left(xu'_n + yv'_n + zw'_n\right) &= 0, \\ \therefore xu'_n + yv'_n + zw'_n &= \Phi_{n+1}, \end{aligned} \tag{A.7}$$

where, Φ_{n+1} is a solid harmonic function. Now, Eq. (A.6) can be rewritten as:

$$(n+1)\,u'_n = \frac{\partial \Phi_{n+1}}{\partial x} + z\frac{\partial \chi_n}{\partial y} - y\frac{\partial \chi_n}{\partial z}. \tag{A.8}$$

$$\left(\begin{array}{c} x\frac{\partial u'_n}{\partial x}+y\frac{\partial u'_n}{\partial y}+z\frac{\partial u'_n}{\partial z}+u'_n=\frac{\partial \Phi_{n+1}}{\partial x}+z\frac{\partial \chi_n}{\partial y}-y\frac{\partial \chi_n}{\partial z} \\ \because \quad \text{here, } u'_n \text{ is a } n\text{th order polynomial of } x,\, y,\, z, \text{ so} \\ x\frac{\partial u'_n}{\partial x}+y\frac{\partial u'_n}{\partial y}+z\frac{\partial u'_n}{\partial z}=nu'_n \end{array}\right)$$

Generality of this equation will hold even if the both hands sides are divided by $(n+1)$, and we get the homogeneous solution $\boldsymbol{u}_H = (u', v', w')^T$:

$$\begin{cases} u' = \sum\left(\frac{\partial \Phi_n}{\partial x}+z\frac{\partial \chi_n}{\partial y}-y\frac{\partial \chi_n}{\partial z}\right) & \text{(A.9a)} \\ v' = \sum\left(\frac{\partial \Phi_n}{\partial y}+x\frac{\partial \chi_n}{\partial z}-z\frac{\partial \chi_n}{\partial x}\right) & \text{(A.9b)} \\ w' = \sum\left(\frac{\partial \Phi_n}{\partial z}+y\frac{\partial \chi_n}{\partial x}-x\frac{\partial \chi_n}{\partial y}\right) & \text{(A.9c)} \end{cases}$$

$$\therefore \boldsymbol{u}_H = \nabla\Phi + \nabla\times(\boldsymbol{r}\chi) \tag{A.10}$$

(note that the difference in the orders of solid harmonic functions in Eq. (A.8) is implicitly expressed via summation over n in Eqs. (A.9))

A.1.2 Introducing the pressure term

Now let's introduce the pressure term.

$$\begin{cases} \mu\nabla^2 u = \frac{\partial p}{\partial x}, \quad \mu\nabla^2 v = \frac{\partial p}{\partial y}, \quad \mu\nabla^2 w = \frac{\partial p}{\partial z}, & \text{(A.11a)} \\ \frac{\partial u}{\partial x}+\frac{\partial v}{\partial y}+\frac{\partial w}{\partial z}=0 & \text{(A.11b)} \end{cases}$$

Taking derivative, we get:

$$\nabla^2 p = 0 \tag{A.12}$$

$$\left(\begin{array}{c} \\ \therefore \\ \\ \end{array} \begin{array}{c} \text{taking derivative of Eq. (A.11a) and substituting Eq. (A.11b), we get} \\ \\ \nabla^2 p = \mu \nabla^2 \left(\frac{\partial u}{\partial x} + \frac{\partial u}{\partial y} + \frac{\partial u}{\partial z} \right) = 0 \end{array} \right)$$

The pressure can be expanded into a series of harmonic functions in the same manner as the previous subsection:

$$p = \sum p_n. \tag{A.13}$$

In order to solve for the terms of p_n, we assume the following relations:

$$\begin{cases} u = Ar^2 \dfrac{\partial p_n}{\partial x} + Br^{2n+3} \dfrac{\partial}{\partial x} \dfrac{p_n}{r^{2n+1}}, & \text{(A.14a)} \\ v = Ar^2 \dfrac{\partial p_n}{\partial y} + Br^{2n+3} \dfrac{\partial}{\partial y} \dfrac{p_n}{r^{2n+1}}, & \text{(A.14b)} \\ w = Ar^2 \dfrac{\partial p_n}{\partial z} + Br^{2n+3} \dfrac{\partial}{\partial z} \dfrac{p_n}{r^{2n+1}}, & \text{(A.14c)} \end{cases}$$

where, $r = \sqrt{x^2 + y^2 + z^2}$. The terms with B are $(n+1)$th order solid harmonic functions, as presented later. This assumption is the key factor of this derivation, since we just want to know a particular solution. Here, due to the following equation, Eq. (A.15),

$$\begin{aligned} \nabla^2 \left(r^2 \frac{\partial p_n}{\partial x} \right) &= r^2 \nabla^2 \frac{\partial p_n}{\partial x} + 4 \left(x \frac{\partial}{\partial x} + y \frac{\partial}{\partial y} + z \frac{\partial}{\partial z} \right) \frac{\partial p_n}{\partial x} + \frac{\partial p_n}{\partial x} \nabla^2 r^2 \\ &= 2 \left(2n + 1 \right) \frac{\partial p_n}{\partial x} \end{aligned} \tag{A.15}$$

$$\left(\begin{array}{c} \\ \therefore \\ \\ \end{array}\right.\begin{aligned} r^2\nabla^2\frac{\partial p_n}{\partial x} &= r^2\frac{\partial}{\partial x}\nabla^2 p_n = 0 \\ \left(x\frac{\partial}{\partial x}+y\frac{\partial}{\partial y}+z\frac{\partial}{\partial z}\right)\frac{\partial p_n}{\partial x} &= \left\{\frac{\partial}{\partial x}\left(x\frac{\partial}{\partial x}+y\frac{\partial}{\partial y}+z\frac{\partial}{\partial z}\right)p_n\right\}-\frac{\partial p_n}{\partial x} \\ \frac{\partial p_n}{\partial x}\nabla^2 r^2 &= \frac{\partial p_n}{\partial x}\left\{\left(\frac{\partial^2}{\partial x^2}+\frac{\partial^2}{\partial y^2}+\frac{\partial^2}{\partial z^2}\right)\left(x^2+y^2+z^2\right)\right\} \\ &= 6\frac{\partial p_n}{\partial x} \end{aligned}\left.\begin{array}{c} \\ \\ \\ \\ \end{array}\right)$$

Eq. (A.11a) is met with respect to the following A,

$$A = \frac{1}{2\left(2n+1\right)\mu}, \tag{A.16}$$

using this notation of A, Eq. (A.11b) can be rewritten as:

$$2nA - \left(n+1\right)\left(2n+3\right)B = 0. \tag{A.17}$$

$$\therefore B = \frac{n}{\left(n+1\right)\left(2n+1\right)\left(2n+3\right)\mu}. \tag{A.18}$$

Now we get the particular solution:

$$\begin{cases} u = \dfrac{1}{\mu}\sum\left\{\dfrac{r^2}{2\left(2n+1\right)}\dfrac{\partial p_n}{\partial x}+\dfrac{nr^{2n+3}}{\left(n+1\right)\left(2n+1\right)\left(2n+3\right)}\dfrac{\partial}{\partial x}\dfrac{p_n}{r^{2n+1}}\right\}, & \text{(A.19a)} \\ v = \dfrac{1}{\mu}\sum\left\{\dfrac{r^2}{2\left(2n+1\right)}\dfrac{\partial p_n}{\partial y}+\dfrac{nr^{2n+3}}{\left(n+1\right)\left(2n+1\right)\left(2n+3\right)}\dfrac{\partial}{\partial y}\dfrac{p_n}{r^{2n+1}}\right\}, & \text{(A.19b)} \\ w = \dfrac{1}{\mu}\sum\left\{\dfrac{r^2}{2\left(2n+1\right)}\dfrac{\partial p_n}{\partial z}+\dfrac{nr^{2n+3}}{\left(n+1\right)\left(2n+1\right)\left(2n+3\right)}\dfrac{\partial}{\partial z}\dfrac{p_n}{r^{2n+1}}\right\}, & \text{(A.19c)} \end{cases}$$

The general solution $\boldsymbol{u}$ of the objective systems can be expressed as the sum of a particular solution $\boldsymbol{u}_P = (u, v, w)^T$ and the homogeneous solution $\boldsymbol{u}_H$:

$$\begin{aligned}\boldsymbol{u} &= \boldsymbol{u}_P + \boldsymbol{u}_H \\ &= \sum_{n=-\infty}^{\infty} \left\{ \frac{(n+3)\, r^2 \nabla p_n}{2\mu\,(n+1)\,(2n+3)} - \frac{n\boldsymbol{r} p_n}{\mu\,(n+1)\,(2n+3)} + \nabla\Phi_n + \nabla \times (\boldsymbol{r}\chi_n) \right\}\end{aligned} \tag{A.20}$$

A.2 Solving for a squirming swimmer

Now we consider the flow field at the surface of a squirmer of radius a. As squirmers, we basically treat micro self-propelled particles, such as microorganisms or Janus particles, and the as host solvent, viscous liquid like water. Therefore, Re of the squirmers is very low, and the governing equations are the Stokes equation and incompressible type of the equation of continuity. Because we will go into the case of axisymmetric cases later, now we adopt the spherical coordinate foe ease. In this coordinate, the flow field is considered as:

$$\boldsymbol{u} = u_r \boldsymbol{e}_r + u_\theta \boldsymbol{e}_\theta + u_\phi \boldsymbol{e}_\phi. \tag{A.21}$$

For the works in this thesis, flow in the radial and azimuthal direction is ignored and purely tangential squirming motion is treated, which means $u_r(r = a, \theta, \phi) = 0$. As lead as Eq. (A.20) in the subsection A.1.2, the Lamb's general solution is, again, :

$$\boldsymbol{u} = \sum_{n=-\infty}^{\infty} \left\{ \frac{(n+3)\, r^2 \nabla p_n}{2\mu\,(n+1)\,(2n+3)} - \frac{n\boldsymbol{r} p_n}{\mu\,(n+1)\,(2n+3)} + \nabla\Phi_n + \nabla \times (\boldsymbol{r}\chi_n) \right\} \tag{A.22}$$

,where Φ and χ meet $\nabla^2\Phi = 0$, $\nabla^2\chi = 0$. They also can be expressed as series of solid harmonic functions:

$$\Phi = \sum_{n=-\infty}^{\infty} \Phi_n, \qquad \chi = \sum_{n=-\infty}^{\infty} \chi_n \tag{A.23}$$

Now we are on the spherical coordinate, so using the relation between solid harmonics and spherical harmonics presented in Appendix B, nth order solid harmonics Φ_n and χ_n can be expressed like:

$$\begin{cases} \Phi_n = r^n \sum_{m=0}^{n} P_n^m(\psi)\left(b_{mn}\cos m\phi + \tilde{b}_{mn}\sin m\phi\right), & \text{(A.24a)} \\ \chi_n = r^n \sum_{m=0}^{n} P_n^m(\psi)\left(c_{mn}\cos m\phi + \tilde{c}_{mn}\sin m\phi\right), & \text{(A.24b)} \end{cases}$$

where, $\psi = \cos\theta$, $P_n^m(\psi)$ is the associated Legendre polynomials of order m and degree n, defined as solutions of the linear differential equation for $f(\psi)$ Similar expression can be employed for the solid harmonics of the pressure,

$$p_n = r^n \sum_{m=0}^{n} P_n^m(\psi)\left(a_{mn}\cos m\phi + \tilde{a}_{mn}\sin m\phi\right). \tag{A.25}$$

Now, since we are considering the situation in which a squirmer is swimming in a host viscous fluid, the flow field at infinite distance should decay to zero. Therefore, we should discard the terms with $n > 0$ in Eq. (A.20). Also, substituting $-n-1$ into n in Eq. (A.20) (see Appendix B),

$$\boldsymbol{u}(r,\theta,\phi) = \sum_{n=1}^{\infty}\left\{-\frac{(n-2)\,r^2\nabla p_{-n-1}}{2\mu n(2n-1)} + \frac{(n+1)\,\boldsymbol{r}p_{-n-1}}{\mu n(2n-1)} + \nabla\Phi_{-n-1} + \nabla\times(\boldsymbol{r}\chi_{-n-1})\right\} \tag{A.26}$$

$$\begin{cases} p_{-n-1} = r^{-n-1}\sum_{m=0}^{n} P_n^m\left(A_{mn}\cos m\phi + \tilde{A}_{mn}\sin m\phi\right), & \text{(A.27a)} \\ \Phi_{-n-1} = r^{-n-1}\sum_{m=0}^{n} P_n^m\left(B_{mn}\cos m\phi + \tilde{B}_{mn}\sin m\phi\right), & \text{(A.27b)} \\ \chi_{-n-1} = r^{-n-1}\sum_{m=0}^{n} P_n^m\left(C_{mn}\cos m\phi + \tilde{C}_{mn}\sin m\phi\right), & \text{(A.27c)} \end{cases}$$

the pressure field can be calculated by $p = \sum_{n=1}^{\infty}$. Here, $n = 0$ terms are eliminated

because such terms mean sources or sinks and inappropriate for the current rigid particle problem. From Eq. (A.26) and Eqs. (A.27), the solution at spherical coordinate is :

$$u_r = \sum_{n=1}^{\infty}\sum_{m=0}^{n} \frac{(n+1)\,p_n^m}{2\,(2n-1)\,\mu r^{n+2}} \left\{ \left[A_{mn} r^2 - 2B_{mn}\,(2n-1)\,\mu\right] \cos m\phi \right. \\ \left. + \left[\tilde{A}_{mn} r^2 - 2\tilde{B}_{mn}\,(2n-1)\,\mu\right] \sin m\phi \right\} \quad \text{(A.28)}$$

$$u_\theta = \sum_{n=1}^{\infty}\sum_{m=0}^{n} \frac{1}{2r^n \sin\theta} \left\{ \sin^2\theta P_n^{m'} \left[\frac{n-2}{n\,(2n-1)\,\mu} \left(A_{mn}\cos m\phi + \tilde{A}_{mn}\sin m\phi\right) \right.\right. \\ \left. - \frac{2}{r^2}\left(B_{mn}\cos m\phi + \tilde{B}_{mn}\sin m\phi\right)\right] \\ \left. + \frac{2m}{r} P_n^m \left(\tilde{C}_{mn}\cos m\phi - C_{mn}\sin m\phi\right)\right\} \quad \text{(A.29)}$$

$$u_\phi = \sum_{n=1}^{\infty}\sum_{m=0}^{n} \frac{1}{2r^n \sin\theta} \left\{ m P_n^{m'} \left[\frac{n-2}{n\,(2n-1)\,\mu} P_n^m \left(-\tilde{A}_{mn}\cos m\phi + A_{mn}\sin m\phi\right) \right.\right. \\ \left. - \frac{2}{r^2}\left(-\tilde{B}_{mn}\cos m\phi + B_{mn}\sin m\phi\right)\right] \\ \left. + \frac{2}{r}\sin^2\theta P_n^{m'} \left(C_{mn}\cos m\phi - \tilde{C}_{mn}\sin m\phi\right)\right\} \quad \text{(A.30)}$$

Here, for ease, a recursion expression of associated Legendre polynomials was employed, (the prime means derivative with respect to the variable $\psi = \cos\theta$)

$$(n+1)\,\psi P_n^m - (1+n-m)\,P_{n+1}^m = \left(1-\psi^2\right) P_n^{m'} \quad \text{(A.31)}$$

The equation for the radial component, Eq. (A.33), gives the condition for the purely tangential motion:

$$A_{mn} = \frac{2\,(2n-1)\,\mu}{a^2} B_{mn}, \quad \tilde{A}_{mn} = \frac{2\,(2n-1)\,\mu}{a^2}\tilde{B}_{mn}. \quad \text{(A.32)}$$

Therefore, the general solution for tangential motion can be written as:

$$u_r = \sum_{n=1}^{\infty}\sum_{m=0}^{n} \frac{(n+1)\,p_n^m}{r^{n+2}}\left(\frac{r^2}{a^2}-1\right)\left[B_{mn}\mathrm{cos}m\phi + \tilde{B}_{mn}\mathrm{sin}m\phi\right] \tag{A.33}$$

$$u_\theta = \sum_{n=1}^{\infty}\sum_{m=0}^{n}\left[\mathrm{sin}\theta P_n^{m'}\left(\frac{n-2}{na^2r^n}-\frac{1}{r^{n+2}}\right)\left(B_{mn}\mathrm{cos}m\phi + \tilde{B}_{mn}\mathrm{sin}m\phi\right)\right.$$
$$\left. + \frac{mP_n^m}{r^{n+1}\mathrm{sin}\theta}\left(\tilde{C}_{mn}\mathrm{cos}m\phi - C_{mn}\mathrm{sin}m\phi\right)\right] \tag{A.34}$$

$$u_\phi = \sum_{n=1}^{\infty}\sum_{m=0}^{n}\left[\frac{\mathrm{sin}\theta P_n^{m'}}{r^{n+1}}\left(C_{mn}\mathrm{cos}m\phi + \tilde{C}_{mn}\mathrm{sin}m\phi\right)\right.$$
$$\left. - \frac{mP_n^m}{\mathrm{sin}\theta}\left(\frac{n-2}{na^2r^n}-\frac{1}{r^{n+2}}\right)\left(\tilde{B}_{mn}\mathrm{cos}m\phi - B_{mn}\mathrm{sin}m\phi\right)\right] \tag{A.35}$$

A.3 Axisymmetric squirming motion

If we consider the axisymmetric condition of the system, the general solution can be reduced drastically exploiting the axisymmetric condition, $m = 0$,

$$\boldsymbol{u}\,(r,\theta,\phi) = \sum_{n=1}^{\infty}\frac{(n+1)\,P_n}{r^{n+2}}\left(\frac{r^2}{a^2}-1\right)B_{0n}\boldsymbol{e}_r$$
$$+\sum_{n=1}^{\infty}\mathrm{sin}\theta P_n'\left(\frac{n-2}{na^2r^n}-\frac{1}{r^{n+2}}\right)B_{0n}\boldsymbol{e}_\theta + \sum_{n+1}^{\infty}\frac{\mathrm{sin}\theta P_n'}{r^{n+1}}C_{0n}\boldsymbol{e}_\phi, \tag{A.36}$$

where, $P_n = P_n^0$ stands for the Legendre polynomials of degree n.

Imposing $r = a$ in Eq. (A.36), we get the surface velocities on the sphere of radius a:

$$\boldsymbol{u}\,(a,\theta,\phi) = \sum_{n=1}^{\infty} -\frac{2\mathrm{sin}\theta P_n'}{a^{n+2}n}B_{0n}\boldsymbol{e}_\theta + \sum_{n=1}^{\infty}\frac{\mathrm{sin}\theta P_n'}{a^{n+1}}C_{0n}\boldsymbol{e}_\phi \tag{A.37}$$

Discarding terms with $\boldsymbol{e}_\phi$ (or in other words, with the condition $C_{0n} = 0$) and setting

$$B_{0n} = -\frac{a^{n+2}}{n+1}B_n \tag{A.38}$$

we can reproduce Eq. (1.1) in the main text.

B Harmonic Functions

Harmonic function is a general phrase for functions which meet the Laplace equation and are twice differentiable continuously. In this chapter, we recapitulate two harmonic functions: the spherical harmonics and the solid harmonics.

B.1 Spherical Harmonics

The angular portion of Laplacian in spherical polar coordinate can be a differential operator itself:

$$\mathbf{\Lambda} = \frac{1}{\sin\theta}\frac{\partial}{\partial\theta}\left(\sin\theta\frac{\partial}{\partial\theta}\right) + \frac{1}{\sin^2\theta}\frac{\partial^2}{\partial\phi^2}. \tag{B.1}$$

Solutions, $Y(\theta,\phi)$, of differential equations which contain $\mathbf{\Lambda}$, like the angular portion of the Laplace equation on the spherical polar coordinate:

$$\mathbf{\Lambda}Y(\theta,\phi) + \nu(\nu+1)Y(\theta,\phi) = 0 \quad ; \quad \nu = 0,1,2 \tag{B.2}$$

are called the spherical harmonics.

If we assume the relation $Y(\theta,\phi) = P(\theta)Q(\phi)$, and substituting this into Eq.(B.2), we obtain,

$$\frac{\sin\theta}{P(\theta)}\frac{\partial}{\partial\theta} + \nu(\nu+1)\sin^2\theta = -\frac{1}{Q(\phi)}\frac{\partial^2 Q(\phi)}{\partial\phi^2}. \tag{B.3}$$

If the separation constant can be expressed as m^2 using an arbitrary integer, m, Eq. (B.3) can be rewritten as (actually, this assumption doesn't any generality, since the resultant solutions will merely affected by corresponding factor):

$$\frac{\partial^2 Q(\phi)}{\partial \phi^2} = -m^2 Q(\phi) \tag{B.4}$$

$$\frac{\sin\theta}{P\theta}\frac{\partial}{\partial\theta}\left(\sin\theta\frac{\partial P\theta}{\partial\theta}\right) + \nu(\nu+1)\sin^2\theta = m^2 \tag{B.5}$$

Eq. (B.4) can be easily solved as:

$$Q(\phi) = q_m(\phi) = c\exp(im\phi). \tag{B.6}$$

Introducing transformation $x = \cos\theta$ and $\sin\theta = (1-x^2)^{1/2}$, Eq. (B.5) can be expressed as:

$$\left(1-x^2\right)P''(x) - 2xP'(x) + \left(\nu(\nu+1) - \frac{m^2}{1-x^2}\right)P(x) = 0. \tag{B.7}$$

Eq. (B.7) is known as the associated Legendre differential equation. The solutions for this equation are the associated Legendre polynomials P_l^m. Therefore, now we have the complete notation for the total spherical harmonics Y_l^m:

$$Y_l^m(\theta,\phi) = \sqrt{\frac{2\nu+1}{4\pi}\frac{(\nu-m)!}{(\nu+m)!}}P_l^m(\cos\theta)\exp(im\phi), \tag{B.8}$$

where, $l = 0, 1, 2, \ldots$ and $m = -l, -(l-1), \ldots, 0, \ldots, \nu-1, \nu$. The coefficients are decided according to the normalization condition.

B.1.1 Associated Legendre polynomials

$$\left(1-x^2\right)y'' - 2xy' + \left(\nu(\nu+1) - \frac{m^2}{1-x^2}\right)y = 0, \quad \nu = 0, 1, 2, \ldots \tag{B.9}$$

The general solution of this associated Legendre differential equation is the associated Legendre polynomial:

$$y=\begin{cases} P_l^m(x)=\left(1-x^2\right)^{m/2}\dfrac{d^m}{dx^m}P_l(x)=\dfrac{\left(1-x^2\right)^{m/2}}{2^l l!}\dfrac{d^{l+m}}{dx^{l+m}}\left(x^2-1\right)^l, & (m>0) \\ P_l^0(x)=P_l(x), & (m=0) \\ P_l^m(x)=(-1)^{|m|}\dfrac{(l-|m|)!}{(l+|m|)!}P_l^{|m|}(x)=\dfrac{\left(1-x^2\right)^{-|m|/2}}{2^l l!}\dfrac{d^{l-|m|}}{dx^{l-|m|}}\left(x^2-1\right)^l, & (m<0) \end{cases} \tag{B.10}$$

where, $P_l(x)$ is the Legendre polynomial and the following relations hold:

$$P_l(x)=\frac{1}{2^l l!}\frac{d^l}{dx^l}\left(x^2-1\right)^l \tag{B.11}$$

$$P_l^m(x)=\frac{d^m}{dx^m}P_l(x)=\frac{1}{2^l l!}\frac{d^{l+m}}{dx^{l+m}}\left(x^2-1\right)^l \tag{B.12}$$

$$m=-l,-(l-1),\ldots,0,\ldots,l-1,l \tag{B.13}$$

B.2 Solid Harmonics

If we consider the full Laplace equation on the spherical polar coordinate, we can write down the equation using the nondimensional angular momentum operator $\tilde{\boldsymbol{l}}=-i(\boldsymbol{r}\times\boldsymbol{\nabla})$,

$$\boldsymbol{\nabla}^2\boldsymbol{T}(\boldsymbol{r})=\left(\frac{1}{r}\frac{\partial^2}{\partial r^2}r-\frac{\tilde{\boldsymbol{l}}^2}{r^2}\right)\boldsymbol{T}(\boldsymbol{r})=0,\quad \boldsymbol{r}\neq=0 \tag{B.14}$$

And we obtain two distinctly featured particular solutions of the total Laplace equation, one group decay to zero at the origin and called regular solid harmonics:

$$\mathrm{R}_l^m(\boldsymbol{r})=\sqrt{\frac{4\pi}{2l+1}}r^l\mathrm{Y}_l^m(\theta,\phi), \tag{B.15}$$

and the others are singular at the origin and called irregular solid harmonics:

$$\mathrm{I}_l^m(\boldsymbol{r}) = \sqrt{\frac{4\pi}{2l+1}} \frac{\mathrm{Y}_l^m(\theta,\phi)}{r^{l+1}}, \tag{B.16}$$

where Y_l^m is the spherical harmonics introduced in the previous section.

In the Cartesian coordinate, the solid harmonics can be rewritten as following:

$$\mathrm{R}_l^m(\boldsymbol{r}) = \sqrt{\frac{2l+1}{4\pi}(l+m)!(l-m)!} \sum_{p,q,s} \frac{1}{p!q!s!} \left(-\frac{x+iy}{2}\right)^p \left(\frac{x-iy}{2}\right)^q z^s, \tag{B.17}$$

where, p, q, s are natural numbers which meet $p+q+s=l$ and $p-q=m$. After small algebra, we will see solid harmonics are polynomials in the Cartesian.

C Implementation of the SPM with the Squirmer model

In this appendix, the implementation of the SPM is summarized. To solve for the dynamics of a multi-phase flow, we have to track the boundary between the phases. If we do this explicitly, we have to recalculate the calculation mesh at each step, resulting in a very expensive calculation cost. In the SPM, such a boundary between domains is not considered explicitly. Instead, a diffuse interface of finite width ξ is introduced, and the solid domain is represented via an order parameter ϕ_{p}, which takes a value of 1 in the solid domain, and 0 in the fluid domain.

$$\phi_{\mathrm{p}}\left(\boldsymbol{r},t\right)=\sum_{i}\phi_{\mathrm{p}i}\left(\boldsymbol{r},t\right). \tag{C.1}$$

The order parameter field is described by the superposition of the order parameters for each particle. Using this continuous order parameter, the particle velocity can be expressed as a field variable on Cartesian grids:

$$\phi_{\mathrm{p}}\boldsymbol{u}_{\mathrm{p}}\left(\boldsymbol{r},t\right)=\sum_{i}\phi_{\mathrm{p}i}\left(\boldsymbol{r},t\right)\left[\boldsymbol{V}_{i}\left(t\right)+\boldsymbol{\Omega}_{i}\left(t\right)\times\boldsymbol{R}_{i}\left(t\right)\right]. \tag{C.2}$$

where $\boldsymbol{r}_i = \boldsymbol{x} - \boldsymbol{R}_i$. This notation allows us to define the total velocity field which include both the fluid and the particle velocity field throughout the whole computational domain:

$$\boldsymbol{u}\left(\boldsymbol{r},t\right)=(1-\phi_{\mathrm{p}})\boldsymbol{u}_{\mathrm{f}}+\phi_{\mathrm{p}}\boldsymbol{u}_{\mathrm{p}}, \tag{C.3}$$

where $\boldsymbol{u}$ is the total velocity field, $(1-\phi_{\mathrm{p}})\boldsymbol{u}_{\mathrm{f}}$ and $\phi_{\mathrm{p}}\boldsymbol{u}_{\mathrm{p}}$ the velocity field of fluid and particles, respectively. Consequently, we can build a momentum balance equation for a multi-phase system. The equation has the form of a modified incompressible Navier-Stokes equation:

$$\rho_{\mathrm{f}}\left(\partial_t + \boldsymbol{u}\cdot\nabla\right)\boldsymbol{u} = \nabla\cdot\boldsymbol{\sigma}_{\mathrm{f}} + \rho_{\mathrm{f}}\left(\phi_{\mathrm{p}}\boldsymbol{f}_{\mathrm{p}} + \boldsymbol{f}_{\mathrm{sq}}\right), \tag{C.4}$$

$$\boldsymbol{\nabla}\cdot\boldsymbol{u} = 0. \tag{C.5}$$

Note that the imcompressible condition should be considered for the total velocity field. The rigidity condition of particles is took into account via a body force $\phi_{\mathrm{p}}\boldsymbol{f}_{\mathrm{p}}$ and the force distribution due to the squirming motion $\boldsymbol{f}_{\mathrm{sq}}$.

C.1 Fractional steps to update the volecity field

In our calculation scheme, a fractional step approach is employed to update the total velocity field. We introduce temporal values of the total velocity field, $\boldsymbol{u}^*$ and $\boldsymbol{u}^{**}$ for each step respectively:

- The advection term and the viscous stress are calculated and $\boldsymbol{u}^*$ is solved for. Regarding the particles motion, they are moved (rotated) according to the velocities (angular velocities) at this point ($t = t_n$)
- The active flow profile $\boldsymbol{u}^{\mathrm{s}}$ is imposed on the surface of the particles and $\boldsymbol{u}^{**}$ is determined iteratively. Using the resultant value, the hydrodynamic force and torque exerted on particles are calculated. Then particle velocities are also updated.
- The rigidity constraint for particles is considered and $\boldsymbol{u}^{n+1}$ is obtained fully.

In the following, the superscript n means the variables at time $t_n = nh$ (h is the time interval) and how to solve for the total velocity field at time t_{n+1} from the data at t_n is presented.

C.1.1 The first step

First of all, the advection term and the viscous stress in Eq. (C.4) are calculated and the total velocity field is updated to the temporal value for the new step$\boldsymbol{u}^*$. At the same time, particles move and rotate according to the velocities and the angular velocities at the previous step ($t = t_n$):

$$\boldsymbol{u}^* = \boldsymbol{u}^n + \int_{t_n}^{t_n+h} \mathrm{ds} \boldsymbol{\nabla} \cdot \left[\frac{1}{\rho} \left(-p^* \boldsymbol{I} + \boldsymbol{\sigma}'_{\mathrm{f}} \right) - \boldsymbol{u}\boldsymbol{u} \right], \tag{C.6}$$

$$\boldsymbol{R}_i^{n+1} = \boldsymbol{R}_i^n + \int_{t_n}^{t_n+h} \mathrm{ds} \boldsymbol{V}_i^n, \tag{C.7}$$

$$\boldsymbol{Q}_i^{n+1} = \boldsymbol{Q}_i^n + \int_{t_n}^{t_n+h} \mathrm{ds} \left[\mathrm{skew} \left(\Omega_i^n \right) \boldsymbol{Q}_i^n \right], \tag{C.8}$$

where the pressure term p^* in Eq. (C.6) is necessary to guarantee the incompressible condition $\boldsymbol{\nabla} \cdot \boldsymbol{u}^* = 0$.

C.1.2 The second step

At the second step, the active motion of particles is calculated. Here, we would like to impose the active flow profile $\boldsymbol{u}^{\mathrm{s}}$ (given by Eq. (1.2)) at the surface of each particle with respect to the particle velocity $\boldsymbol{V}'_i, \boldsymbol{\Omega}'_i$, using the updated positions and orientations$\boldsymbol{R}_i^{n+1}, \boldsymbol{Q}_i^{n+1}$ obtained at the first step. Because the particle motion is determined by the active flow field as the reaction to it, we do not know the final updated values of particle velocities $\boldsymbol{V}_i^{n+1}, \boldsymbol{\Omega}_i^{n+1}$, which we should use when we enforce the active flow profile ($\boldsymbol{V}'_i = \boldsymbol{V}_i^{n+1}, \boldsymbol{\Omega}'_i = \boldsymbol{\Omega}_i^{n+1}$). Therefore we calculate this part iteratively, with the particle velocities at the previous step as values for the initial trial. The

second temporal value $\boldsymbol{u}^{**}$ is now:

$$\boldsymbol{u}^{**} = \boldsymbol{u}^{*} + \left[\int_{t_n}^{t_n+h} \mathrm{d}s \boldsymbol{f}_{\mathrm{sq}}\right], \tag{C.9}$$

$$\left[\int_{t_n}^{t_n+h} \mathrm{d}s \boldsymbol{f}_{\mathrm{sq}}\right] = \sum_i \varphi_{\mathrm{p}i}\left(\boldsymbol{V}_i' + \boldsymbol{\Omega}_i' \times \boldsymbol{r}_i + \boldsymbol{u}_i^{\mathrm{s}} - \boldsymbol{u}^{*}\right), + \sum_i \phi_{\mathrm{p}i}\left(\delta\boldsymbol{V}_i + \delta\boldsymbol{\Omega}_i \times \boldsymbol{r}_i\right) - \frac{h}{\rho}\boldsymbol{\nabla} p_{\mathrm{sq}}, \tag{C.10}$$

where, φ_{p} is an order parameter which takes nonzero values only at the surface, $\delta\boldsymbol{V}_i, \delta\boldsymbol{\Omega}_i$ the counter flow inside particle i against the active flow field and p_{sq} the pressure due to the active squirming. The first term on the right hand side of Eq. (C.10) is imposing the active flow field $\boldsymbol{u}^{\mathrm{s}}$ onto the particle surface. Technically, within the SPM scheme, if $\varphi_{\mathrm{p}i} \propto (1-\phi_{\mathrm{p}i})\left|\boldsymbol{\nabla}\phi_{\mathrm{p}i}\right|$ is nonzero on a computational grid point, the point is considered to be the surface of a particle. $\varphi_{\mathrm{p}i}$ is normalized such that $\left|\boldsymbol{\nabla}\phi_{\mathrm{p}i}\right|$ has a maximum value of one. The second term ensures that the local momentum conservation is met, by giving a counter-flow inside the particle. Considering the particle rigidity, such a counter flow $\delta\boldsymbol{V}_i, \delta\boldsymbol{\Omega}_i$ can be obtained by:

$$\int \mathrm{d}\boldsymbol{x}\phi_{\mathrm{p}i}\left(\delta\boldsymbol{V}_i + \delta\boldsymbol{\Omega}_i \times \boldsymbol{r}_i\right) = -\int \mathrm{d}\boldsymbol{x}\varphi_{\mathrm{p}i}\left(\boldsymbol{V}_i' + \boldsymbol{\Omega}_i' \times \boldsymbol{r}_i + \boldsymbol{u}_i^{\mathrm{s}} - \boldsymbol{u}^{*}\right), \tag{C.11}$$

$$\int \mathrm{d}\boldsymbol{x}\boldsymbol{r}_i \times \phi_{\mathrm{p}i}\left(\delta\boldsymbol{V}_i + \delta\boldsymbol{\Omega}_i \times \boldsymbol{r}_i\right) = -\int \mathrm{d}\boldsymbol{x}\boldsymbol{r}_i \times \varphi_{\mathrm{p}i}\left(\boldsymbol{V}_i' + \boldsymbol{\Omega}_i' \times \boldsymbol{r}_i + \boldsymbol{u}_i^{\mathrm{s}} - \boldsymbol{u}^{*}\right). \tag{C.12}$$

The last term in Eq. (C.10) is necessary to guarantee the incompressible condition for this temporal velocity field $\boldsymbol{\nabla}\cdot\boldsymbol{u}^{**} = 0$.

The hydrodynamic force and torque exerted on particles due to the fluid motion can now be calculated by considering the local momentum conservation. Note that all the contributions from the active flow field is included in this force. The time integration of the hydrodynamic force (torque) over a period of h should be equal to the

momentum transfer over the whole particle domain:

$$\left[\int_{t_n}^{t_n+h} \mathrm{d}s \left(\boldsymbol{F}_i^{\mathrm{H}} + \boldsymbol{F}_i^{\mathrm{sq}}\right)\right] = \int \mathrm{d}\boldsymbol{x} \rho \phi_{\mathrm{p}i}^{n+1} \left(\boldsymbol{u}^{**} - \boldsymbol{u}_{\mathrm{p}}^{n}\right) \tag{C.13}$$

$$\left[\int_{t_n}^{t_n+h} \mathrm{d}s \left(\boldsymbol{N}_i^{\mathrm{H}} + \boldsymbol{N}_i^{\mathrm{sq}}\right)\right] = \int \mathrm{d}\boldsymbol{x} \left[\boldsymbol{r}_i^{n+1} \times \rho \phi_{\mathrm{p}i}^{n+1} \left(\boldsymbol{u}^{**} - \boldsymbol{u}_{\mathrm{p}}^{n}\right)\right] \tag{C.14}$$

Now that we have all the forces exerted on particles, we can update the particle velocities using all those values:

$$\boldsymbol{V}_i^{n+1} = \boldsymbol{V}_i^{n} + M_{\mathrm{p}}^{-1} \left[\int_{t_n}^{t_n+h} \mathrm{d}s \left(\boldsymbol{F}_i^{\mathrm{H}} + \boldsymbol{F}_i^{\mathrm{sq}}\right)\right] + M_{\mathrm{p}}^{-1} \left[\int_{t_n}^{t_n+h} \mathrm{d}s \boldsymbol{F}_i^{\mathrm{C}}\right], \tag{C.15}$$

$$\boldsymbol{\Omega}_i^{n+1} = \boldsymbol{\Omega}_i^{n} + \boldsymbol{I}_{\mathrm{p}}^{-1} \cdot \left[\int_{t_n}^{t_n+h} \mathrm{d}s \left(\boldsymbol{N}_i^{\mathrm{H}} + \boldsymbol{N}_i^{\mathrm{sq}}\right)\right], \tag{C.16}$$

where $\boldsymbol{F}_i^{\mathrm{c}}$ follows from Eq. (1.11). Note that all the calculations in the second step are based on a guess of the resultant velocity, $\boldsymbol{V}', \boldsymbol{\Omega}'$, which are not necessarily equal to the final values of $\boldsymbol{V}_i^{n+1}, \boldsymbol{\Omega}_i^{n+1}$. We iterate over Eqs. (C.9)-(C.16) until we see convergence in the velocities, $\boldsymbol{V}_i' = \boldsymbol{V}_i^{n+1}, \boldsymbol{\Omega}_i' = \boldsymbol{\Omega}_i^{n+1}$

C.1.3 The third step

Including the updated particle velocity field, the total velocity field is updated fully:

$$\boldsymbol{u}^{n+1} = \boldsymbol{u}^{**} + \left[\int_{t_n}^{t_n+h} \mathrm{d}s \phi_{\mathrm{p}} \boldsymbol{f}_p\right], \tag{C.17}$$

$$\left[\int_{t_n}^{t_n+h} \mathrm{d}s \phi_{\mathrm{p}} \boldsymbol{f}_p\right] = \phi_{\mathrm{p}}^{n+1} \left(\boldsymbol{u}_{\mathrm{p}}^{n+1} - \boldsymbol{u}^{**}\right) - \frac{h}{\rho} \boldsymbol{\nabla} p_{\mathrm{p}}, \tag{C.18}$$

where p_{p} is the pressure due to the rigidity of the particles which ensures the imcompressible condition$\boldsymbol{\nabla} \cdot \boldsymbol{u}^{n+1} = 0$. The total pressure field can be expressed as:

$$p = p^* + p_{\mathrm{p}} + p_{\mathrm{sq}}. \tag{C.19}$$

Bibliography

[1]M. C. Marchetti, J. F. Joanny, S Ramaswamy, T. B. Liverpool, J. Prost, M. Rao, and R. A. Simha, "Hydrodynamics of soft active matter", Reviews Of Modern Physics **85**, 1143–1189 (2013).

[2]T. Vicsek and A. Zafeiris, "Collective motion", Physics Reports **517**, 71–140 (2012).

[3]C. Bechinger, R. Di Leonardo, H. Löwen, C. Reichhardt, G. Volpe, and G. Volpe, "Active Particles in Complex and Crowded Environments", Reviews Of Modern Physics **88**, 045006 (2016).

[4]A. Cavagna and I. Giardina, "Bird Flocks as Condensed Matter", Annual Review of Condensed Matter Physics **5**, 183–207 (2014).

[5]J. S. Guasto, R. Rusconi, and R. Stocker, "Fluid mechanics of planktonic microorganisms", Annual Review of Fluid Mechanics **44**, 373–400 (2012).

[6]V. Prymidis, S. Paliwal, M. Dijkstra, and L. Filion, "Vapour-liquid coexistence of an active Lennard-Jones fluid", The Journal of Chemical Physics **145**, 124904 (2016).

[7]J. Blaschke, M. Maurer, K. Menon, A. Zöttl, and H. Stark, "Phase separation and coexistence of hydrodynamically interacting microswimmers", Soft Matter **12**, 9821–9831 (2016).

[8]X. Yang, M. L. Manning, and M. C. Marchetti, "Soft Matter", Soft Matter **10**, 6477–6484 (2014).

[9]W. Yan and J. F. Brady, "The swim force as a body force", Soft Matter **11**, 6235–6244 (2015).

[10]R. G. Winkler, A. Wysocki, and G. Gompper, "Virial pressure in systems of spherical active Brownian particles", Soft Matter **11**, 6680–6691 (2015).

[11]T. Speck, "Stochastic thermodynamics for active matter", EPL (Europhysics Letters) **114**, 30006 (2016).

[12]A. P. Solon, Y Fily, A Baskaran, M. E. Cates, Y Kafri, M Kardar, and J Tailleur, "Pressure is not a state function for generic active fluids", Nature Physics **11**, 673–678 (2015).

[13]A. Tiribocchi, J. Stenhammar, R. J. Allen, D. Marenduzzo, M. E. Cates, and R. Wittkowski, "field theory for active-particle phase separation", Nature Communications **5**, 1–9 (2014).

[14]É. Fodor, C. Nardini, M. E. Cates, J. Tailleur, P. Visco, and F. van Wijland, "How Far from Equilibrium Is Active Matter?", Physical Review Letters **117**, 038103 (2016).

[15]S. C. Takatori and J. F. Brady, "Towards a thermodynamics of active matter", Physical Review E **91**, 032117 (2015).

[16]S. C. Takatori, W Yan, and J. F. Brady, "Swim Pressure: Stress Generation in Active Matter", Physical Review Letters **113**, 028103 (2014).

[17]F. Smallenburg and H. Löwen, "Swim pressure on walls with curves and corners", Physical Review E **92**, 032304 (2015).

[18]F. Ginot, I. Theurkauff, D. Levis, C. Ybert, L. Bocquet, L. Berthier, and C. Cottin-Bizonne, "Nonequilibrium Equation of State in Suspensions of Active Colloids", Physical Review X **5**, 011004 (2015).

[19]A. P. Solon, J. Stenhammar, R. Wittkowski, M. Kardar, Y. Kafri, M. E. Cates, and J. Tailleur, "Pressure and Phase Equilibria in Interacting Active Brownian Spheres", Physical Review Letters **114**, 198301 (2015).

[20]K. Terayama, K. Hongo, H. Habe, and M.-a. Skagami, "Appearnce-based Multiple Fish Tracking for Collective Motion Analysis", 2015 3rd IAPR Asian Conference on Pattern Recognition (2016).

[21]A. Waters, F. Blanchette, and A. D. Kim, "Modeling Huddling Penguins", PLoS ONE **7**, e50277 (2012).

[22]K. Suzuki, K. Minami, and T. Inamuro, "Lift and thrust generation by a butterfly-like flapping wing–body model: immersed boundary–lattice Boltzmann simulations", Journal of Fluid Mechanics **767**, 659–695 (2015).

[23]A. Cavagna, A. Cimarelli, I. Giardina, G. Parisi, R. Santagati, F. Stefanini, and M. Viale, "Scale-free correlations in starling flocks", Proceedings of the National Academy of Sciences **107**, 11865–11870 (2010).

[24]S. Bazazi, J. Buhl, J. J. Hale, M. L. Anstey, G. A. Sword, S. J. Simpson, and I. D. Couzin, "Collective Motion and Cannibalism in Locust Migratory Bands", Current Biology **18**, 735–739 (2008).

[25]T. Toyota, N. Maru, M. M. Hanczyc, T. Ikegami, and T. Sugawara, "Self-Propelled Oil Droplets Consuming "Fuel" Surfactant", Journal of the American Chemical Society **131**, 5012–5013 (2009).

[26]T. Banno, A. Asami, N. Ueno, H. Kitahata, Y. Koyano, K. Asakura, and T. Toyota, "Deformable Self-Propelled Micro-Object Comprising Underwater Oil Droplets", **6**, 31292 EP –9 (2016).

[27]N. J. Suematsu, S. Nakata, A. Awazu, and H. Nishimori, "Collective behavior of inanimate boats", Physical Review E **81**, 056210 (2010).

[28]M. S. Davies Wykes, J. Palacci, T. Adachi, L. Ristroph, X. Zhong, M. D. Ward, J. Zhang, and M. J. Shelley, "Dynamic self-assembly of microscale rotors and swimmers", Soft Matter **12**, 4584–4589 (2016).

[29]I Theurkauff, C Cottin-Bizonne, J Palacci, C Ybert, and L Bocquet, "Dynamic Clustering in Active Colloidal Suspensions with Chemical Signaling", Physical Review Letters **108**, 268303 (2012).

[30]J. Palacci, S. Sacanna, A. Vatchinsky, P. M. Chaikin, and D. J. Pine, "Photoactivated Colloidal Dockers for Cargo Transportation", Journal of the American Chemical Society **135**, 15978–15981 (2013).

[31]H. Kitahata, N. Yoshinaga, K. H. Nagai, and Y. Sumino, "Spontaneous motion of a droplet coupled with a chemical wave", Physical Review E **84**, 015101 (2011).

[32]N. J. Suematsu, Y. Mori, T. Amemiya, and S. Nakata, "Oscillation of Speed of a Self-Propelled Belousov–Zhabotinsky Droplet", The Journal of Physical Chemistry Letters **7**, 3424–3428 (2016).

[33]R. Suzuki, C. A. Weber, E. Frey, and A. R. Bausch, "Polar pattern formation in driven filament systems requires non-binary particle collisions", Nature Physics **11**, 839–843 (2015).

[34]V. Schaller, C. Weber, C. Semmrich, E. Frey, and A. R. Bausch, "Polar patterns of driven filaments", Nature **467**, 73–77 (2010).

[35]K. Y. Wan and R. E. Goldstein, "Coordinated beating of algal flagella is mediated by basal coupling", Proceedings of the National Academy of Sciences **113**, E2784–E2793 (2016).

[36]P. Kanehl and T. Ishikawa, "Fluid mechanics of swimming bacteria with multiple flagella", Physical Review E **89**, 042704 (2014).

[37]K. Ishimoto, "Hydrodynamic evolution of sperm swimming: Optimal flagella by a genetic algorithm", Journal of Theoretical Biology **399 IS -**, 166–174 (2016).

[38]E Lushi, H Wioland, and R. E. Goldstein, "Fluid flows created by swimming bacteria drive self-organization in confined suspensions", Proceedings of the National Academy of Sciences **111**, 9733–9738 (2014).

[39]A. Kaiser, A. Peshkov, A. Sokolov, B. ten Hagen, H. Löwen, and I. S. Aranson, "Transport Powered by Bacterial Turbulence", Physical Review Letters **112**, 158101 (2014).

[40]A Kaiser, H. H. Wensink, and H Löwen, "How to Capture Active Particles", Physical Review Letters **108**, 268307 (2012).

[41]L. Angelani, R. Di Leonardo, and G. Ruocco, "Self-Starting Micromotors in a Bacterial Bath", Physical Review Letters **102**, 048104 (2009).

[42]R Di Leonardo, L Angelani, D Dell'Arciprete, G Ruocco, V Iebba, S Schippa, M. P. Conte, F Mecarini, F De Angelis, and E Di Fabrizio, "Bacterial ratchet motors", Proceedings of the National Academy of Sciences of the United States of America **107**, 9541–9545 (2010).

[43]T. Vicsek, A. Czirók, E. Ben-Jacob, I. Cohen, and O. Shochet, "Novel Type of Phase Transition in a System of Self-Driven Particles", Physical Review Letters **75**, 1226–1229 (1995).

[44]H. Chaté, F. Ginelli, and F. Raynaud, "Collective motion of self-propelled particles interacting without cohesion", Physical Review E **77** (2008).

[45]H. Chaté, F. Ginelli, and R. Montagne, "Simple Model for Active Nematics: Quasi-Long-Range Order and Giant Fluctuations", Physical Review Letters **96**, 180602 (2006).

[46]G. Grégoire and H. Chaté, "Onset of Collective and Cohesive Motion", Physical Review Letters **92**, 025702 (2004).

[47]J. Howse, R. Jones, A. Ryan, T. Gough, R. Vafabakhsh, and R. Golestanian, "Self-Motile Colloidal Particles: From Directed Propulsion to Random Walk", Physical Review Letters **99**, 048102 (2007).

[48]W. Yan and J. F. Brady, "The behavior of active diffusiophoretic suspensions: An accelerated Laplacian dynamics study", The Journal of Chemical Physics **145**, 134902 (2016).

[49]M. Rein and T. Speck, "Applicability of effective pair potentials for active Brownian particles", The European Physical Journal E **39**, 84 (2016).

[50]H. C. Berg and L. turner, " Movement of microorganisms in viscous environments", Nature **278**, 349–351 (1979).

[51]A. Costanzo, J. Elgeti, T. Auth, G. Gompper, and M. Ripoll, "Motility-sorting of self-propelled particles in microchannels", EPL (Europhysics Letters) **107**, 36003 (2014).

[52]R. Soto and R. Golestanian, "Run-and-tumble dynamics in a crowded environment: Persistent exclusion process for swimmers", Physical Review E **89**, 012706 (2014).

[53]M Paoluzzi, R Di Leonardo, and L Angelani, "Self-Sustained Density Oscillations of Swimming Bacteria Confined in Microchambers", Physical Review Letters **115**, 188303 (2015).

[54]S. C. Takatori and J. F. Brady, "Swim stress, motion, and deformation of active matter: effect of an external field", Soft Matter **10**, 9433–9445 (2014).

[55]N. Nikola, A. P. Solon, Y. Kafri, M. Kardar, J. Tailleur, and R. Voituriez, "Active Particles with Soft and Curved Walls: Equation of State, Ratchets, and Instabilities", Physical Review Letters **117**, 098001 (2016).

[56]J. Stenhammar, D. Marenduzzo, R. J. Allen, and M. E. Cates, "Phase behaviour of active Brownian particles: the role of dimensionality", Soft Matter (2014).

[57]T. Speck and R. L. Jack, "Ideal bulk pressure of active Brownian particles", Physical Review E **93**, 062605 (2016).

[58]J. Bialké, J. T. Siebert, H. Löwen, and T. Speck, "Negative Interfacial Tension in Phase-Separated Active Brownian Particles", Physical Review Letters **115**, 098301 (2015).

[59]R Aditi Simha and S. Ramaswamy, "Hydrodynamic Fluctuations and Instabilities in Ordered Suspensions of Self-Propelled Particles", Physical Review Letters **89**, 058101 (2002).

[60]B. Ezhilan, M. J. Shelley, and D. Saintillan, "Instabilities and nonlinear dynamics of concentrated active suspensions", Physics of Fluids **25**, 070607 (2013).

[61]D. Saintillan and M. Shelley, "Instabilities and Pattern Formation in Active Particle Suspensions: Kinetic Theory and Continuum Simulations", Physical Review Letters **100**, 178103 (2008).

[62]M. J. Lighthill, "On the Squirming Motion of Nearly Spherical Deformable Bodies Through Liquids at Very Small Reynolds Numbers", Communications on Pure and Applied Mathematics **5**, 109–118 (1952).

[63]J. R. Blake, "A spherical envelope approach to ciliary propulsion", Journal of Fluid Mechanics **46**, 199–208 (1971).

[64]I Llopis and I. Pagonabarraga, "Hydrodynamic interactions in squirmer motion: Swimming with a neighbour and close to a wall", Journal Of Non-Newtonian Fluid Mechanics **165**, 946–952 (2010).

[65]I. O. Götze and G. Gompper, "Mesoscale simulations of hydrodynamic squirmer interactions", Physical Review E **82**, 041921 (2010).

[66]G.-J. Li and A. M. Ardekani, "Hydrodynamic interaction of microswimmers near a wall", Physical Review E **90**, 013010 (2014).

[67]L Zhu, E Lauga, and L Brandt, "Low-Reynolds-number swimming in a capillary tube", Journal of Fluid Mechanics **726**, 285–311 (2013).

[68]J. J. Molina, Y. Nakayama, and R. Yamamoto, "Hydrodynamic interactions of self-propelled swimmers", Soft Matter **9**, 4923–4936 (2013).

[69]T Ishikawa and M Hota, "Interaction of two swimming Paramecia", Journal of Experimental Biology **209**, 4452–4463 (2006).

[70]T. Ishikawa and T. J. Pedley, "The rheology of a semi-dilute suspension of swimming model micro-organisms", Journal of Fluid Mechanics **588**, 399–435–435 (2007).

[71]T. Ishikawa and T. J. Pedley, "Coherent structures in monolayers of swimming particles", Physical Review Letters **100**, 088103 (2008).

[72]M. T. Downton and H. Stark, "Simulation of a model microswimmer", Journal of Physics: Condensed Matter **21**, 204101 (2009).

[73]D. Giacche and T. Ishikawa, "Hydrodynamic interaction of two unsteady model microorganisms", Journal of Theoretical Biology **267**, 252–263 (2010).

[74]Z. Lin, J.-L. Thiffeault, and S. Childress, "Stirring by squirmers", Journal of Fluid Mechanics **669**, 167–177 (2011).

[75]F Alarcon and I. Pagonabarraga, "Spontaneous aggregation and global polar ordering in squirmer suspensions", Journal of Molecular Liquids **185**, 56–61 (2013).

[76]K Kyoya, D Matsunaga, Y Imai, T Omori, and T Ishikawa, "Shape matters: Near-field fluid mechanics dominate the collective motions of ellipsoidal squirmers", Physical Review E **92**, 063027 (2015).

[77]J. S. Lintuvuori, A. T. Brown, K. Stratford, and D. Marenduzzo, "Hydrodynamic oscillations and variable swimming speed in squirmers close to repulsive walls", Soft Matter **12**, 7959–7968 (2016).

[78]A. S. Khair and N. G. Chisholm, "Expansions at small Reynolds numbers for the locomotion of a spherical squirmer", Physics of Fluids **26**, 011902 (2014).

[79]T. Ishikawa and T. J. Pedley, "Diffusion of swimming model micro-organisms in a semi-dilute suspension", Journal of Fluid Mechanics **588**, 437–462 (2007).

[80]Y. Nakayama and R. Yamamoto, "Simulation method to resolve hydrodynamic interactions in colloidal dispersions", Physical Review E **71**, 036707 (2005).

[81]K. Kim, Y. Nakayama, and R. Yamamoto, "Direct Numerical Simulations of Electrophoresis of Charged Colloids", Physical Review Letters **96**, 208302 (2006).

[82]Y. Nakayama, K Kim, and R. Yamamoto, "Simulating (electro) hydrodynamic effects in colloidal dispersions: Smoothed profile method", The European Physical Journal E **26**, 361–368 (2008).

[83]A. A. Evans, T. Ishikawa, T. Yamaguchi, and E. Lauga, "Orientational order in concentrated suspensions of spherical microswimmers", Physics of Fluids **23** (2011).

[84]N. Oyama, J. J. Molina, and R. Yamamoto, "Purely hydrodynamic origin for swarming of swimming particles", Physical Review E **93**, 043114 (2016).

[85]H Chaté, F Ginelli, G Grégoire, F. Peruani, and F Raynaud, "Modeling collective motion: variations on the Vicsek model", The European Physical Journal B **64**, 451–456 (2008).

[86]J Buhl, D. J. T. Sumpter, I. D. Couzin, J. J. Hale, E Despland, E. R. Miller, and S. J. Simpson, "From Disorder to Order in Marching Locusts", Science **312**, 1402–1406 (2006).

[87]M Ballerini, N Cabibbo, R Candelier, A Cavagna, E Cisbani, I Giardina, V Lecomte, A Orlandi, G Parisi, A Procaccini, M Viale, and V Zdravkovic, "Interaction ruling animal collective behavior depends on topological rather than metric distance: Evidence from a field study", in Proceedings of the national academy of sciences (2008), pp. 1232–1237.

[88]D. Volfson, S. Cookson, J. Hasty, and L. S. Tsimring, "Biomechanical ordering of dense cell populations", in Proceedings of the national academy of sciences (2008), pp. 15346–15351.

[89]R. Lukeman, Y.-X. Li, and L. Edelstein-Keshet, "Inferring individual rules from collective behavior", in Proceedings of the national academy of sciences (2010), pp. 12576–12580.

[90]S. Rafaï, L. Jibuti, and P. Peyla, "Effective Viscosity of Microswimmer Suspensions", Physical Review Letters **104**, 098102 (2010).

[91]A Zöttl and H. Stark, "Hydrodynamics Determines Collective Motion and Phase Behavior of Active Colloids in Quasi-Two-Dimensional Confinement", Physical Review Letters (2014).

[92]T. Ishikawa, M. P. Simmonds, and T. J. Pedley, "Hydrodynamic interaction of two swimming model micro-organisms", Journal of Fluid Mechanics **568**, 119–160–160 (2006).

[93]N. Oyama, J. J. Molina, and R. Yamamoto, "Hydrodynamic alignment of microswimmers in pipes", arXiv.org (2016).

[94]Y. Katz, K. Tunstrøm, C. C. Ioannou, C. Huepe, and I. D. Couzin, "Inferring the structure and dynamics of interactions in schooling fish", in Proceedings of the national academy of sciences (2011), pp. 18720–18725.

[95]T. Hanke, C. A. Weber, and E. Frey, "Understanding collective dynamics of soft active colloids by binary scattering", Physical Review E **88**, 052309 (2013).

[96]K.-D. N. T. Lam, M. Schindler, and O. Dauchot, "Self-propelled hard disks: implicit alignment and transition to collective motion", New Journal of Physics **17**, 1–10 (2015).

[97]A. Sokolov, I. Aranson, J. Kessler, and R. Goldstein, "Concentration Dependence of the Collective Dynamics of Swimming Bacteria", Physical Review Letters **98**, 158102 (2007).

[98]R. W. Nash, R Adhikari, J Tailleur, and M. E. Cates, "Run-and-Tumble Particles with Hydrodynamics: Sedimentation, Trapping, and Upstream Swimming", Physical Review Letters **104**, 258101 (2010).

[99]S. Mishra, "Giant number fluctuation in the collection of active apolar particles: from spheres to long rods", Journal Of Statistical Mechanics-Theory And Experiment **2014**, P07013 (2014).

[100]C. D. Nadell, J. B. Xavier, and K. R. Foster, "The sociobiology of biofilms", FEMS Microbiology Reviews **33**, 206–224 (2009).

[101]D Laage, "A Molecular Jump Mechanism of Water Reorientation", Science **311**, 832–835 (2006).

[102]F. G. Woodhouse and R. E. Goldstein, "Spontaneous Circulation of Confined Active Suspensions", Physical Review Letters **109**, 168105 (2012).

[103]T Ohta and S Yamanaka, "Soliton-like behavior of traveling bands in self-propelled soft particles", Progress of Theoretical and Experimental Physics **2014**, 11J01–0 (2014).

[104]J.-P. Hansen and I. R. McDonald, *Theory of Simple Liquids*, 3rd (Academic Press, New York, 2008).

[105]T. Ishikawa, J. T. Locsei, and T. J. Pedley, "Development of coherent structures in concentrated suspensions of swimming model micro-organisms", Journal of Fluid Mechanics **615**, 401–431 (2008).

[106]A. Lefauve and D. Saintillan, "Globally aligned states and hydrodynamic traffic jams in confined suspensions of active asymmetric particles", Physical Review E **89**, 021002 (2014).

[107]A. C. H. Tsang and E. Kanso, "Density Shock Waves in Confined Microswimmers", Physical Review Letters **116**, 048101 (2016).

[108]N. Desreumaux, J.-B. Caussin, R. Jeanneret, E. Lauga, and D. Bartolo, "Hydrodynamic Fluctuations in Confined Particle-Laden Fluids", Physical Review Letters **111**, 118301 (2013).

[109]W Hess and R Klein, "Generalized hydrodynamics of systems of Brownian particles", Advances in physics **32**, 173–283 (2006).

[110]A. Zöttl and H. Stark, "Emergent behavior in active colloids", Journal of Physics: Condensed Matter **28**, 253001 (2016).

[111]W. F. Paxton, K. C. Kistler, C. C. Olmeda, A. Sen, S. K. St Angelo, Y. Cao, T. E. Mallouk, P. E. Lammert, and V. H. Crespi, "Catalytic Nanomotors: Autonomous

Movement of Striped Nanorods", Journal of the American Chemical Society **126**, 13424–13431 (2004).

[112]W. F. Paxton, S. Sundararajan, T. E. Mallouk, and A. Sen, "Chemical Locomotion", Angewandte Chemie International Edition **45**, 5420–5429 (2006).

[113]S. Das, A. Garg, A. I. Campbell, J. Howse, A. Sen, D. Velegol, R. Golestanian, and S. J. Ebbens, "Boundaries can steer active Janus spheres", Nature Communications **6**, 8999 (2015).

[114]J. de Graaf, A. J. T. M. Mathijssen, M. Fabritius, H. Menke, C. Holm, and T. N. Shendruk, "Understanding the onset of oscillatory swimming in microchannels", Soft Matter **12**, 4704–4708 (2016).

[115]M. N. Popescu, M. N. Popescu, S Dietrich, S Dietrich, G Oshanin, and G Oshanin, "Confinement effects on diffusiophoretic self-propellers", The Journal of Chemical Physics **130**, 194702 (2009).

[116]N. Oyama, J. J. Molina, and R. Yamamoto, "A binary collision route for purely hydrodynamic orientational ordering of microswimmers", arXiv.org (2016).

[117]J. Elgeti and G. Gompper, "Wall accumulation of self-propelled spheres", Europhysics Letters (EPL) **101**, 48003 (2013).

[118]W. B. Russel, D. A. Saville, and W. R. Schowalter, *Colloidal Dispersions*, 1st ed. (Cambridge University Press, Cambridge, 1992).

[119]O. S. Pak and E. Lauga, "Generalized squirming motion of a sphere", Journal of Engineering Mathematics **88**, 1–28 (2014).

[120]S. H. Lamb, *Hydrodynamics* (Courier Corporation, 1945).